

EFFECTS OF CLIMATE CHANGE AND PERTURBATION IN BIOGEOCHEMICAL
CYCLES ON OXYGEN DISTRIBUTION AND OCEAN ACIDIFICATION

by

TERESA MARIE BEATY-SYKES

Presented to the Faculty of the Graduate School of
The University of Texas at Arlington in Partial Fulfillment
of the Requirements
for the Degree of

DOCTOR OF PHILOSOPHY

THE UNIVERSITY OF TEXAS AT ARLINGTON

DECEMBER 2014

Copyright © by Teresa Marie Beaty-Sykes 2014

All Rights Reserved

Dedication

I dedicate my dissertation work to the memory of my father, Gerald W Beaty, for all the guidance and support throughout my life. It was his unconditional love, support, and encouragement that empowered me to pursue my love of science. I grew up watching him work miracles in the back yard using science and engineering. He built planes, model aircraft, and cars; sometimes building the needed parts from scratch. He had many talents and many hobbies. One of my fondest childhood memories was building the 16-inch telescope, which I still have to this day. He was my real-life MacGyver and an inspiration. My father was an amazing man who could fix anything, build anything, and fly anything. I only hope that I can become half the person he was and everything he hoped I could be.

Acknowledgements

I would like to acknowledge all those who have worked on and with the HAMOCC model; the late Dr. Ernst Maier-Reimer, Dr. Christoph Heinze, and Dr. Virginia Palastanga. I would also like to thank Dr. Heinze for the use of his plotting program. This dissertation would not have been possible without the guidance and patience of my Ph.D advisor Dr. Arne Winguth who introduced me to high-performance computing and set me on my way in a world that was totally alien to me at the beginning of this adventure. I would also like to thank all of my committee members Dr. Hu, Dr. Sattler, Dr. Griffith, and Dr. Mydlarz for their time and guidance on this project. Finally, I would like to thank my family, my daughter Genesis, and everyone who stood beside me, pushed me, and put up with me while I worked toward this degree. Plotting was accomplished on NCAR computers, which are supported by the National Science Foundation. This research is supported by NSF grants EAR-0628336 and EAR 0745817 as well as NSF STEM support and UTA graduate dissertation fellowship.

November 21, 2014

Abstract

EFFECTS OF CLIMATE CHANGE AND PERTUBATION IN BIOGEOCHEMICAL CYCLES ON OXYGEN DISTRIBUTION AND OCEAN ACIDIFICATION

Teresa Marie Beaty-Sykes, PhD

The University of Texas at Arlington, 2014

Supervising Professor: Arne Winguth

Dissolved oxygen (DO) concentration in the ocean is an important component of the marine biogeochemical cycles. In this study a global oceanic carbon cycle model (HAMOCC 2.0) was used to address how oxygen minimum zones (OMZ) respond to changes due to CO₂ radiative forcing. Atmospheric pCO₂ was increased at a rate of 1% annually and the model is stabilized at 2 X, 4 X, 6 X, and 8 X preindustrial pCO₂ levels. With an increase in CO₂ radiative forcing, the OMZ in the Pacific Ocean was controlled largely by changes in particulate organic carbon (POC) export. In contrast, the vertical expansion of the OMZs within the Atlantic and Indian Oceans were the result of changes to oxygen solubility. Changes in oxygen solubility also lead to the formation of a new OMZ in the western sub-tropical Pacific Ocean. The response of the pH value to a total carbon emission of 4480 PgC or 8 times preindustrial pCO₂ was found to be comparable to the ocean acidification at the PETM (56 Ma). The HAMOCC 2.0 simulations indicate a significant relationship between the pH value and the DO concentration at intermediate depth. This can lead to stress for the marine ecosystem by further decreasing pH due to respiratory processes. Improved parameterization may enhance the predictability of regions with low DO concentrations and pH value. A 50% increase in atmospheric dust deposition did not significantly alter the regions of Fe limitation of export production and

hence did not result in significant changes in DO in the twilight zone and at intermediate depth. However, a 50% reduction in dust deposition significantly expanded the regions of Fe-limited export production thereby reducing the vertical particle flux of POC and the extent of the OMZs. This counteracted the OMZ expansion due to the increased CO₂ radiative forcing.

Table of Contents

Acknowledgements	iv
Abstract	v
List of Illustrations	x
List of Tables	xvii
Chapter 1 Introduction	1
1.1 Climate change	1
1.2 Biogeochemical cycles and dissolved oxygen distribution in the ocean	5
1.2.1 Marine carbon cycle	5
1.2.2 Marine phosphorus cycle	9
1.2.3 Dissolved ocean oxygen distribution	11
Chapter 2 Objectives	13
2.1 Introduction	13
2.2 Response of the oxygen minimum zone and pH value to CO ₂ radiative forcing ...	13
2.3 Reduced biology and atmospheric oxygen concentration experiments	16
2.4 Fe fertilization experiments	17
Chapter 3 HAMOCC 2.0 Model Description and Reference Simulation	21
3.1 Model description	21
3.2 The reference experiment	30
3.2.1 Initial and boundary conditions used	30
3.2.2 Reference run results and discussion	32
Chapter 4 Response of Export Production and Dissolved Oxygen Concentrations to pCO ₂ and Temperature Stabilization Scenarios	42
4.1 Introduction	42
4.2 Experimental design	43

4.3 Results.....	45
4.3.1 Sensitivity of the dissolved oxygen distribution to reduced biological pump and atmospheric pO ₂	45
4.3.1.2 Sensitivity of dissolved oxygen to reduced atmospheric pO ₂	46
4.3.2 Sensitivity of the oxygen minimum zone to CO ₂ radiative forcing	47
4.3.2.4 Simulated OMZ formation in the western tropical Pacific Ocean in response to CO ₂ radiative forcing.	54
4.4 Discussion	59
4.5 Conclusion and future research.....	64
Chapter 5 Response of Ocean Acidification to Anthropogenic-Induced Carbon Emission.....	
Emission.....	69
5.1 Introduction	69
5.2 Experimental design	71
5.3 Results.....	71
5.3.1 Sensitivity of ocean acidification to atmospheric carbon input.	71
5.3.2 Regression analyses of O ₂ , total DIC, and pH.	75
5.4 Discussion	79
5.5 Conclusion and future research.....	83
Chapter 6 Affects of Changes in Atmospheric Dust Deposition on Iron Fertilization and Dissolved Oxygen Concentration in the Ocean	
Dissolved Oxygen Concentration in the Ocean	86
6.1 Introduction	86
6.2 Experimental design	87
6.3 Results.....	88
6.3.1 Particulate organic carbon export response to changes in atmospheric dust deposition.	88

6.3.2 Particulate organic carbon export response to an increase of atmospheric dust.....	89
6.3.4 Global dissolved oxygen concentration response to changes in dust deposition.....	95
6.3.5 Oxygen minimum zone response to changes in dust deposition.....	97
6.4 Discussion	102
6.5 Conclusion and future perspectives.....	109
References	111
Biographical Information	138

List of Illustrations

Figure 2-1 Flow diagram of the impacts of atmospheric CO ₂ on OMZs.....	19
Figure 3-1 Schematic model concept diagram including the sediment biogeochemical cycling of sedimentary phosphorus (Heinze et al., 1991; Palastanga et al., 2011).	21
Figure 3-2 Surface DIC in $\mu\text{mol L}^{-1}$ simulated by HAMOCC3 from Maier-Reimer (1993).....	34
Figure 3-3 Surface DIC in $\mu\text{mol L}^{-1}$ simulated by preindustrial reference experiment of this study.....	35
Figure 3-4 Dissolved oxygen concentration in ml L^{-1} at 3000 m depth from the World Ocean Atlas 2013. Note that $1 \text{ ml L}^{-1} \text{ O}_2$ is equal to $44.6 \mu\text{mol L}^{-1} \text{ O}_2$	35
Figure 3-5 Dissolved oxygen concentration in $\mu\text{mol L}^{-1}$ at 3000 m depth from the preindustrial experiment of this study. Note that $1 \text{ ml L}^{-1} \text{ O}_2$ is equal to $44.6 \mu\text{mol L}^{-1} \text{ O}_2$	36
Figure 3-6 Export production of POC (a), CaCO ₃ (b) and opal (c) from the euphotic zone (100m) Sarmiento and Gruber (2006) compared to the preindustrial reference experiment of HAMOCC 2.0 (d-f) at 25 m depth.	37
Figure 3-7 Sediment composition of POC (a), CaCO ₃ (b) and opal (c) from Sarmiento and Gruber (2006) compared to the preindustrial reference experiment of HAMOCC 2.0 (d-f).....	38
Figure 3-8 Locations of the OMZ at 450 meters depth simulated by HAMOCC 2.0 (reference experiment) [1] Eastern North Pacific OMZ [2] Eastern South Pacific OMZ [3] Eastern South Atlantic OMZ [4] Indian Ocean.	39
Figure 3-9 Simulated core locations of present day permanent non-seasonal OMZ. [1] Eastern tropical North Pacific; 110°W, 10°N. [2] eastern tropical South Pacific; 85°W,	

10°S. [3] eastern tropical South Atlantic; 5°W, 10°S. [4] Indian Ocean (Gulf of Bengal); 85°E, 7°N.	40
Figure 3-10 Simulated vertical dissolved O ₂ concentrations through the OMZ cores for a) eastern North Pacific OMZ [10°N, 110°W], b) eastern South Pacific OMZ [10°S, 85°W], c) eastern South Atlantic [10°S, 5°W], and d) Indian Ocean OMZ [7°N, 85°E]. Observed data are the annual statistical mean for dissolved oxygen from the World Ocean Atlas 2013 (Garcia et al., 2014). Standard error of the mean; upper ocean: 0.54-2.86 μmol L ⁻¹ , twilight zone: 0.42-2.32 μmol L ⁻¹ , deep ocean: 0.36-1.98 μmol L ⁻¹	41
Figure 4-1 pCO ₂ and SST increase from the reference run (a) 2 X CO ₂ (b) 4 X CO ₂ (c) 6 X CO ₂ (d) 8 X CO ₂ for the first 500 years of a 30k year simulation. The red dashed line indicates the preindustrial pCO ₂ level.....	45
Figure 4-2 (a) Change in alkalinity from the reference run and (b) change in pH from the reference run for the extinction simulation.	46
Figure 4-3 (a) Dissolved oxygen concentration for the extinction simulations and (b) reference simulation oxygen concentration.	47
Figure 4-4 Change in dissolved oxygen concentration between the extinction simulation and the extinction simulation with a 50% reduction of atmospheric O ₂	47
Figure 4-5 Dissolved O ₂ concentration simulated by (a) the 4 X CO ₂ experiment without CO ₂ radiative forcing minus the reference experiment (b) the 4 X CO ₂ with CO ₂ radiative forcing simulation minus reference experiment.	48
Figure 4-6 Meridional cross-section of dissolved oxygen [μmol L ⁻¹] in the Pacific OMZ for the (a) reference experiment and (b) 8 X CO ₂ experiment, the Atlantic OMZ for the (c) reference experiment and (d) 8 X CO ₂ experiment, and the Indian Ocean for the (e) reference experiment and (f) 8 X CO ₂ experiment.....	52

Figure 4-7 Simulated vertical distribution of dissolved O₂ through the OMZ cores for a) Eastern North Pacific OMZ, b) Eastern South Pacific OMZ, c) Eastern South Atlantic OMZ, and d) Indian Ocean OMZ for the 1 X, 4 X and 8 X CO₂ simulations (top). The bottom row are finer scale dissolved oxygen profiles for the OMZ cores e) Eastern North Pacific OMZ, f) Eastern South Pacific OMZ, g) Eastern South Atlantic OMZ, and h) Indian Ocean OMZ for the 1 X, 4 X and 8 X CO₂ simulations. Observed data are the annual statistical mean for dissolved oxygen from the World Ocean Atlas, 2013 (Garcia et al., 2014). Standard error of the mean; upper ocean: 0.54-2.86 μmol L⁻¹, twilight zone: 0.42-2.32 μmol L⁻¹, deep ocean: 0.36-1.98 μmol L⁻¹. 53

Figure 4-8 Zonal cross-section at 1.25° N of the formation of the western tropical Pacific OMZ for the (a) 2 X, (b) 4 X and (c) 8 X CO₂ simulations. The OMZ core is located between 130°E and 150°E. 54

Figure 4-9 Simulated vertical dissolved oxygen concentration through the western tropical Pacific OMZ for the a) 1 X CO₂, b) 3 X CO₂, c) 4 X CO₂, and d) 8 X CO₂ simulations (Top). The bottom row are finer scale dissolved oxygen profiles for the OMZ cores e) 3 X CO₂, f) 4 X CO₂, and g) 8 X CO₂ simulations. The black dashed lines indicate the 20 μmol O₂ L⁻¹ threshold for OMZ core. Observed data are the annual statistical mean for dissolved oxygen from the World Ocean Atlas, 2013 (Garcia et al., 2014). Standard error of the mean; upper ocean: 0.54-2.86 μmol L⁻¹, twilight zone: 0.42-2.32 μmol L⁻¹, deep ocean: 0.36-1.98 μmol L⁻¹. 55

Figure 4-10 (a) Oxygen lost due to remineralization of particulate organic carbon for the reference run [μmol m⁻²yr⁻¹]. Difference between the loss of oxygen due to remineralization between (b) 2 X CO₂ and reference run, (c) 4 X CO₂ and reference run (d) 8 X CO₂ and reference run. 65

Figure 4-11 (a) Difference in export production of POC between the 2 X CO₂ experiment and reference experiment, (b) dissolved oxygen at 450 m depth for the 2 X CO₂ experiment, (c) difference in air-sea gas exchange between the 2 X CO₂ experiment and the reference experiment, and (d) sea-water temperature at 450 m depth. The numbers indicate the OMZ locations; [1] Eastern tropical North Pacific; 110°W, 10°N. [2] eastern tropical South Pacific; 85°W, 10°S. [3] eastern tropical South Atlantic; 5°W, 10°S. [4] Indian Ocean (Gulf of Bengal); 85°E, 7°N..... 66

Figure 4-12 (a) Difference in export production of POC between the 4 X CO₂ experiment and reference experiment, (b) dissolved oxygen at 450 m depth for the 4 X CO₂ experiment, (c) difference in air-sea gas exchange between the 4 X CO₂ experiment and the reference experiment, and (d) sea-water temperature at 450 m depth. The numbers indicate the OMZ locations; [1] Eastern tropical North Pacific; 110°W, 10°N. [2] eastern tropical South Pacific; 85°W, 10°S. [3] eastern tropical South Atlantic; 5°W, 10°S. [4] Indian Ocean (Gulf of Bengal); 85°E, 7°N..... 67

Figure 4-13 (a) Difference in export production of POC between the 8 X CO₂ experiment and reference experiment, (b) dissolved oxygen at 450 m depth for the 8 X CO₂ experiment, (c) difference in air-sea gas exchange between the 8 X CO₂ experiment and the reference experiment, and (d) sea-water temperature at 450 m depth. The numbers indicate the OMZ locations; [1] Eastern tropical North Pacific; 110°W, 10°N. [2] eastern tropical South Pacific; 85°W, 10°S. [3] eastern tropical South Atlantic; 5°W, 10°S. [4] Indian Ocean (Gulf of Bengal); 85°E, 7°N..... 68

Figure 5-1 (a) pH value of the 1 X CO₂ (reference) experiment and the difference in pH value between (b) 4 X CO₂ experiment and reference experiment, (c) 6 X CO₂ experiment and the reference experiment, and (d) 8 X CO₂ experiment and the reference experiment simulated by HAMOCC 2.0. 73

Figure 5-2 Zonal section of carbonate ion concentration at 2°N ($\mu\text{mol kg}^{-1}$) for (a) reference simulation, (b) 4 X CO_2 , and (c) 8 X CO_2 simulations. The solid and dashed black line indicates the calcite and aragonite saturation horizons. The contour interval for the pH value is 0.05 units. 74

Figure 5-3 CaCO_3 accumulations in ocean sediments in percent weight for the (a) reference experiment, (b) 2 X CO_2 , (c) 4 X CO_2 , and (d) 8 X CO_2 simulations. Ocean depth contours are displayed in Figure 3-9. 76

Figure 5-4 Regression analyses of the reference experiment for six simulated water columns between pH and dissolved O_2 (top) and between DIC and dissolved O_2 (bottom). Core numbers are located in brackets in the top left hand corner. Note that the dots reflect the water masses at various depths for each location. The location of each water column is displayed in Figure 5-5. 77

Figure 5-5 Location of water columns used for the regression analyses and the percent efficiency of the biological pump for the preindustrial simulations. 78

Figure 5-6 Regression analysis of a water column in the (Southern Ocean) simulated by the 8 X CO_2 experiment. 78

Figure 5-7 Simulated globally averaged CCD as a function of atmospheric pCO_2 levels from this study and the estimated CCD for the Pacific Ocean for the present (+), Younger Dryas (°) (Pälike et al., 2012), last glacial maximum (*) (Thunell et al., 1992; Pälike et al., 2012), Eocene/Oligocene (•) (Coxall et al., 2005; Liu et al., 2009; Pälike et al., 2012), and the CCD estimated derived from the Atlantic Ocean for the PETM (♦) (Zachos et al., 2005; Zachos et al., 2008). 80

Figure 5-8 Regression analysis of pH value and dissolved O_2 concentration in a water column in the North Pacific (location [1] ~10N, 110W) for the reference experiment (left) and the reduced biology simulation (right). 82

Figure 5-9 Regression analysis of DIC and dissolved O ₂ concentration in a water column in the North Pacific (location ~10N, 110W) for the reference experiment (left) and the extinction simulation (right).	83
Figure 6-1 Simulated atmospheric dust deposition for the (a) 1 X CO ₂ DUST-50%, (b) 1 XCO ₂ , and (c) 1 X CO ₂ DUST+50% simulations and sea surface dissolved iron concentrations for the (d) 1 X CO ₂ DUST-50%, (e) 1 XCO ₂ , and (f) 1 X CO ₂ DUST+50% simulations.	92
Figure 6-2 Export production of POC (P _{POC}) for the (a) 1 X CO ₂ DUST-50%, (b) 1 X CO ₂ , (c) 1 X CO ₂ DUST+50%, (d) 4 X CO ₂ DUST-50%, (e) 4 X CO ₂ , and (f) 4 X CO ₂ DUST+50% experiments.	93
Figure 6-3 POC flux for the 1 X CO ₂ (solid), 1 X CO ₂ DUST+50% (dashed), and 1 X CO ₂ DUST-50% (dashed-dot-dot) for the (a) Arabian Sea [10°S,70°E], (b) subtropical North Atlantic Ocean [30°N, 30°W], (c) equatorial Pacific Ocean [0°, 140°W], and (d) Southern Ocean [65°S, 110°W]. The circles are observed POC flux concentrations (Honjo et al., 1980; Honjo et al., 1995; Hammond et al., 1996; Rabouille et al., 1998).	94
Figure 6-4 Increase in export production of particulate organic carbon (P _{POC}) due to temperature-dependent productivity (difference between the 4 X CO ₂ and 1 X CO ₂ experiment.	94
Figure 6-5 Dissolved oxygen concentration [μmol L ⁻¹] at a depth of 400 m for the a) 1 X CO ₂ DUST-50%, b) 1 X CO ₂ , c) 1 X CO ₂ DUST+50%, d) 4 X CO ₂ DUST-50%, e) 4 X CO ₂ , and f) 4 X CO ₂ DUST+50% simulations.	99
Figure 6-6 Difference between the simulations with a 50% reduction in atmospheric dust deposition for the a) 1 X CO ₂ and b) 4 X CO ₂ simulations. Dissolved oxygen concentration [μmol L ⁻¹] for c) 1 X CO ₂ and d) 4 X CO ₂ simulations without a dust	

perturbation. Difference between the simulations with a 50% increase in atmospheric dust deposition for the e) 1 X CO ₂ and f) 4 X CO ₂ simulations.	100
Figure 6-7 Dissolved oxygen concentrations [$\mu\text{mol L}^{-1}$] for the OMZ cores for (a) 4 X CO ₂ DUST-50% and (b) 4 X CO ₂ DUST+50% simulations.	101
Figure 6-8 Difference in dissolved oxygen concentration [$\mu\text{mol L}^{-1}$] between the 4 X CO ₂ DUST-50% and the 1 X CO ₂ reference simulation.	101
Figure 6-9 Vertical dissolved oxygen concentration profiles [$\mu\text{mol L}^{-1}$] at ~10N, 140 W for the a) 1 X CO ₂ and b) 4 X CO ₂ simulations. The observations are taken from the World Ocean Atlas, 2013 (Garcia et al., 2014). Standard error of the mean; upper ocean: 0.54-2.86 $\mu\text{mol L}^{-1}$, twilight zone: 0.42-2.32 $\mu\text{mol L}^{-1}$, deep ocean: 0.36-1.98 $\mu\text{mol L}^{-1}$	102
Figure 6-10 Biological pump efficiency for the a) 1 X CO ₂ DUST-50%, b) 1 X CO ₂ , and c) 1 X CO ₂ DUST+50% simulations.	108
Figure 6-11 Change in total productivity through the dust perturbation and recovery simulations. The red line at indicates the time in which simulation starts to recover and the gray dotted line is the preindustrial total export production.....	109

List of Tables

Table 2-1 Summary of Experiment	20
Table 3-1 List of model tracers	22
Table 3-2 Initial conditions for the reference experiment	31
Table 3-3 Parameter value list for the reference experiment (after Palastanga et.al, (2011)).....	32
Table 4-1 Global total particulate organic carbon production and export production of particulate organic carbon (P_{POC}) at 30k years.	56
Table 4-2 Total ocean area and total ocean volume at which dissolved O_2 concentrations are $\leq 50 \mu\text{mol L}^{-1}$, $\leq 20 \mu\text{mol L}^{-1}$, and $\leq 12 \mu\text{mol L}^{-1}$ respectively for the 2 X, 4 X, 6 X and 8 X CO_2 simulations. Total ocean area value is from Volumes of the World's Oceans from ETOPO1 (Eakins and Sharman, 2010).....	58
Table 5-1 Global sum of P_{CaCO_3} and global average DIC, pH, and carbonate ion concentrations for the 2 X, 4 X, 6 X and 8 X CO_2 simulations.	72
Table 5-2 Lysocline depth and CCD for the 2 X, 4 X, 6 X and 8 X CO_2 simulations.....	72
Table 6-1 Description of the dust deposition experiments.	89
Table 6-2 Global means and percent change from the reference simulation for soluble iron, dissolved O_2 , total productivity and export production of POC for the dust perturbation experiments after 15kyr integration.	91
Table 6-3 Total ocean area (~volume) with a dissolved O_2 concentrations of $\leq 50 \mu\text{mol L}^{-1}$, $\leq 20 \mu\text{mol L}^{-1}$, for the experiments listed in Table 6-1 after 15k yrs of integration. Total ocean area is estimated from ETOPO1 (Eakins and Sharman, 2010).	96

Chapter 1

Introduction

1.1 Climate change

The investigation of paleoclimate during Earth's history is of interest to improve the understanding of future climate change. One of the most prominent changes in climate in Earth's history occurred at the end of the Permian (252 Ma; Erwin, 1994; Kidder and Worsley, 2004), which was potentially triggered by a variety of causes including an extraterrestrial impact and volcanism leading to global warming with tropical temperatures increasing by 12°C to over 40°C (Sun et al., 2012). The climatic shift in the Permian resulted in large shifts in stable carbon isotopes (Baud et al., 1989; Payne et al., 2004) and associated ocean stratification (Grotzinger and Knoll, 1995; Knoll et al., 1996) forest fires (Algeo et al., 2013), acid rain (Black et al., 2012), increased weathering, ocean anoxia (Wignall and Hallam, 1993; Isozaki, 1997; Benton and Twitchett, 2003), and ocean acidification (Honisch et al., 2012). These environmental changes lead to nich-loss, the lillyput effect, and massive terrestrial and oceanic extinction (Benton and Twitchett, 2003; Payne et al., 2004). The initial decline and the final extinction during the Permian-Triassic boundary coincides with the onset of ocean stratification and widespread anoxia (Knoll et al., 1996; Isozaki, 1997) which are supported by modeling studies; particularly if global nutrient concentration are elevated by the decline of the terrestrial ecosystem occurred that could have led to an increase in surface productivity and increase in the vertical organic carbon flux and anoxia in the deep sea (Meyer et al, 2008; Winguth and Winguth, 2012).

During the mid-Cretaceous (130-87 Ma) the atmospheric pCO₂ concentration was 2-10 times higher than present and the globally averaged surface temperatures were greater than the present by more than 14 °C and the sea level was 100-200 m higher

than today (Misumi and Yamanaka, 2008). This climate shift has been linked to higher volcanism associated with a faster spreading rate (Berner, 1997; Hay et al., 1996; Otto-Bliesner et al., 2003). Paleoclimate records from the Cretaceous indicate several Oceanic Anoxic Events (OAEs) as well as altered biogeochemical cycles associated with oxygen depletion in warm ocean waters (Leckie et al., 2002; Handoh and Lenton, 2003). The significance of these Cretaceous OAEs is the widespread deposition of black shale rich in organic matter, which indicated a shift in the carbon cycle and a direct effect on climate. One of the OAEs, OAE2, resulted in a reduction of atmospheric CO₂ due to a burial of 1.6 X 10¹⁸ moles of organic carbon over 0.5 my (Arthur et al., 1988; Kuypers et al., 1999). The increase in carbon burial may have led to the cooling that occurred in the late Cretaceous due to a decline in greenhouse gas concentration in the atmosphere (Berner, 2003). The cause of the deposition of organic rich black shale during OAE2 is controversial (e.g. Weissert, 1981; Erba et al., 2004); however, two mechanisms have been suggested as a cause: (1) oxygen supply decreased to the deep sea due to an increase in ocean stratification and (2) an increase in surface productivity which increases the vertical organic carbon flux and oxygen consumption in the deep sea (Sarmiento and Gruber, 2006). Another mechanism suggested by Misumi and Yamanaka (2008) for the OAEs of the Cretaceous is the increase in the nutrient concentration due to an increase in riverine input and sediment output, particularly during the OAE2 event. Misumi and Yamanaka (2008) suggested that under stagnant thermohaline circulation and present day dissolved nutrient concentration the anoxic bottom water covers 29% of the global ocean. By assuming that global nutrient concentration doubled the anoxic bottom water expanded to cover 100% of the global ocean.

A more recent global warming is the Paleocene-Eocene Thermal Maximum (PETM) at the Paleocene-Eocene boundary (~56 Ma), that has been treated as an

analog to the possible anthropogenic climate change of the future (Zachos et al., 2008). The PETM occurred approximately 55 Ma and is marked by an abrupt global warming (Kennett and Stott, 1991) inferred from a negative carbon isotope excursion (CIE) potentially due to increased emissions of isotopically light carbon possibly from methane hydrates and volcanism (Eldholm and Thomas, 1993; Dickens et al., 1995; McInerney and Wing, 2011). The carbon pulse at the PETM, inferred from the CIE of approximately -3.0 per mil (‰) in sediment cores (Thomas and Shackleton, 1996), likely caused a shoaling of the lysocline and calcite compensation depth (CCD) (Zachos et al., 2005). The PETM also coincides with the formation of the North Atlantic Igneous Province approximately 60.5 - 54.4 Ma (mid-Paleocene to early Eocene), which could have resulted in a large release of mantle-derived and volcanic CO₂ (Dickens et al., 1995; Svensen et al., 2004; Sluijs et al., 2007; Storey et al., 2007). Dickens et al. (1995) considered biogenic methane, methane clathrate, mantle-derived CO₂, and volcanic CO₂ as sources that may have contributed to this hyperthermal event. A model study (Panchuk et al., 2008) revealed that for larger CO₂ pulses the seafloor dissolution of CaCO₃ increased and that a pulse of at least 6800 Pg C would be required to result in the CaCO₃ dissolution at the seafloor during the PETM.

Abrupt climate shifts have occurred frequently over the last 100,000 years (Dansgaard et al., 1993) and it is possible for greenhouse gases to cause a rapid change in climate on decadal to centennial time scales (Broecker, 1997; Stocker and Schmittner, 1997). Since the 18th Century, the concentrations of greenhouse gases (CO₂, CH₄, and N₂O) in the atmosphere have significantly increased and are predicted to continue to rise from the pre-industrial level of 280 ppmv up to ~800 ppmv in the year 2100 (IPCC, 2013) or 2000 ppmv by year 2400 under the assumption that all fossil fuel reservoirs are emitted into the atmosphere (Caldeira and Wickett, 2003; Zachos et al., 2008). The

anthropogenic CO₂ will be partially sequestered by the ocean and by the biosphere on time scales in the order of 10⁴ years. An increase global temperature tends to keep CO₂ in the atmosphere due to the decreased solubility of CO₂ in the surface of warmer oceans making the oceans critical in the variability of Earth's climate. A rise in deep-water temperature on a 10,000 year timescale could decrease the effectiveness of the CaCO₃ cycle and sediment deposition (Archer et al., 2009).

Comprehensive Earth system model simulations (IPCC, 2013) are limited computationally (integrated <10,000 years) and thus are not suitable to investigate long-term feedbacks with the sediments. Studies have shown a strong feedback between the climate and the carbon cycle (Dufresne et al., 2002; Friedlingstein et al., 2003; Winguth et al., 2005; Mikolajewicz et al., 2007). Anthropogenic CO₂ emitted by fossil fuel combustion and land use changes remain in the atmosphere at least several centuries (Archer et al., 2009; IPCC, 2013). A release of greater than 5000 PgC nearly depletes CaCO₃ in the deep waters, thus leading to long residence times for anthropogenic CO₂ in the atmosphere with an exponential decline over centuries. However, ~20-35% will remain in the atmosphere after equilibrium (Archer, 2005) and dissolved inorganic carbon concentration in the ocean will remain high millennia (Zachos et al., 2008).

Changes in climate will also effect the oxygen distribution in the ocean. Dissolved oxygen in the ocean is affected by the solubility and biological pump in which the later is controlled by export production, vertical carbon flux and decay of particulate organic carbon, and by the transport of the tracers by the ocean circulation. Variations in seasonal and long-term oxygen concentration have been observed in sub-polar and subtropical regions (Whitney et al., 2007; Stramma et al., 2008). Climate models predict that dissolved oxygen concentrations in the ocean will continue to decline with the warming of the deep-sea resulting in the expansion of oxygen minimum zones

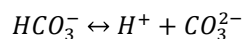
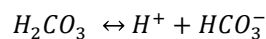
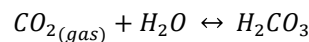
(Sarmiento and Orr, 1991; Sarmiento et al., 1998; Schmittner et al., 2008; Shaffer et al., 2009) and a significant expansion of bottom water anoxia ($<10 \mu\text{mol O L}^{-1}$).

1.2 Biogeochemical cycles and dissolved oxygen distribution in the ocean

1.2.1 Marine carbon cycle

In order to investigate how dissolved oxygen will respond to atmospheric CO_2 emissions, it is important to understand how the biogeochemical cycles are affected by atmospheric changes. The ocean contains 60 times more carbon than the atmosphere and therefore exerts a strong control over atmospheric CO_2 (Honisch et al., 2012). Over the ocean, atmospheric pCO_2 is influenced by the air-sea gas exchange and solubility as well as the concentration of dissolved inorganic carbon (DIC) and alkalinity at the sea surface. The air-sea gas exchange rate is dependent on sea surface temperature and wind speed and the solubility is dependent on sea surface temperature and salinity.

This carbonate system consists of an equilibrium in the DIC concentrations. When gaseous CO_2 dissolves in seawater, first it is hydrated to form aqueous $(\text{CO}_2)_{\text{aq}}$, which reacts with water to form a small portion of carbonic acid (H_2CO_3). H_2CO_3 then reacts rapidly to form bicarbonate (HCO_3^-). Therefore, it is assumed that a thermodynamic equilibrium exists between $(\text{CO}_2)_{\text{aq}}$ and (HCO_3^-) . Equation 1-1 summarizes these reactions.



Equation 1-1

Surface pCO_2 in the ocean is controlled by the concentration of dissolved CO_2 in the surface water and the CO_2 solubility constants (K_0) (Weiss, 1970). The partial pressure of CO_2 can be related to the carbonate and bicarbonate ions by Equation 1-2.

$$(pCO_2)_{aq} = \frac{K_2}{K_0 * K_1} * \frac{[HCO_3^-]^2}{CO_3^{2-}}$$

Equation 1-2

Where: $K_0 = \frac{[CO_2]_{aq}}{pCO_2}$

$$K_1 = \frac{[H^+] * [HCO_3^-]}{[H_2CO_3^*]}$$

$$K_2 = \frac{[H^+] * [CO_3^{2-}]}{[HCO_3^-]}$$

The sensitivity of pCO_2 to temperature and salinity can be estimated for a closed system (where DIC and alkalinity remains constant) by Equation 1-3 and Equation 1-4 (Sarmiento and Gruber, 2006). Spatial variability is greater in temperature than salinity, thus temperature can be regarded as the more dominant physical factor effecting pCO_2 .

$$\gamma_t = \frac{1}{pCO_2} * \frac{\partial pCO_2}{\partial T}$$

Equation 1-3

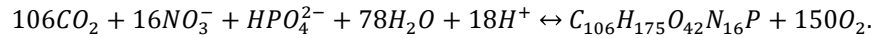
$$\gamma_s = \frac{S}{pCO_2} * \frac{\partial pCO_2}{\partial S}$$

Equation 1-4

where γ_t is the sensitivity of pCO_2 to temperature and γ_s is the sensitivity of pCO_2 to salinity.

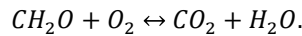
Another important component of the marine carbon cycle is the biological pump, which is a strong control of the vertical DIC and alkalinity distributions of the ocean. Total ocean alkalinity is the measure of the negatively charged ions in the sea water (HCO_3^-

and CO₃). During photosynthesis CO₂ is taken up by organisms to form organic matter by the following equation (Sarmiento and Gruber, 2006):



Equation 1-5

Hydrogen, carbon, nitrogen, oxygen, and phosphorus are found in approximately constant stoichiometric ratios in marine organic matter (Redfield, 1934). Phytoplankton organisms take up nutrients and carbon with sufficient amount of insolation, temperature, and mixing to form organic matter (e.g. Berger et al., 1989). Within the euphotic zone a significant portion of organic material is remineralized leading to an increase in the DIC concentration and a decline in dissolved oxygen:



Equation 1-6

The remaining particulate organic matter is exported from the euphotic zone into the deep sea and partially deposited on the ocean floor.

Incident solar radiation, temperature, and nutrient supply stimulate the biological pump. Light is a key factor in biological productivity, if the light is insufficient for photosynthesis the biological pump will not function. The strength of the biological pump is the magnitude of the downward flux of organic matter. The Biological pump efficiency (E_{BP}) is a measure of the success of phytoplankton in maintaining a low nutrient concentration at the surface of the ocean and is defined by Equation 1-7. One hundred percent efficiency in the biological pump would result in a nutrient concentration of zero in the surface water. A weak biological pump will result in high nutrient concentration at the surface as well as limited organic matter export. The nutrients concentration of ocean's surface water comes primarily from the main thermocline by upwelling, convective overturning, vertical mixing, and river input.

$$E_{BP} = \frac{C_{deep} - C_{surface}}{C_{deep}}$$

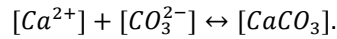
Equation 1-7

The biogenic formation and dissolution of calcite or aragonite is also important in the carbon cycle and maintaining the ocean's pH. Calcium carbonate occurs in the ocean mostly in the form of calcite, which represents a significant fraction of deep ocean sediments, if the sea floor is above the calcium carbonate compensation depth (CCD).

Coccolithophorids, foraminifera, and pteropods are the dominant groups of marine organism responsible for the precipitation of CaCO_3 in the open ocean. It has been hypothesized (Paasche, 1969; Sikes and Wilbur, 1980) that calcification could be linked to photosynthesis, as the formation of CaCO_3 from HCO_3^- produces aqueous CO_2 , which can then be used as a source of inorganic carbon for photosynthesis. However, most of the organisms that precipitate CaCO_3 in today's ocean are relatively young. Due to limited fossil record evidence, it is difficult to determine the existence of calcifiers prior to the evolution of coccolithophorids, which emerged in the mid-Triassic (~228 Ma). Foraminifera appear in the mid-Jurassic (~170 Ma). Prior to the Triassic, there were only shallow water benthic organisms forming biogenic CaCO_3 and there has been essentially no fossil record of open ocean planktonic organisms that would have precipitated CaCO_3 (Sarmiento and Gruber, 2006; Falkowski et al., 2007).

Global estimates of the open ocean CaCO_3 export are of the order of 1 PgC yr^{-1} . Once the CaCO_3 particles leave the ocean surface they are subject to dissolution below the lysocline, the boundary between well preserved and poorly preserved foraminifera. Below the lysocline is the CaCO_3 compensation depth (CCD). The hydrographic calcite lysocline is defined as the depth at which the $[\text{CO}_3^{2-}]$ is equal to the calcite saturation

horizon or as the depth at which $[Ca^{2+}]$ and $[CO_3^{2-}]$ is in equilibrium with the $[CaCO_3]$ (Equation 1-8):



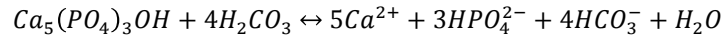
Equation 1-8

The saturation level for calcite is at ~2800 m in the equatorial Pacific Ocean and ~4000 m in the equatorial Atlantic Ocean (Feely et al., 2004). Carbonate particles are among the fastest to settle to the ocean floor with sinking velocities ranging from 100 m to over 300 m day⁻¹ (Broecker and Peng., 1982). Such rapid sinking results in a residence time in the deepest parts of the ocean of about 50 days and the majority of this time is spent in the supersaturated zone above the lysocline. The degree to which settling CaCO₃ particles dissolve in the water column depends on how fast the dissolution reaction is relative to the time it takes for the particle to settle to the bottom of the ocean. The high burial rate of CaCO₃, which is approximately balanced in the present by riverine input of weathered continental rock, leads to a reduction of alkalinity of the ocean water. On long time scales CaCO₃ content of marine sediments are important to sequester anthropogenic CO₂ (Archer et al., 2009) and are thus a crucial component of the global carbon cycle.

1.2.2 Marine phosphorus cycle

The phosphorus cycle in the past has been driven primarily by tectonics (changes in terrestrial weathering) and sea level change. During the glacial/interglacial periods changes in sea level affected the area of continental margin available as a phosphorus sink and mountain chain formations increase the amount of weathering and thus the amount of phosphorus reaching the oceans. The terrestrial weathering process of phosphorus from apatite mineral occurs by Equation 1-9 and then transported by rivers as either particulate or dissolved phosphorus (Filippelli, 2008). Soluble forms of phosphorus are limited in the environment and in most areas in the ocean PO₄ is the

limiting nutrient for primary productivity. Dissolved phosphorus concentrations at the surface are reduced by primary producers during photosynthesis (Equation 1-5).



Equation 1-9

In the deep sea phosphorus can be divided into preformed (Equation 1-10) and remineralized phosphorus (Equation 1-11) (Sarmiento and Gruber, 2006).

$$[PO_4^{3-}]_{pref} = [PO_4^{3-}]_{obs} - \Delta[PO_4^{3-}]_{remin}$$

Equation 1-10

$$\Delta[PO_4^{3-}]_{remin} = -r_{P:O_2} AOU$$

Equation 1-11

$$AOU = [O_2]_{sat} - [O_2]_{obs}$$

Equation 1-12

where $r_{P:O_2}$ is the phosphorus to oxygen ratio and AOU is the apparent oxygen utilization (Equation 1-12).

Preformed phosphorus is not utilized by organisms and is thus a useful water mass tracer (Filippelli, 2008). The ocean exhibits a clear gradient in preformed phosphorus between the high preformed phosphorus and low saline waters of the Southern Ocean and the low preformed phosphorus concentration and high salinity of the North Atlantic. In the deep ocean phosphorus concentration increases with the age of the water mass; therefore, the older waters of the Pacific have higher phosphorus concentrations than that of the Atlantic (Broecker and Peng, 1982; Sarmiento and Gruber, 2006).

The marine phosphorus deposition in present ocean sediment is nearly balanced by the natural riverine supply of phosphorus to the ocean. Phosphorus can be buried and

precipitated as authigenic carbonate fluorapatite or buried as biogenic Ca-P in anoxic conditions (Figure 3-1) (Slomp et al., 1996; Filippelli, 2001; Filippelli, 2002; Slomp et al., 2002; Filippelli et al., 2003; Slomp et al., 2004). Preferential regeneration of phosphorus relative to carbon can also release regenerated phosphorus back into the water column, which affects the concentration at the sediment-water interface. With sufficient mixing the phosphorus-rich bottom water could be returned to the surface affecting productivity (Van Cappellen and Ingall, 1994; Van Cappellen and Ingall, 1996; Filippelli, 2002; Slomp et al., 2002; Filippelli et al., 2003; Slomp et al., 2004; Filippelli, 2008).

The modern phosphorus cycle is altered by anthropogenic process e.g. by the supply of dissolved phosphorus and phosphorus-bearing particulates in the world's rivers. During the last 200 years the amount of riverine phosphorus reaching the ocean surface has doubled (Filippelli, 2002; Walling and Fang, 2003). This change is occurring due to alterations in land use and agriculture; however, the response of the ocean to the perturbation in phosphorus will likely have comparable feedbacks as those of the phosphorus changes of the glacial-interglacial cycles.

1.2.3 Dissolved ocean oxygen distribution

The solubility and biological pump (Volk and Hoffert, 1984) are both influenced by ocean circulation and govern the distribution of dissolved oxygen in the ocean. Oxygen enters the surface of the ocean through the gas exchange between the surface and the atmosphere and to a lesser degree dissolved O₂ in the ocean is also produced in the photic zone by organism through photosynthesis (Equation 1-5). The surface waters can be slightly supersaturated or under saturated with oxygen possibly due to bubble entrainment or seasonal variations; however, globally the oxygen concentration in the atmosphere and surface of the ocean are near equilibrium (Broecker and Peng, 1982).

The solubility of oxygen in the surface waters is directly related to salinity and the sea surface temperature (SST) as defined by Weiss (1970).

Sources of O₂ are balanced by the reduction of oxygen by remineralization as organic matter is delivered to the deep sea and the oxidation of organic matter in sediments. Sulfate reduction and denitrification also occur in today's oceans but have a negligible effect on oxygen concentration. Two processes for oxygen loss in the deep sea (oxygen sinks) are carbon remineralization and by biochemically oxidizing ammonia to nitrate. Oxygen is consumed by one O₂ molecule for every carbon atom remineralized and by two O₂ molecules for every nitrogen atom oxidized in the following equation (Richards et al., 1965; Broecker and Peng, 1982; Shaffer, 1996):



Equation 1-13

The oxygen minimum zone (OMZ) at intermediate depth is the zone at which oxygen saturation is the lowest in the water column. This minimum is linked to a high remineralization of POC and thus according to Equation 1-6 high consumption of dissolved oxygen. The core in the OMZ was defined in this study to have a dissolved oxygen concentration of $\leq 20 \mu\text{mol L}^{-1}$ O₂ consistent with (Helly and Levin, 2004; Fuenzalida et al., 2009; Paulmier et al., 2011). The OMZ boundaries were described to have a dissolved O₂ concentration of $\leq 50 \mu\text{mol L}^{-1}$. The maximum dissolved oxygen concentration of $50 \mu\text{mol L}^{-1}$ was more stringent than upper limits in other studies (Whitney et al., 2007; Karstensen et al., 2008); however, at these dissolved O₂ concentrations most microorganisms cannot survive (Kamykowski and Zentara, 1990; Gray et al., 2002; Sarmiento and Gruber, 2006; Paulmier et al., 2011) and therefore considered a reasonable criterion for non-seasonal OMZ.

Chapter 2

Objectives

2.1 Introduction

The geological record of the early Cenozoic indicates that on shorter timescales, atmospheric CO₂ concentrations and temperature can change rapidly; however, the residence time of carbon in the ocean sediments is about 10 kyr-100 Ma (Sarmiento and Gruber, 2006). Thus the removal of the increased carbon emission since the industrial revolution will have long-term effects on seawater chemistry and deep-sea sediment composition (Archer et al., 2009). On time scales of thousands of years it has been estimated that the world's oceans will sequester ~20-35% after a few centuries (Chapter 1; Archer et al., 2009) and 90% of anthropogenic carbon emissions on the geologic time scale of 100,000 years (Archer et al., 1998), but positive and negative feedbacks between the climate and biogeochemical cycles are still not well quantified (Heinze, 2004). This study will explore how expected future carbon and dust deposition perturbation can alter the dissolved oxygen distribution in deep-sea. For all simulations in this study the model applied is the Hamburg Oceanic Carbon Cycle Model (HAMOCC 2.0; Maier-Reimer and Hasselmann, 1987; Heinze et al., 1991; Palastanga et al., 2011). An overview of the simulations is summarized in Table 2-1.

2.2 Response of the oxygen minimum zone and pH value to CO₂ radiative forcing

The main objective of this study is to examine the solubility and the biological pump effect on dissolved oxygen concentration in the ocean with a focus on the oxygen minimum zone, which are in the twilight zone to intermediate depth. The study also considers the pH response to anthropogenic CO₂ emission.

An Increase in radiative forcing by anthropogenic CO₂ emissions is likely to have impacts on the sea surface temperature, ocean circulation, export production, and vertical carbon flux in the ocean. Figure 2.1 illustrates how anthropogenic CO₂ can lead to expansion of oxygen minimum zones via changes in sea surface temperature and export production. These changes will affect the global dissolved oxygen concentrations as well as the extent and strength of oxygen minimum zones (OMZs) (Winguth et al., 2005; Schmittner et al., 2008; Moore et al., 2013). There is strong evidence that dissolved O₂ concentrations in tropical OMZ of the North Pacific as well as subarctic zone is declining in recent decades (Stramma et al., 2008; Keeling et al., 2010; Stramma et al., 2012).

Low dissolved oxygen concentration in the ocean during climate changes in the geological past have been linked to major changes in the ecological structure of the ocean as well as mass extinctions (Grotzinger and Knoll, 1995; Knoll et al., 1996; Isozaki, 1997; Benton and Twitchett, 2003). Rapid expansion and contraction of OMZs during the glacial-interglacial cycles has also been noted which suggest a strong link between dissolved oxygen concentration and climate (Ganeshram et al., 2002; Galbraith et al., 2004; Nameroff et al., 2004). Sensitivity experiments with HAMOCC 2.0 were carried out to address the following questions:

- (1) How sensitive is the lateral and vertical expansion of the oxygen minimum zones to an increase in atmospheric CO₂ radiative forcing and the associated rise in the sea surface temperature and changes in the biological pump? Do fluctuations of vertical particulate organic matter flux to the intermediate depth by climate change alter the oxygen minimum zone and its cores? Could there be a development of a North Atlantic oxygen minimum zone or low oxygen zone in a warmer climate?

The expansion of OMZs has been observed in the recent decades as the temperature of the world's oceans increases (Whitney et al., 2007; Stramma et al., 2008; Fuenzalida et al., 2009; Stramma et al., 2009) and models predict further decreases in oxygen concentrations with increased atmospheric $p\text{CO}_2$ emissions (Sarmiento et al., 1998; Matear et al., 2000). Oxygen minimum zones are not only important to the ecosystem structures but also influence locally the nitrogen cycle because denitrification occurs in low oxygen environments. Denitrification converts NO_3^- to N_2O (also CH_4 and H_2S) which is released to the atmosphere as a greenhouse gas thus causing a positive feedback in the climate system. Paulmier (2011) concluded that dissolved oxygen concentration of $<20 \mu\text{mol L}^{-1}$ currently covers ~8% of the global ocean area at the surface of the OMZs, which is greater than previous estimates (Kamykowski and Zentara, 1990). This study will focus on the OMZ cores and causes their expansion under a changing climate change which could play an increasing role by affecting the global carbon cycle due to the influence of the decline of dissolved O_2 on the rate of remineralization of organic matter and the burial of organic matter in ocean sediments.

(2) Could future ocean acidification be amplified by hypoxia in the response to global climate change?

Observations indicate that the ocean pH is becoming more acidic and therefore increasing CaCO_3 dissolution resulting in an increase in carbon burial in deep-sea sediments, which could increase the ocean ability to uptake CO_2 for the atmosphere. A complete decline in calcification in surface waters would be able to reduce the $p\text{CO}_2$ by 10-20 μatm (Feely et al., 2004).

Changes in pH may be also amplified by global climate change Melzner et al., (2012) because hypoxic conditions in coastal margins may lead to a further decrease in pH due to reparatory processes. Therefore, the $p\text{CO}_2$ -induced acidification may be

further compounded by the loss of oxygen due to decreased solubility in a warmer ocean. Rapid acidification could severely impair primary productivity. Beyond this, the decreased pH of seawater will impair protein functions of lower marine organisms as the organism's tissue will also become acid. One key protein affected by acidification is the oxygen-binding protein. Loss of oxygen-binding protein could lead to an increase in the dissolved oxygen concentration required for the organism to survive. This study will following the concept of Melzner et al. (2012) examine how the pH value change under different anthropogenic CO₂ emission scenarios in response to the decline of dissolved oxygen in the ocean.

2.3 Reduced biology and atmospheric oxygen concentration experiments

The biological pump is a strong control for the distribution of dissolved oxygen in the ocean. Dissolved oxygen is produced at the surface of the ocean by photosynthesis and is reduced below the photic zone by the remineralization of POC as organic material produced at the surface sink to the deep sea. Therefore, significant changes primary productivity would lead to significant changes in dissolved oxygen concentrations and distribution in the ocean.

- (1) How would dissolved oxygen and DIC be distributed in the ocean in the absence of the biological pump? Would this result in large changes in total alkalinity and pH?

Although most dissolved oxygen at the ocean surface is due to the air-sea gas exchange of oxygen, a complete extinction of primary producers could lead to slightly decreased dissolved O₂ concentrations in the ocean's surface waters. However, the lack of POC flux to the deep sea would have much more profound implication on dissolved oxygen concentrations due to the lack of remineralization of organic matter. The lack of remineralization could lead to much higher DIC, alkalinity, and O₂ concentration in the

deep sea and thus more carbon burial in deep ocean sediments leading to higher $p\text{CO}_2$ uptake from the atmosphere. This study investigates changes in dissolved oxygen and DIC concentrations and distribution in the deep sea as well as the resultant change in alkalinity and pH.

- (2) How are dissolved oxygen concentrations and the solubility of O_2 at the sea surface affected by changes in the atmospheric oxygen concentration?

Oxygen in the atmosphere and dissolved oxygen at the ocean surface are presumed to be at equilibrium (Broecker and Peng, 1982). This study investigates changes in oxygen solubility at the sea surface and oxygen concentrations at depth in response to decreased atmospheric oxygen concentration.

2.4 Fe fertilization experiments

Prediction of future atmospheric dust concentrations is problematic due in part due to direct uncertain anthropogenic influence (Dale, 1997; Foley et al., 2005; Jickells et al., 2005; Neff et al., 2008) including atmospheric Fe from combustion (Ito et al., 2012). Predictions range from large increases to large decreases in dust deposition to the ocean in the future (Harrison et al., 2001; Tegen et al., 2004; Woodward et al., 2005; Mahowald et al., 2006). Fe is a limiting nutrient and therefore important to the biological pump and thus the dissolved oxygen concentration in the ocean. This study examines the response of ocean oxygen concentration to ocean Fe fertilization changes due to fluctuations in atmospheric dust with increase atmospheric CO_2 emissions.

- (1) How would possible changes to atmospheric dust affect oxygen minimum zones due to changes in Fe fertilization? Would an increase in atmospheric dust deposition result in increased export production of particulate organic carbon in regions that are not Fe limited?

Iron is a rate-limiting micronutrient critical to ocean primary productivity and limits primary productivity in regions which have a high-(macro) nutrient availability but low-chlorophyll concentration (Martin, 1990; Behrenfeld et al., 1996). Export production can be reduced or enhanced by atmospheric dust concentration (Hand et al., 2004; Maher et al., 2010; Martínez-García et al., 2011). Dust deposition from deserts was reduced by 20-60% in the next century in a study by Mahowald and Luo (2003). One scenario from this study exhibited a reduction of desert dust of a 9-24% since pre-industrial times. Other modeling studies have indicated an increase in dust deposition in this same time span (Tegen et al., 2004; Woodward et al., 2005; Mahowald et al., 2007; Mahowald et al., 2009). Observations from ice cores (McConnell et al., 2007) and lake sediments (Neff et al., 2008) suggest that atmospheric dust has increased in the last 100 years. Dust deposition could be altered in the future due to increased rainfall, melting ice sheets, desertification, and increased storm activity (Eisenman et al., 2009). However, these data are limited and therefore future changes in dust concentration remains uncertain. In this study, we examine the response of the biological pump and related dissolved oxygen content to significant changes in the Fe fertilization from atmospheric dust.

- (2) Could reduced atmospheric dust deposition in the future mitigate the expansion of OMZ with increased pCO₂ emission?

If atmospheric dust deposition is reduced due to future climate change the areas of ocean which are Fe-limited could expand. This expansion would reduce primary productivity and export production of POC and thereby reduce the loss of dissolved oxygen due to remineralization in the twilight and intermediate depths. The loss of primary productivity would hinder the ocean's ability to sequester CO₂ from the atmosphere; however preserving the dissolved oxygen concentrations within the oxygen minimum zone.

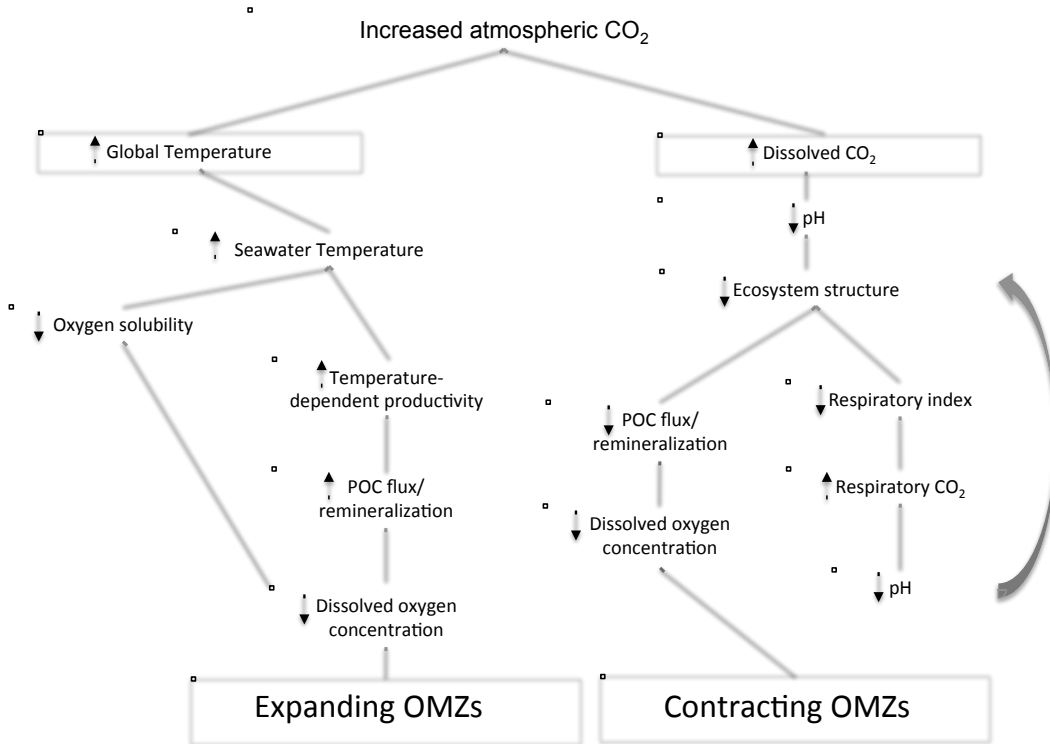


Figure 2-1 Flow diagram of the impacts of atmospheric CO₂ on OMZs.

Table 2-1 Summary of Experiment

Summary of Experiments

Experiments		
Increased pCO ₂ without Radative Forcing	Increased pCO ₂ with Radative Forcing	Brief Description
Oxygen Distribution and pH Experiments		
1 X CO ₂		Reference simulation with preindustrial atmospheric CO ₂ levels (278 ppmv). The reference simulation is integrated for 30,000 years.
2 X CO ₂ _CC_nf	2 X CO ₂ _CC_f	Experiments with no feedbacks (nf) have an increase of pCO ₂ of 1% per year without temperature change. Temperature changes are applied in experiments with feedbacks (f) as a function of pCO ₂ after Hansen et al. (1988). Each simulation is integrated for 30,000 years.
3 X CO ₂ _CC_nf	3 X CO ₂ _CC_f	
4 X CO ₂ _CC_nf	4 X CO ₂ _CC_f	
6 X CO ₂ _CC_nf	6 X CO ₂ _CC_f	
8 X CO ₂ _CC_nf	8 X CO ₂ _CC_f	
Reduced Atmospheric Oxygen Concentration and Extinction Experiments		
Kill_atmO ₂ _50		Oxygen solubility simulations include preindustrial pCO ₂ levels and reduced atmospheric O ₂ and reduced primary productivity. Kill_atmO ₂ _50 was simulated with present day productivity with atmospheric O ₂ reduced by 50%. Kill_all_prod was simulated with primary productivity (POC, Si, CaCO ₃) reduced to 1X10 ⁻²⁰ PgC yr ⁻¹ and present day atmospheric O ₂ concentrations. A final experiment (Kill_all_prod_50) include the extinction of primary producers (1X10 ⁻²⁰ PgC yr ⁻¹) and a 50% reduction in atmospheric O ₂ . Each simulation is integrated for 1,000 years.
Kill_all_prod		
Kill_all_prod_50		
Fe Fertilization Experiments		
1 X CO ₂	4 X CO ₂	Fe experiments were simulated by increasing (+50%) and decreasing (-50%) the dust fields of Mahowald et al. (2006) globally. These experiments do not consider land use change. Fe fertilization simulation with no feedbacks (nf) include only changes in dust with no increase pCO ₂ . Feedbacks are considered in the simulation at 4 times preindustrial (f) including temperature change after Hansen et al. (1988). Fe fertilization sensitivity experiments are integrated for 15,000 years.
1 X CO ₂ DUST+50%	4 X CO ₂ DUST+50%	
1 X CO ₂ DUST-50%	4 X CO ₂ DUST-50%	

Chapter 3

HAMOCC 2.0 Model Description and Reference Simulation

3.1 Model description

This study is conducted with the Hamburg Oceanic Carbon Cycle Model Version 2.0 (HAMOCC 2.0) that is expanded with an iron cycle, sedimentary phosphorus cycle and improved atmospheric dust parameterization (Palastanga et al., 2011; Palastanga et al., 2013). The original HAMOCC was developed by Maier-Reimer and Hasselmann, (1987) and Heinze et al., (1991) and designed for long-term carbon cycle simulations of several 10,000 years and is integrated with an annual time step.

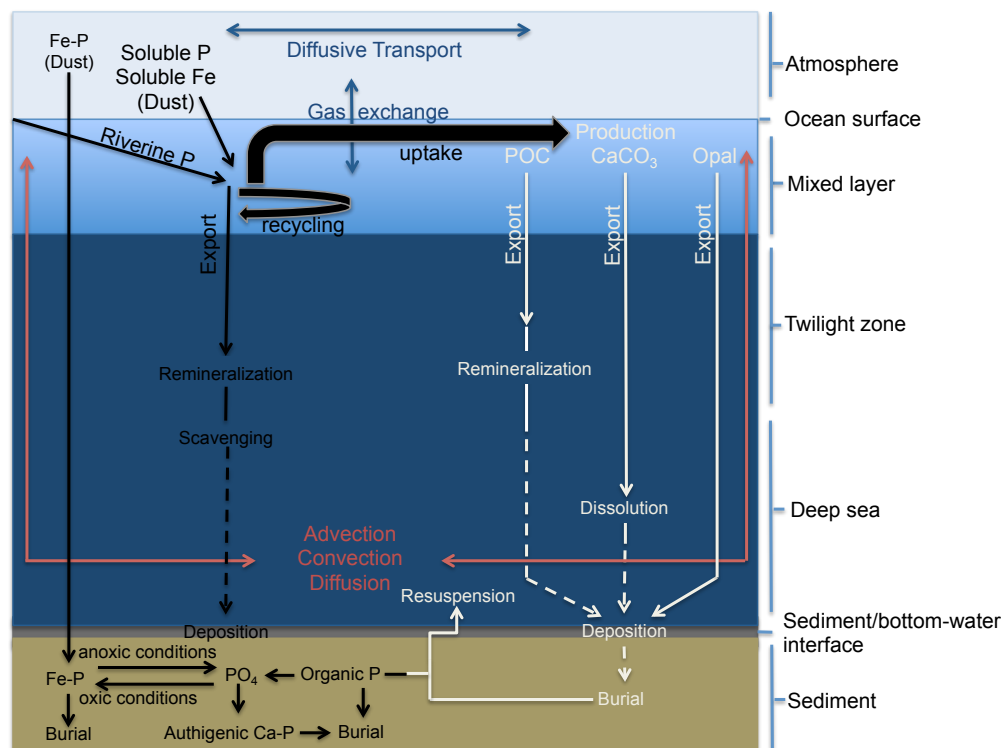


Figure 3-1 Schematic model concept diagram including the sediment biogeochemical cycling of sedimentary phosphorus (after: Heinze et al., 1991; Palastanga et al., 2011).

The model has a horizontal resolution of $\sim 3.5^\circ \times 3.5^\circ$ and utilizes an E-grid (Arakawa and Lamb, 1977) and resolves the equatorial upwelling belt by grid points 1.25° north and south of the equator. The model provides 11 vertical layers (centered at 25, 75, 150, 250, 450, 700, 1000, 2000, 3000, 4000, and 5000 meters) with a total depth of 5000 meters (Heinze et al., 1999; Heinze, 2004; Heinze et al., 2006). HAMOCC 2.0 includes one 10 cm thick layer of bioturbated sediment, which is further divided into 11 sub-layers. Transport tracers are simulated using flow fields from the Hamburg large-scale geostrophic model (LSG; Maier-Reimer et al., 1993).

Table 3-1 List of model tracers

Model Tracers	
Water Column	
Dissolved	Solids
Total Alkalinity	Calcium Carbonate (CaCO_3)
Total CO_2 (DIC)	opal
Phosphate (PO_4)	clay
Oxygen (O_2)	Particulate Organic Carbon (POC)
Dissolved Organic Carbon (DOC)	
Silicic acid	
Sediment	
Porewater	Solid
Total Alkalinity	Calcium Carbonate (CaCO_3)
Total CO_2	opal
Phosphate (PO_4)	clay
Oxygen (O_2)	Particulate Organic Carbon (POC)
Silicic acid	

Advection of tracers (Table 3-1) are modeled iteratively by the following tracer equation:

$$\frac{dc}{dt} = -\text{div}(\vec{v} \cdot c) - q.$$

Equation 3-1

where \vec{v} is the velocity vector and q is sources and sinks due to atmospheric exchanges, riverine input, sedimentary loss, and biogeochemical processes within the ocean. The

advection of tracers are numerically iteratively solved by an upstream formulation (Equation 3-2) at each vertical level (Maier-Reimer and Heinze, 1992).

$$\frac{c^{t+\Delta t} - c^t}{\Delta t} = - \sum_i v_i * \frac{c_i^{t+\Delta t} - c^{t+\Delta t}}{\Delta x_i} - q_i$$

Equation 3-2

where v_i is the velocity component in the direction of grid point i , Δx_i is the distance to the neighboring grid point i , c_i is the tracer concentration at the neighboring grid point i , and q_i is the sources and sinks and grid point i .

Atmospheric CO_2 and O_2 concentrations are exchanged between the ocean surface (top 50 m) and zonally mixed atmospheric boxes via the air-sea gas exchange equations for CO_2 and O_2 . The air-sea gas exchange flux (F_{CO_2}) is determined by the difference in the partial pressure of CO_2 ($p\text{CO}_{2(\text{sea})}$) in the sea surface and the atmospheric $p\text{CO}_2$ ($p\text{CO}_{2(\text{atm})}$) at each grid point where λ denotes the gas exchange coefficient (Heinze et al., 1991):

$$F_{\text{CO}_2} = \lambda_{\text{CO}_2} (p\text{CO}_{2(\text{atm})} - p\text{CO}_{2(\text{sea})}).$$

Equation 3-3

The gas exchange flux of oxygen (F_{O_2}) is an order of magnitude faster than that of CO_2 (F_{CO_2}) and is carried out according to a fixed transfer velocity and is assumed to be at equilibrium between the atmospheric layer and the surface water at the temperature-dependent saturation level:

$$F_{\text{O}_2} = \lambda_{\text{O}_2} (p\text{O}_{2(\text{atm})} - p\text{O}_{2(\text{sea})}).$$

Equation 3-4

where λ_{O_2} is a fixed gas exchange transfer coefficient based on a fixed gas transfer velocity of O_2 at 250 m yr^{-1} . The solubility of dissolved oxygen depends on temperature, salinity, and pressure (Weiss, 1970). Oxygen concentrations are determined at each grid

point and every depth level. The O₂ flux into the atmosphere can be neglected since the atmospheric concentration of O₂ is by far larger than the concentration of O₂ at the ocean surface.

The annual export production of particulate organic carbon (P_{POC}) from the euphotic zone is calculated via Michaelis Menten kinetics for nutrient uptake (Takahashi and Parsons, 1973; Heinze et al., 1991) by:

$$P_{POC} = \frac{V_{max}^{POC} * [PO_4^{3-}]^2 * red(C:P)}{K_s^{POC} + [PO_4^{3-}]}$$

Equation 3-5

where V_{max}^{POC} is the maximum uptake rate of PO₄ per year as a function of sea surface temperature (SST) in °C. V_{max}^{POC} is determined by:

$$V_{max}^{POC} = C_{V1} + SST * \frac{C_{V2}}{T_{max} - T_{min}}$$

Equation 3-6

where T_{max} = 25°C and is the maximum temperature and T_{min} = 0.1°C which is the lower temperature cut off value. C_{V1} and C_{V2} are adjustable values of 0.3 yr⁻¹ and 0.7 yr⁻¹ respectively. K_s^{POC} denotes the half saturation constant for POC production and red (C:P) is the C to P Redfield ratio of 122:1 (Takahashi et al., 1995).

Export production of opal (P_{opal}) is calculated via Michaelis Menten kinetics for silicic acid uptake (Heinze et al., 1991; Heinze et al., 2003) by:

$$P_{opal} = \frac{V_{max}^{opal} * [Si(OH)_4]^2}{K_s^{opal} + [Si(OH)_4]}$$

Equation 3-7

where $V_{max}^{opal} = V_{max}^{POC} * 2.5$ and is the maximum uptake rate of silicic acid per year and K_s^{opal} denotes the half saturation constant for opal production.

CaCO₃ production (P_{CaCO_3}) is dependent on the particulate organic and opal production and a threshold value:

$$P_{CaCO_3} = P_{org} * R_{max} * \left(1 * \frac{P_{Si}}{P_{org}/th} \right),$$

Equation 3-8

where R_{max} denotes the maximum value for the rain ratio of $C_{POC}:C_{CaCO_3}$ and th is the threshold value for CaCO₃ production. This relationship is based on the assumption that in the present day ocean there is a dominance of the silicate producers (e.g. diatoms) over the calcareous plankton (e.g. coccolithophores) (Falkowski et al., 2007). The amount of CaCO₃ production is inversely proportional to the Si(OH)₄ concentrations, as silicate acid decreases CaCO₃ production increases. In the current version of the model the maximum value for the ratio of $C_{POC}:C_{CaCO_3}$ is equal to 0.197 and the threshold for CaCO₃ production is 0.7. Equation 3-8 calculates CaCO₃ production for P_{Si}/P_{org} less than the threshold value (th). If P_{Si}/P_{org} is greater than the threshold value the third term is equal to zero.

All particulate matter in the model is redistributed vertically to the deep through the particle flux (Equation 3-9), which is assumed to exponentially decline with depth (Heinze et al., 1991).

$$F_{POC} = F_1 + F_2$$

$$F_1 = \frac{P_{POC}}{0.0238z + 0.212}$$

$$F_2 = (P_{POC} - F_1(50m) - S_{POC})e^{-z/d_p} + S_{POC}$$

Equation 3-9

Where P_{POC} is the annual production of POC, S_{POC} is the part of the P_{POC} that sinks immediately to the bottom layer, z is the depth, and d_p is the e-folding depth.

POC flux parameterization does not consider the ballasting effect of minerals from organism or clay and is calculated by the concentration of POC¹² at each depth multiplied by a uniform sinking rate (*w*) for all particles at all depths of 120 m day⁻¹ (Martin et al., 1987). The POC flux exported from the surface into the deep sea is determined from organic carbon production multiplied by the thickness of the uppermost layer, the euphotic zone.

Remineralization of organic matter depends on the fixed Redfield ratio and oxygen consumption in the water column. Concentration of particulate organic carbon (POC) remineralization occurs as long as dissolved O₂ is larger than the minimum O₂ concentration for bacterial decomposition of POC [O_{2min} = 10⁻⁵ mol L⁻¹]. The amount of oxygen available for remineralization of organic matter (O_{2av}) depends on the particulate organic carbon concentration:

$$\begin{aligned}
 & \text{for } \left(\frac{[O_2] - [O_{2min}]}{O_{2RR}} \right) \geq [POC] \\
 & \quad O_{2av} = r_z * POC \\
 & \text{and for } \left(\frac{[O_2] - [O_{2min}]}{O_{2RR}} \right) < [POC] \\
 & \quad O_{2av} = r_z * \left(\frac{[O_2] - [O_{2min}]}{O_{2RR}} \right)
 \end{aligned}$$

Equation 3-10

where *r_z* denotes the POC remineralization rate in the water column at each depth and O_{2RR} is the Redfield ratio of O₂:C (172:122). The POC remineralization rate (*r_z*) is set to 1 at the surface and 0.05 for all other layers. Once the amount of O₂ consumed and remineralized POC are calculated O_{2av} reduces dissolved oxygen and the concentration of POC and increases of [PO₄³⁻] and the concentration of DIC with the stoichiometric ratios based on the Redfield ratio of Takahashi et al. (1995). Increase in alkalinity is

considered by the dissolution of calcareous shells and the increase of nitrate by the remineralization assuming the Redfield ratio of N:C (16:122).

HAMOCC 2.0 includes a sediment module with porewater and solid components (Table 3-1) that are couple by a reaction rate. For a more detailed description of the sediment module see Heinze (1991; 2004) and Heinze et al. (1999). Diffusive transport and porewater reactions (reduction of undersaturation) occur via Equation 3-11

$$\frac{dU}{dt} = \frac{\partial}{\partial z} \left(D_w \frac{\partial U}{\partial z} \right) - G$$

Equation 3-11

where U is the deviation from the saturation concentration (undersaturation), G is the reaction rate, and D_w is the diffusion coefficient for porewater diffusion of $8 \times 10^{-6} \text{ cm}^2 \text{ yr}^{-1}$. Porewater diffusion and chemical reactions within the porewater are accomplished simultaneously. Equation 3-12 and Equation 3-13 calculate the final concentration for solid and porewater components.

$$S_*^{t+\Delta t} = S_*^t - \Delta t \cdot r_c^* \cdot U^{t+\Delta t} \cdot \frac{S_*^t + Q \cdot \Delta t}{1 + \Delta t \cdot r_c^* \cdot U^{t+\Delta t}} + \Delta t \cdot Q$$

Equation 3-12

$$P^{t+\Delta t} = P_{sat} - U^{t+\Delta t}$$

Equation 3-13

where r_c is the reaction rate, U is the deviation from saturation concentration, Q is the gain from particle rain, and P_{sat} is the saturation concentration in solution.

In order to account for the degradation of organic matter in anaerobic conditions, remineralization of the POC concentration in the sediments becomes active for the pore water $[O_2] < [O_{2crit}]$ with $O_{2crit} = 5 \mu\text{mol L}^{-1}$ (Palastanga et al., 2011). The oxic pathway (Equation 3-14) is not dependent on oxygen concentration and occurs in sediments where the porewater $[O_2] \geq [O_{2crit}]$.

$$G_c = G_{c_{ox}} = k_{ox} * POC$$

Equation 3-14

If the pore water $[O_2] < 5 \mu\text{mol L}^{-1}$ then the anaerobic pathway (Equation 3-15) which is dependent on the dissolved oxygen concentration, is activated:

$$G_c = G_{c_{ox}} + G_{c_{ax}} = k_{ox} * [POC] * \left(\frac{[O_2]}{[O_{2crit}]} \right) + k_{ax} * [POC],$$

Equation 3-15

where G_c denotes the net rate of POC degradation, $G_{c_{ox}}$ is the aerobic rate of POC degradation of [POC], $G_{c_{ax}}$ is the anaerobic rate of the degradation of [POC], k_{ox} is first order kinetic constant for aerobic remineralization of [POC], and k_{ax} denotes the first order kinetic constant for anaerobic POC mineralization and O_2 is the pore water oxygen concentration. Palastanga et al. (2011) selected k_{ox} and k_{ax} by the best fit to global observed surface POC. Different k values were selected for depths greater than 2000 meters and the more shallow margins (<2000 meters). The values for k_{ox} and k_{ax} as well as the sediment mixing rates (bioturbation) are listed in Table 3-1.

Dust deposition and sediments re-suspension are sources of dissolved Fe in HAMOCC 2.0. Total dissolved Fe is assumed to be free bioavailable inorganic Fe. The ratio of Fe fixation to POC remineralization and thus the release of Fe back into the water column is 4 μmol : 1 mol (Parekh et al., 2005; Palastanga et al., 2013). Fe is removed from the water column through scavenging by:

$$dFe = dFe_{surf} - Fe_{scav}$$

Equation 3-16

where dFe_{surf} is the dissolved Fe concentration at the surface and Fe_{scav} is the amount of Fe scavenged via Equation 3-17.

$$Fe_{scav} = \left(k_0 + k_p (POC_{flux} + CaCO_{3Flux} + Opal_{flux} + clay_{flux}) \right) * (dFe_{surf} - \alpha)$$

Equation 3-17

where k_0 is the scavenging rate constant, k_p is the particle dependent rate constant, and α is the apparent solubility constant. It is assumed that 10% of scavenged Fe is delivered to the sediments. Fe is released from the sediments as a function of POC flux from the bottom water to the sediments at a rate of $0.2 \mu\text{mol Fe m}^{-2} \text{ day}^{-1}$ for each $\text{mmol C m}^{-2} \text{ day}^{-1}$. For a more detailed description of Fe processes see Palastanga (2013), Moore and Braucher (2008), and Aumont and Bopp (2006).

In previous versions of the model particulate organic phosphorus (POP) was linked to POC by a constant Redfield ratio. Palastanga et al. (2011) introduced a new approach treating POP as a prognostic variable within the sediments subject to degradation as well as transport and burial (see figure 3-1). For $O_2 < O_{2crit}$, preferential regeneration of phosphorus from organic matter the degradation of POP is simulated by Equation 3-18.

$$G_{P_{ax}} = \alpha k_{ax} POP$$

Equation 3-18

where α is an acceleration factor for the anaerobic degradation rate of POP. The porewater PO_4 and O_2 dependent precipitation of authigenic carbonate fluorapatite (Ca-P) (Equation 3-19), formation (Equation 3-20) of Fe-oxide bound phosphorus (Fe-P) are included in the sediment module. Also include is the dissolution of Fe-P which is

dependent on the O_2 and Fe-P concentration in the sediments (Equation 3-21). The rate of precipitation (R_a) of authigenic Ca-P is defined as:

$$R_a = k_a(PO_4 - C_a)$$

Equation 3-19

where k_a is the rate constant for Ca-P precipitation, and C_a is the equilibrium concentration for Ca-P precipitation. The rate of phosphate sorption (R_s) is defined as:

$$R_s = k_s(PO_4 - C_s)$$

Equation 3-20

where k_s is the rate constant for phosphorus sorption, and C_s is the equilibrium concentration for phosphorus sorption.

$$R_m = k_m(FeP - M_f)$$

Equation 3-21

where R_m is the desorption rate of phosphorus from Fe-oxides, k_m is the rate constant for phosphorus release upon Fe-oxide dissolution, and M_f is the minimum concentration of Fe-P required for the release of phosphorus.

3.2 The reference experiment

3.2.1 Initial and boundary conditions used

The annually averaged version of the model (Heinze et al., 2006) was integrated to near equilibrium (200 kyr) at which point total global inventory of dissolved oxygen varied by $<50 \times 10^{12}$ mol per time step. The reference experiment as well as all sensitivity experiments was started from the equilibrium state. All experiments discussed below, with the exception of the iron fertilization simulations, were integrated for 30,000 yrs. For the reference experiment, the model was forced from preindustrial flow fields of the IFG simulation with a global average temperature of 19°C and a global salinity of 34.8 psu (Winguth et al., 1999). The initial condition and parameters for the reference experiment

are listed in Table 3-2 and Table 3-3. Atmospheric pCO₂ was prescribed at the preindustrial level of 279.78 ppmv.

Table 3-2 Initial conditions for the reference experiment

Initial Conditions	
Water Column	
Parameter	Value (mol L ⁻¹)
DIC	2.25 10 ⁻³
Alkalinity	2.33 (eq)
PO ₄	2.54 10 ⁻⁴
O ₂	1.65 10 ⁻⁴
Fe (dust)	6.00 10 ⁻¹⁰
Atmosphere	
Parameter	Value
pCO ₂	279.78 ppmv
O ₂	20.976 mol%

A correction factor is introduced to adjust the atmospheric pCO₂ to preindustrial conditions by:

$$pCO_{2cor} = pCO_2 * \left[1 - \left(\frac{pCO_2}{pCO_{2ref}} \right) \right]$$

Equation 3-22

where pCO_{2ref}= 279.78 ppmv is the preindustrial atmospheric pCO₂ concentration.

Export production of CaCO₃ production (Equation 3-8) is limited by the fraction of silicate production to organic carbon production with a global PIC:POC ratio of 0.181.

Table 3-3 Parameter value list for the reference experiment (after Palastanga et.al, 2011)

Parameter Values	
Parameter	Value
Rate constant for aerobic degradation of sediment POC (margins)	0.01 a ⁻¹
Rate constant for aerobic degradation of sediment POC (deep sea)	0.005 a ⁻¹
Rate constant for anaerobic degradation of sediment POC (margins)	0.008 a ⁻¹
Rate constant for anaerobic degradation of sediment POC (deep sea)	0.002 a ⁻¹
Oxygen saturation concentration for the redox boundary	5.0 μ mol L ⁻¹
Parameter for preferential regeneration of P relative to C	2
Bioturbation coefficient (z<3000m)	1.0 cm ² a ⁻¹
Bioturbation coefficient (z>3000m)	0.3 cm ² a ⁻¹
Rate constant for P sorption (margins)	36.5 a ⁻¹
Rate constant for P sorption (deep sea)	3.65 a ⁻¹
Equilibrium concentration for P sorption (margins)	0 μ mol L ⁻¹
Equilibrium concentration for P sorption (deep sea)	2 μ mol L ⁻¹
Global river input of PO ₄	2.7 Tmol year ⁻¹
Atmospheric (dust) input of PO ₄	0.3 Tmol year ⁻¹
Global river input of Opal	4.5 Tmol year ⁻¹
Global river input of CO ₃	15 Tmol year ⁻¹
Global input of Clay (margins and pelagic)	35 Tmol year ⁻¹

Annual mean dust deposition fields are taken from Mahowald et al., (2006) with a total dust deposition of 989.26 Tg yr⁻¹. In the reference experiment, the vertical POC flux does not consider the effect of mineral ballasting of POC (see section 3.1).

3.2.2 Reference Run Results and Discussion

The results of the reference experiment presented in this section were integrated 30,000 years. Prescribed temperature and salinity taken from (Winguth et al., 1999) are comparable to the observed data from the World Ocean Atlas 2013 (referred hereafter as

WOA2013; Locarmini, et al., 2013; Zweng, et al., 2013) and to the preindustrial model simulations of Maier-Reimer (1993). Simulated seawater temperature and salinity are comparable to the World Ocean Atlas 2013 at 3000 m depth. Compared to WOA2013, a cooler simulated temperature predicted for the Bering Seaby the LSG, lead to higher O₂ solubility at the surface and therefore higher dissolved O₂ concentration than the corresponding data from WOA2013 (Locarmini et al., 2013; Garcia et al., 2014). This bias may be partially linked to the long-term warming trend over the last decades (IPCC,2013). Dissolved inorganic carbon (DIC) at the surface is similar to the simulations of Maier-Reimer (1993) (Figure 3-2 and Figure 3-3) and the observations from the WOA2013 (Locarmini et al., 2013) with the exception of the Arctic region in which the reference experiment simulated DIC concentrations at approximately 150 umol/kg less than Maier-Reimer's. The decreased simulated DIC in the Arctic region of this preindustrial simulation could be due to the addition of dust fields (Mahowald et al., 2006) and Fe and P cycles (Palastanga et al., 2011; Palastanga et al., 2013). Simulated ocean oxygen concentrations were comparable to Maier-Reimer (1993) and the WOA2013 (Figure 3-4 and Figure 3-5). POC, CaCO₃, and opal export and sediment composition are comparable to Maier-Reimer (1993). However, the model does trend toward higher export of CaCO₃ globally and slightly higher POC and opal export in the tropical latitudes compared to the empirical algorithm used by Sarmiento and Gruber (2006) (Figure 3-6). This bias may be linked to overestimation of export production linked to nutrient trapping (Najjar et al., 1992) at the equator. Sarmiento and Gruber (2006) used the chlorophyll concentration and sea surface temperature based empirical algorithm of Dunne et al. (2005) to determine POC export. CaCO₃ export and opal export were calculated from the estimated CaCO₃:POC and opal:POC export ratios.

The sediment composition in percent weight of POC was similar to Sarmiento and Gruber (2006). However, the opal composition is over estimated in HAMOCC 2.0 compared to Sarmiento and Gruber (2006, Figure 3-7) for the equatorial east Pacific. The CaCO_3 accumulation at the sea floor was slightly underestimated in the equatorial Pacific. Sarmiento and Gruber (2006) sediment composition data are from Archer (1996) and Seiter (2004).

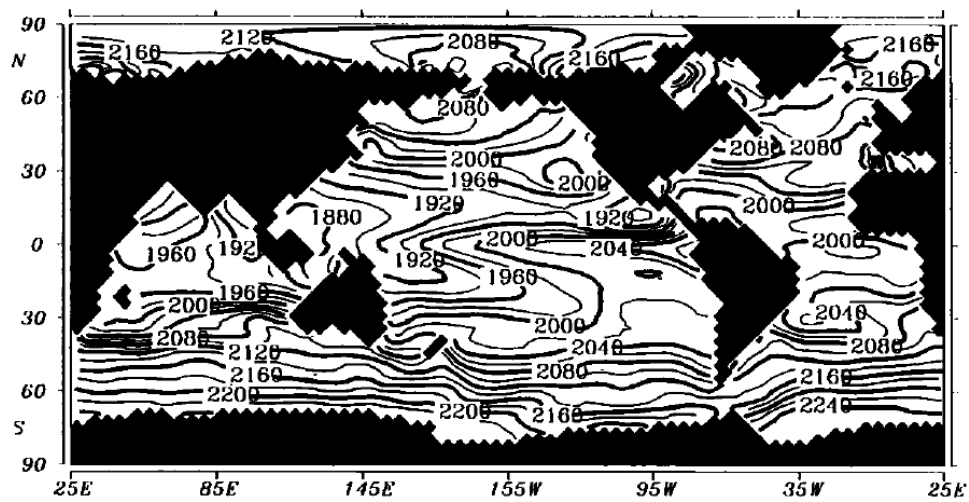


Figure 3-2 Surface DIC in $\mu\text{mol L}^{-1}$ simulated by HAMOCC 3.0 from Maier-Reimer (1993).

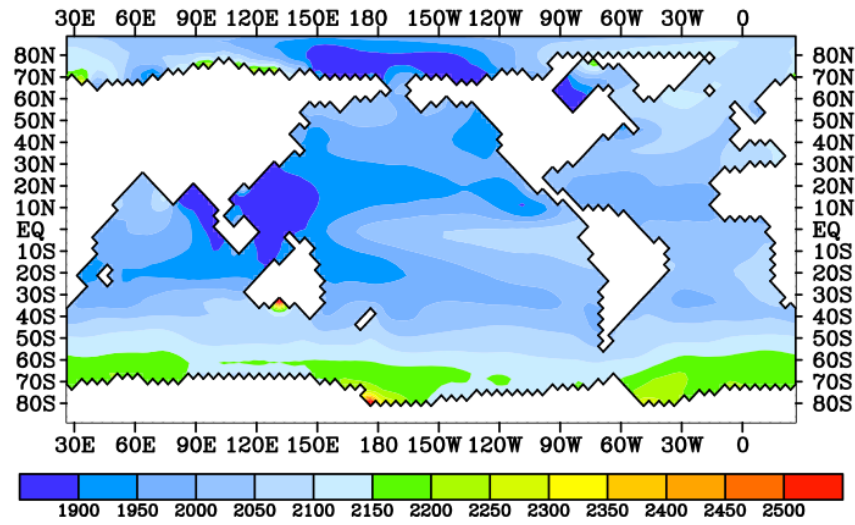


Figure 3-3 Surface DIC in $\mu\text{mol L}^{-1}$ simulated by preindustrial reference experiment of this study.

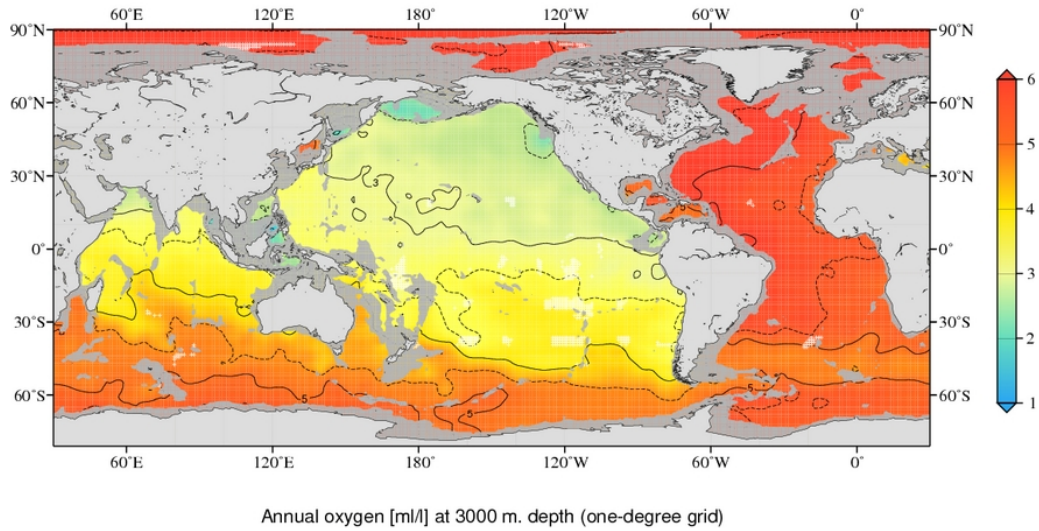


Figure 3-4 Dissolved oxygen concentration in ml L^{-1} at 3000 m depth from the World Ocean Atlas 2013. Note that $1 \text{ ml L}^{-1} \text{ O}_2$ is equal to $44.6 \mu\text{mol L}^{-1} \text{ O}_2$.

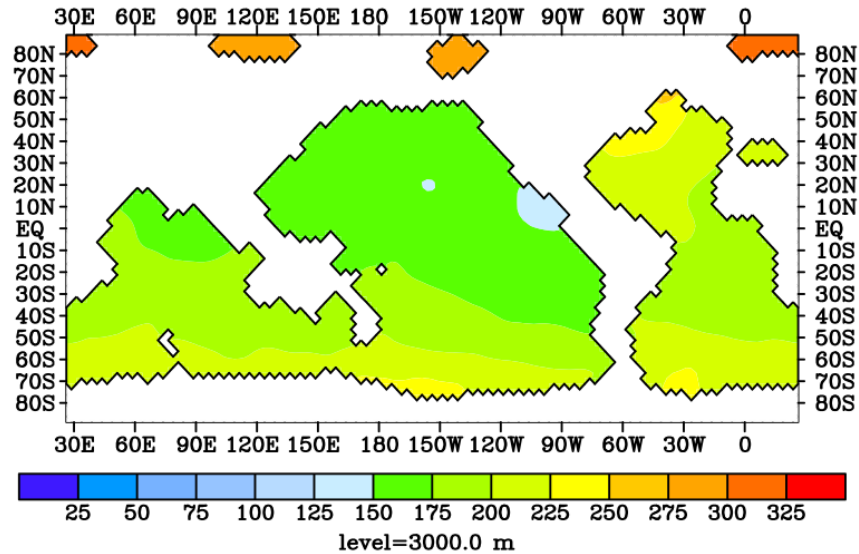


Figure 3-5 Dissolved oxygen concentration in $\mu\text{mol L}^{-1}$ at 3000 m depth from the preindustrial experiment of this study. Note that $1 \text{ ml L}^{-1} \text{ O}_2$ is equal to $44.6 \mu\text{mol L}^{-1} \text{ O}_2$.

In the following paragraphs the oxygen distribution of the reference simulation will be discussed. Simulated dissolved O_2 distribution did represent all five major non-seasonal oxygen minimum zones (OMZs; Chapter 1) of the Pacific Ocean and Indian Ocean and the OMZ or low oxygen zone (LOZ; dissolved $\text{O}_2 < 90 \mu\text{mol L}^{-1}$) of the eastern South Atlantic (Figure 3-8). However, due to the coarse model grid, the eastern Sub-tropical and tropical North Pacific OMZ as well as the OMZs in the Indian Ocean (Arabian Sea and Bay of Bengal) were not resolved. Therefore, this study simulated these as single OMZs (eastern North Pacific Ocean and Indian Ocean). The LOZ of the eastern South Atlantic was simulated in the reference experiment with a core of less than $20 \mu\text{mol L}^{-1} \text{ O}_2$ ($\sim 17\text{-}19 \mu\text{mol L}^{-1}$) and therefore was considered a non-seasonal OMZ. Using the presented OMZ definition the LOZ of the north tropical Atlantic was not simulated as a permanent OMZ in the reference experiment.

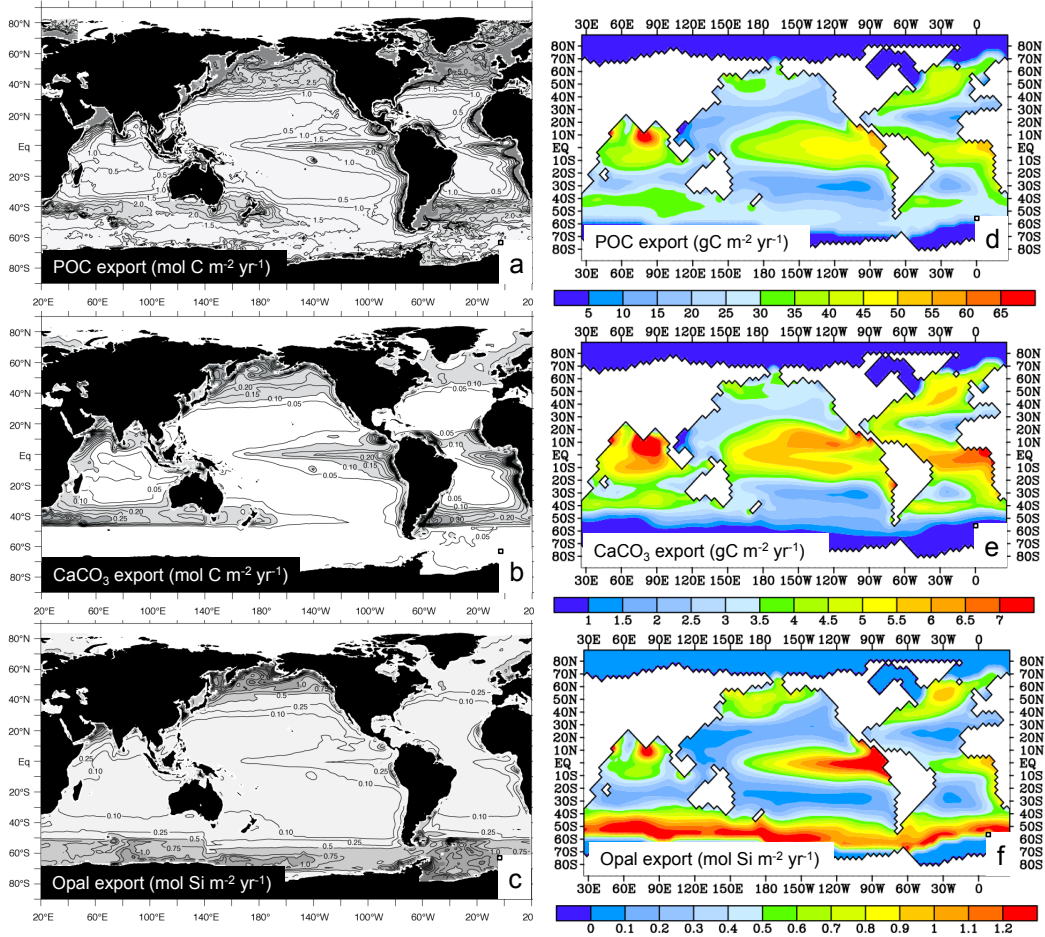


Figure 3-6 Export production of POC (a), CaCO_3 (b) and opal (c) from the euphotic zone (100m) Sarmiento and Gruber (2006) compared to the preindustrial reference experiment of HAMOCC 2.0 (d-f) at 25 m depth.

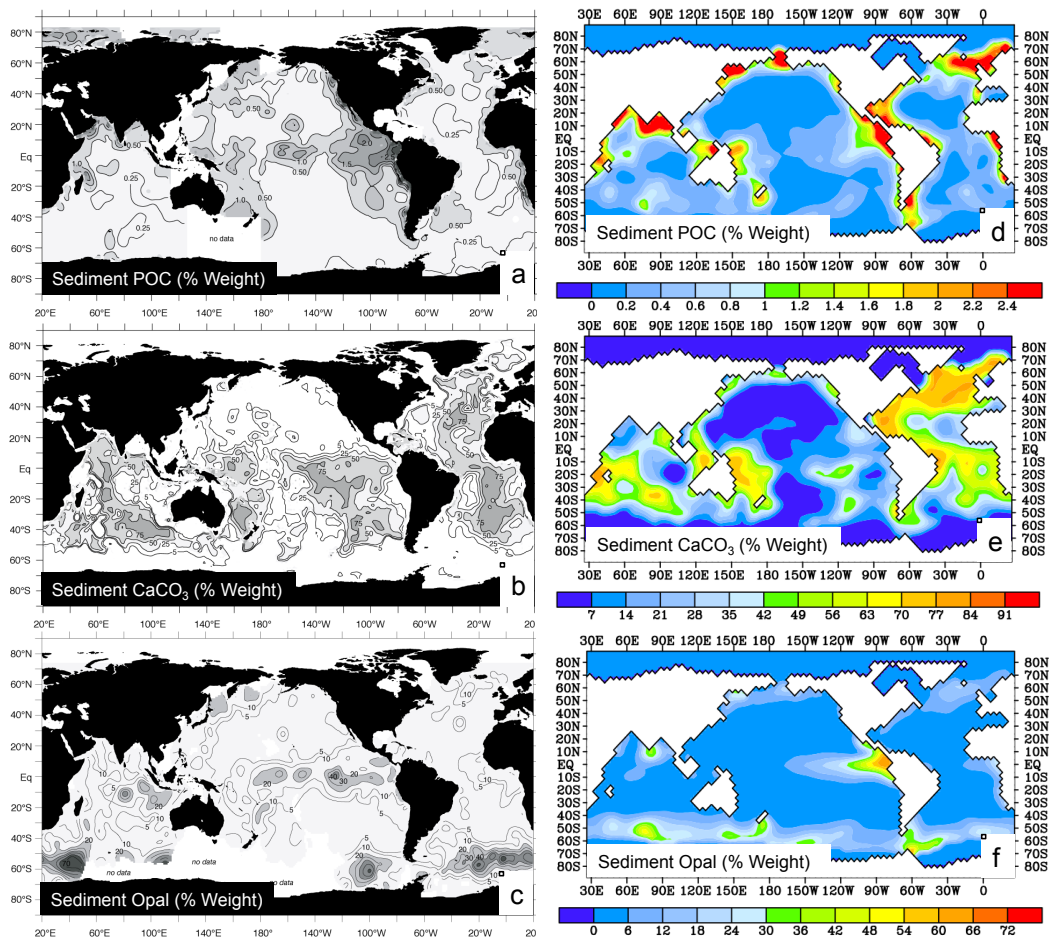


Figure 3-7 Sediment composition of POC (a), CaCO_3 (b) and opal (c) from Sarmiento and Gruber (2006) compared to the preindustrial reference experiment of HAMOCC 2.0 (d-f).

Present-day observed permanent OMZs are located between 37°S and 52°N (Kamykowski and Zentara, 1990; Helly and Levin, 2004; Fuenzalida et al., 2009; Paulmier et al., 2011). The tropical Pacific OMZ is the most extensive extending from the coast to approximately 180°E with a maximum depth of 3000 meters (Kamykowski and Zentara, 1990; Karstensen et al., 2008; Paulmier et al., 2011). The Arabian Sea and Bay of Bengal are the shallowest with an upper OMZ boundary ($\leq 50 \mu\text{mol O}_2 \text{ L}^{-1}$) between 44-96 meters (Paulmier et al., 2011). The tropical South Atlantic OMZ extends from approximately 5°S to 20°S with a western boundary of $70 \mu\text{mol L}^{-1}$ near 10°W and a depth of hypoxia of 300-500 meters (Karstensen et al., 2008). Paulmier and Ruiz-Pino (2011) estimate the total ocean area $\leq 20 \mu\text{mol L}^{-1}$ to be approximately 8% of the total oceanic area.

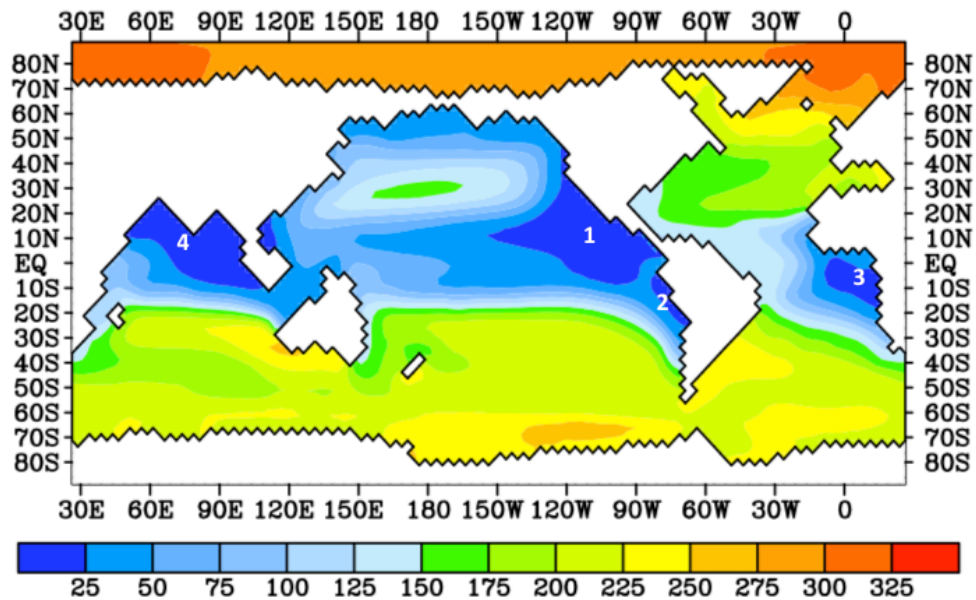


Figure 3-8 Locations of the OMZ at 450 meters depth simulated by HAMOCC 2.0 (reference experiment) [1] Eastern North Pacific OMZ [2] Eastern South Pacific OMZ [3] Eastern South Atlantic OMZ [4] Indian Ocean.

The model accurately represented the extent, depth, and core concentration values of the observed OMZ with the exception of the extension of the North Pacific OMZ past 180°E to approximately 150°E and a maximum depth of approximately 2300m in the reference experiment. The difference in horizontal extent between the model simulation and observed in the Eastern North Pacific OMZ was likely due to the annually averaged version of the model and therefore the lack of seasonally variability that occurs in OMZs. The total simulated oceanic area $\leq 20 \mu\text{mol L}^{-1}$ was approximately 8.6% including the South Sub-tropical Atlantic OMZ. The simulated vertical dissolved oxygen concentration placed the OMZ cores between 300 and 700 meters in depth (slightly shallower in the Indian Ocean OMZ). The approximate locations of the simulated cores are shown in Figure 3-9 and the simulated vertical profiles through the OMZ cores are shown in Figure 3-5.

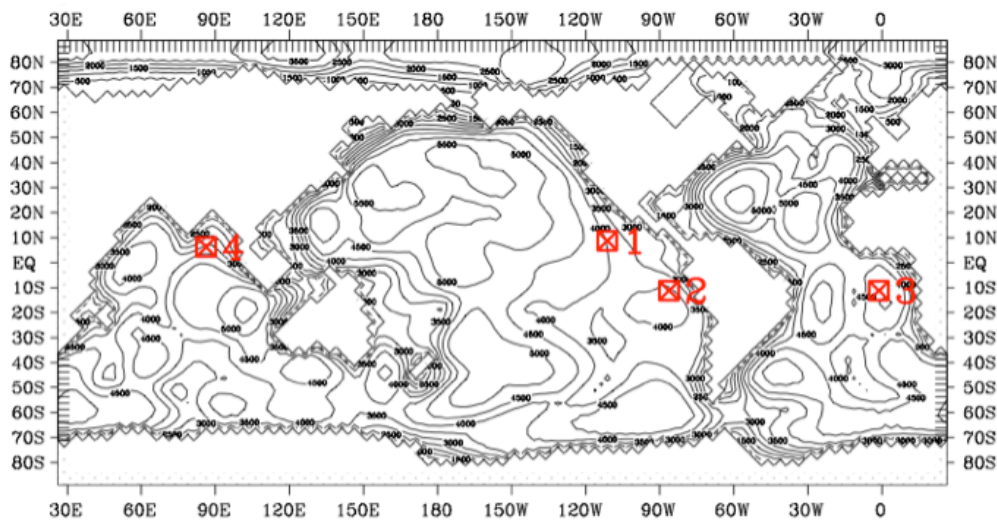


Figure 3-9 Simulated core locations of present day permanent non-seasonal OMZ. [1] eastern tropical North Pacific; 110°W, 10°N. [2] eastern tropical South Pacific; 85°W, 10°S. [3] eastern tropical South Atlantic; 5°W, 10°S. [4] Indian Ocean (Gulf of Bengal); 85°E, 7°N.

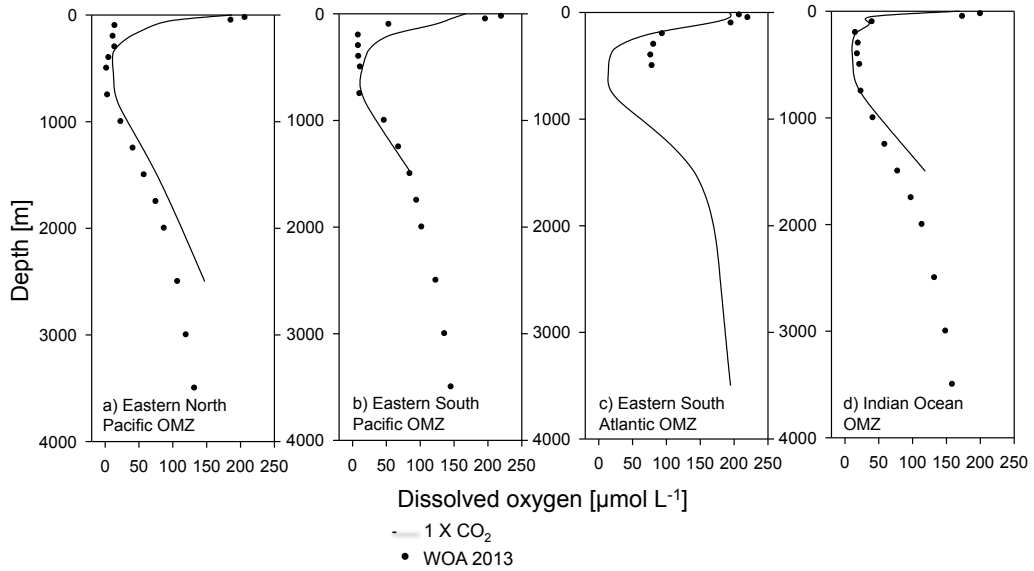


Figure 3-10 Simulated vertical dissolved O_2 concentrations through the OMZ cores for a) eastern North Pacific OMZ [$10^\circ N$, $110^\circ W$], b) eastern South Pacific OMZ [$10^\circ S$, $85^\circ W$], c) eastern South Atlantic [$10^\circ S$, $5^\circ W$], and d) Indian Ocean OMZ [$7^\circ N$, $85^\circ E$]. Observations are the annual statistical mean for dissolved oxygen from the World Ocean Atlas 2013 (Garcia et al., 2014). Standard error of the mean; upper ocean: $0.54\text{--}2.86 \mu\text{mol L}^{-1}$, twilight zone: $0.42\text{--}2.32 \mu\text{mol L}^{-1}$, deep ocean: $0.36\text{--}1.98 \mu\text{mol L}^{-1}$.

Chapter 4

Response of Export Production and Dissolved Oxygen Concentrations to pCO₂ and Temperature Stabilization Scenarios

4.1 Introduction

Oceanic uptake of the increased anthropogenic carbon emissions (LeQuéré et al., 2013) since the industrial revolution will have long-term effects and on the dissolved oxygen distribution within the ocean. The dissolved oxygen distribution will be altered due to ocean warming and the subsequent decline in solubility as well as variations in the biological pump due to changes in mixing and enhanced ocean stratification. This study focused on the extent and physical properties of oxygen minimum zones (OMZ, see Chapter 3) expansion as well as the formation of new OMZs under future emission scenarios including the mechanisms that lead to OMZ intensification.

There are five major non-seasonal OMZs discussed in the current literature, which are the eastern sub-tropical North Pacific OMZ (15°-25°N), the eastern tropical Pacific OMZ (equatorial region), the eastern South Pacific OMZ (15°-40°S), the Arabian Sea, and the Bay of Bengal (Kamykowski and Zentara, 1990; Karstensen et al., 2008; Paulmier et al., 2011). There is limited literature discussing the seasonal variability of the Atlantic and Indian Ocean OMZs; however, Pacific OMZs have been discussed extensively and there is strong evidence that expansion is already occurring (Stramma et al., 2008; Keeling et al., 2010; Stramma et al., 2012). Expansion of the OMZs, shoaling of the depth of hypoxia (DOH; shallowest depth at which OMZ criteria is met), and any shoaling of the OMZ cores into the photic zone could have severe impacts most notably the decline in ecosystems in the ocean. The low oxygen zone (LOZ; see Chapter 3) of the eastern tropical South Atlantic was simulated in the reference experiment with a core

of less than $20 \mu\text{mol L}^{-1}$ (approximately $17\text{-}19 \mu\text{mol L}^{-1}$) and therefore was considered a non-seasonal OMZ.

4.2 Experimental design

Carbon cycle sensitivity experiments were conducted in two sets of scenarios. The first set of scenario consists of a perturbation of the atmospheric CO_2 concentration relative to preindustrial atmospheric levels ($p\text{CO}_{2ref}$; PAL) of 2 X CO_2 , 3 X CO_2 , 4 X CO_2 , CO_2 , 6 X CO_2 , and 8 X CO_2 to explore the sensitivity of distribution of dissolved oxygen concentration to rising atmospheric $p\text{CO}_2$ level. In these simulations, all other boundary conditions and model parameters are kept at preindustrial levels (Table 3-2; Table 3-3). In a second set of experiments the $p\text{CO}_2$ levels were accompanied by the associated changes of the sea surface as well as deep-sea temperature to investigate the response of the dissolved oxygen distribution to increase in CO_2 radiative forcing.

In the CO_2 perturbation scenarios atmospheric $p\text{CO}_2$ was increased from preindustrial levels by 1% each year (t) until the perturbed atmospheric $p\text{CO}_2$ ($p\text{CO}_{2pert}$) is stabilized at its maximum level ($p\text{CO}_{2max}$) (Figure 4-1):

$$\begin{aligned} & \text{for } p\text{CO}_2 < p\text{CO}_{2max}: p\text{CO}_{2pert} = p\text{CO}_{2ref}(1 + 0.01)^t \\ & \text{and for } p\text{CO}_2 \geq p\text{CO}_{2max}: p\text{CO}_{2pert} = p\text{CO}_{2max} \end{aligned}$$

Equation 4-1

The 1% increase of atmospheric CO_2 concentration follows the IPCC (2013) business as usual scenario and was stabilized after 70 years for doubling (see also Winguth et al., 2005). The second set of carbon perturbation scenarios included the feedback of increasing seawater temperature due to rising atmospheric $p\text{CO}_2$ (Figure 4-1).

Temperature increased as a function of the 1% increase per time step of atmospheric

pCO₂ and was determined using the equation of Hansen et al., (1988) for the radiative forcing of CO₂ with the addition of a climate model sensitivity of A_t= 0.6870.

$$\Delta T = A_t 6.3 \ln \left(\frac{pCO_2}{pCO_{2ref}} \right)$$

Equation 4-2

Thus a doubling of pCO₂ in Equation 4-2 resulted in an increase in temperature of ~3°C which is consistent to the estimate of (Hansen et al., 1988; Archer, 2005). Note that this enhanced sensitivity include climate feedbacks whereas the direct CO₂ warming for 2 X CO₂ is ~1.2°C (Ruddiman, 2001; Houghton, 2004).

The resultant sea surface temperature change for the doubling of pCO₂ for 2 X CO₂, 4 X CO₂, 6 X CO₂, and 8 X CO₂ is 2.8°C, 5.9°C, 8.7°C and 11.5°C respectively (Figure 4-1). Solubility and chemical kinetic equilibrium constants of the carbon cycle are adjusted to the changes in pCO₂ and temperature at each time step in the temperature feedback experiments. In addition to experiments with increased pCO₂ with and without radiative forcing (Table 2-1) a reduced biology scenario was added in which primary productivity and export (Si, CaCO₃, and organic carbon) was set to zero following the approach of Maier-Reimer et al.,(1996). The reduced biology scenario was simulated with preindustrial pCO₂ (279 ppmv).

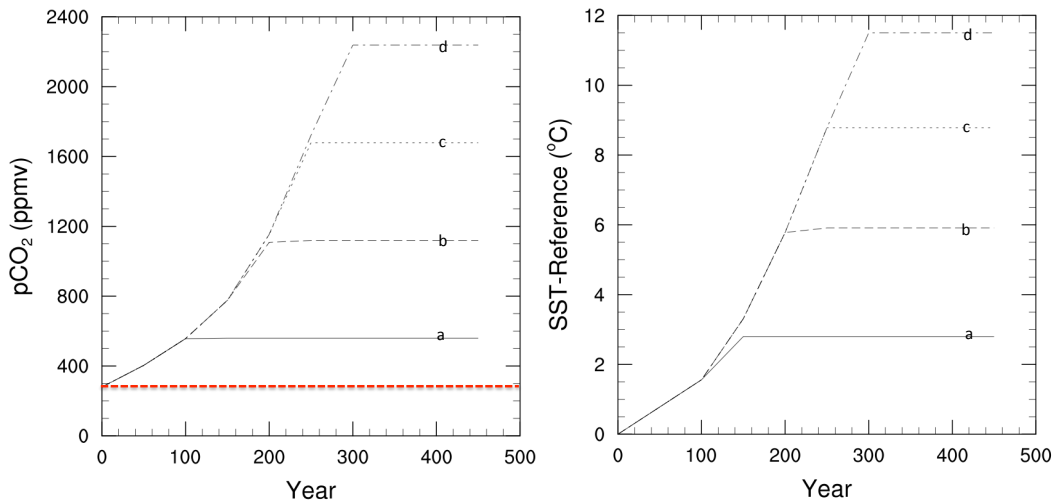


Figure 4-1 pCO₂ and SST increase from the reference run (a) 2 X CO₂ (b) 4 X CO₂ (c) 6 X CO₂ (d) 8 X CO₂ for the first 500 years of a 30k year simulation. The red dashed line indicates the preindustrial pCO₂ level.

4.3 Results

4.3.1 Sensitivity of the dissolved oxygen distribution to reduced biological pump and atmospheric pO₂

4.3.1.1 Sensitivity of dissolved oxygen to reduced biological pump

In order to explore the importance of biological pump (soft tissue pump) to the distribution and concentration of dissolved oxygen globally in the ocean all productivity was reduced to zero. This simulation, referred hereafter as the reduced biology scenario, is similar to the “Kill Biology” experiment by Maier-Reimer et al., (1996). In this simulation the atmospheric pCO₂ was set to preindustrial levels, which is in contrast to the experiment of Maier-Reimer et al., (1996) with an exponential increase in atmospheric pCO₂. Due to the reduced export production, the DIC concentrations increased at the ocean surface by >400 μmol kg⁻¹ and by >200 μmol kg⁻¹ in the intermediate and deep-water masses at mid-latitudes and led to a significant rise in total alkalinity by an average

of 550 ueq kg^{-1} . As a result, the pH increases by an average of 0.7 units (Figure 4-2) despite the loss of calcification and CaCO_3 burial. Note that weathering rates are kept at preindustrial conditions in all simulations. Dissolved oxygen increased by $>300 \text{ } \mu\text{mol L}^{-1}$ in the deep-sea and $>200 \text{ } \mu\text{mol L}^{-1}$ in the intermediate water masses. The dissolved oxygen gradient in this reduced biology scenario was controlled by the air-sea gas exchange of O_2 at the surface (Equation 3-2) and the temperature-dependent solubility of oxygen and not by the vertical POC flux, which was set by definition to zero to the “killed” productivity. Thus consumption of oxygen by decay of POC is also diminished.

4.3.1.2 Sensitivity of dissolved oxygen to reduced atmospheric $p\text{O}_2$

In an additional experiment, the sensitivity of deep-sea dissolved oxygen concentration to changes in atmospheric O_2 concentration was explored by reducing the atmospheric $p\text{O}_2$ by 50%. The decrease in atmospheric $p\text{O}_2$ did not alter the dissolved oxygen concentration in all depths significantly compared to the reference experiment (Figure 4-4).

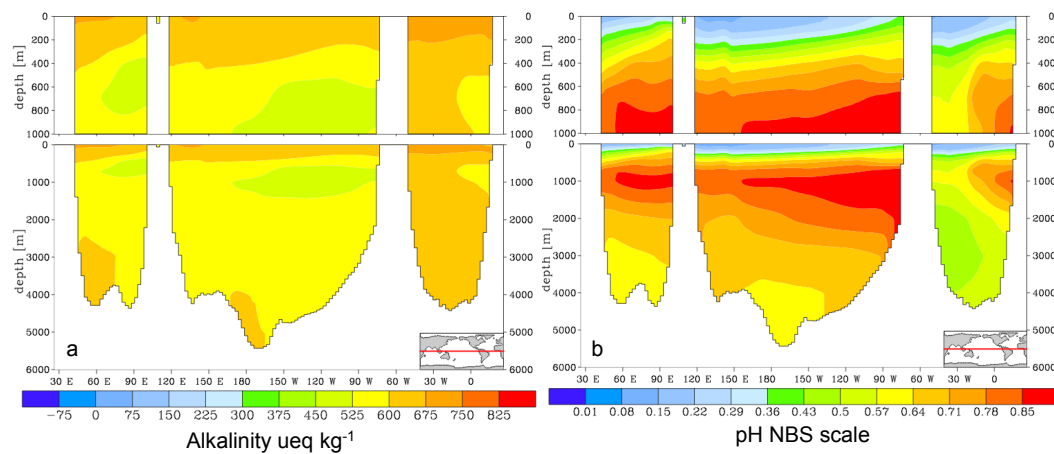


Figure 4-2 (a) Change in alkalinity from the reference experiment and (b) change in pH from the reference run for the extinction simulation.

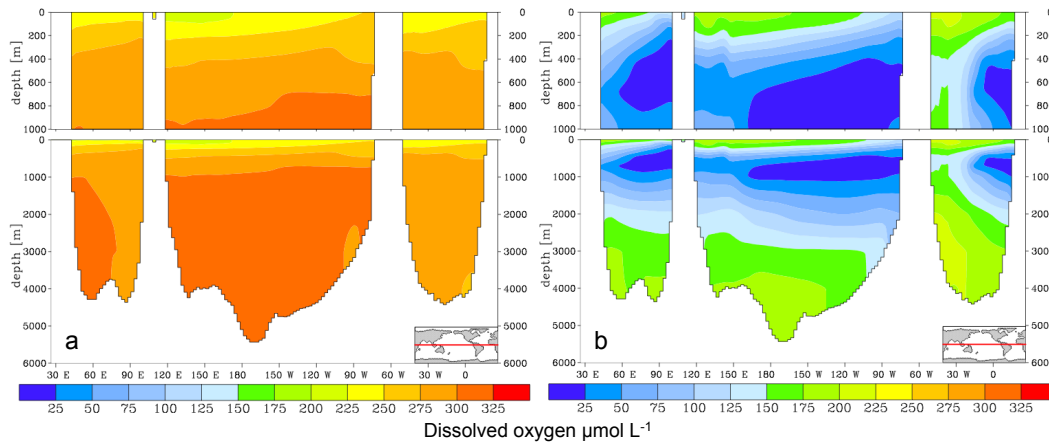


Figure 4-3 (a) Dissolved oxygen concentration for the extinction simulations and (b) reference simulation oxygen concentration.

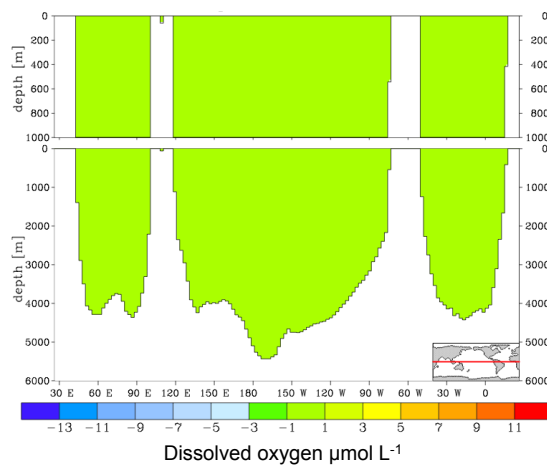


Figure 4-4 Change in dissolved oxygen concentration between the extinction simulation and the extinction simulation with a 50% reduction of atmospheric O_2 .

4.3.2 Sensitivity of the oxygen minimum zone to CO_2 radiative forcing

In each of the scenarios described above, the simulated OMZs expanded. The results included the formation of a new OMZ core in the south tropical western Pacific Ocean. There were significant changes in the distributions of dissolved oxygen concentrations in all simulations that include CO_2 radiative forcing. However, there were

only slight changes in the distributions of dissolved oxygen concentration for the simulations, which do not include CO₂ radiative forcing (Figure 4-5). Therefore, the following section will address the expansion of each OMZ and OMZ core as well as the global change at 2 X, 4 X, 6 X, and 8 X CO₂ simulations that included the temperature feedback.

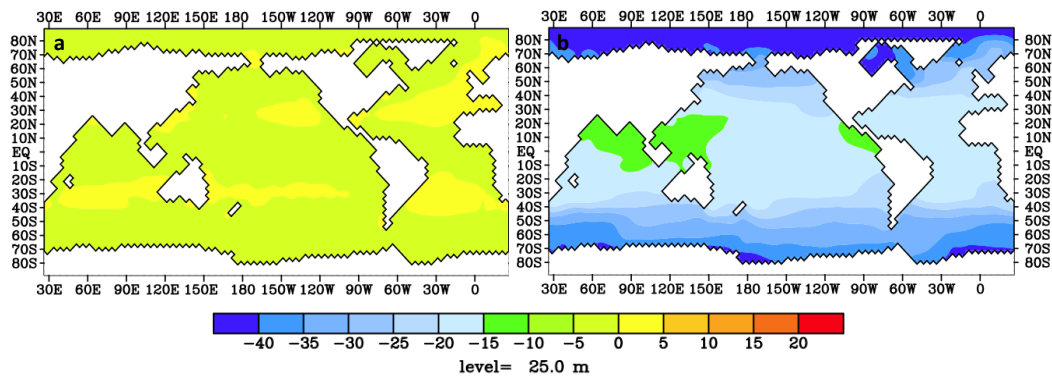


Figure 4-5 Dissolved O₂ concentration simulated by (a) the 4 X CO₂ experiment without CO₂ radiative forcing minus the reference experiment (b) the 4 X CO₂ with CO₂ radiative forcing simulation minus reference experiment.

4.3.2.1 Simulated OMZ expansion in the eastern tropical Pacific Ocean in response to CO₂ radiative forcing.

For the 2 X CO₂ experiment, the OMZ cores (dissolved O₂ concentration $\leq 20 \mu\text{mol L}^{-1}$) of the eastern North Pacific OMZ and the eastern South Pacific OMZ merge at the equator and therefore were considered a single OMZ, hereafter referred to as the eastern Pacific OMZ. At the west coast of North America, the northern extent of the eastern Pacific OMZ for the 2 X CO₂ experiment expanded from 35°N to 65°N. At a depth of 450 m it extended northward around the northern boundary of the North Pacific gyre with dissolved oxygen concentrations of $\leq 20 \mu\text{mol O}_2 \text{ L}^{-1}$ in the Gulf of Alaska. The southern boundary of the Pacific OMZ is located near the coast of Northern Chile at

approximately 30°S at 450 meters depth. Compared to the reference simulation, the OMZ in the 2 X CO₂ experiment expanded 200 km further to the south. The OMZ western boundary increased by approximately 550 km to 150°E. The depth of hypoxia (DOH) was between 150-250 meters. The OMZ had a max depth of 1900 meters, 200 meters deeper than the reference simulation. The OMZ core shoaled to 380 meters; however, it did not deepen in the 2 X CO₂ simulation. The lowest oxygen concentration in the OMZ core was 17 μmol O₂ L⁻¹ in this simulation.

The horizontal extent of the OMZ in the 4 X CO₂ scenario was similar to the 2 X CO₂ experiment with the addition of all of the North Pacific outside of the North Pacific Gyre having an dissolved oxygen concentration of ≤50 μmol L⁻¹ at a depth of 450 meters. The depth of hypoxia shoaled vertically to between 75-150 m from the surface in the North Pacific and remained in a depth range of 150-250m in the South Pacific (Figure 4-6). The maximum depth of the Pacific OMZ increased to 2000 m. For the 4 X CO₂ experiment, the OMZ core extended ~100 km west and deepened by 200 m compared to the 2 X CO₂ simulations. The depth of the OMZ core did not change in the 4 X CO₂ simulations compared to the 2 X CO₂ simulations but the minimum dissolved oxygen concentration decreased by 14 μmol L⁻¹ (Figure 4-7).

There is further extension of the OMZ core south to approximately 50°S (central coast of Chile) at 450 m depth in the 8 X CO₂ scenario relative to the 4 X CO₂ experiment. The OMZ core, at a depth of ~2000 meters, did not shoal or deepen in the 6 X and 8 X CO₂ compared to the 4 X CO₂ experiment. In the 8 X CO₂ simulation, the core became hypoxic with a minimum dissolved oxygen concentration of ≤8 μmol L⁻¹ (Figure 4-7). The 6 X CO₂ experiment resulted in a minimum dissolved oxygen concentration of ~12 μmol L⁻¹.

4.3.2.2 Simulated OMZ expansion in the eastern tropical South Atlantic in response to CO₂ radiative forcing.

The horizontal expansion of the OMZ in the eastern South Atlantic in the 2 X CO₂ simulation remained similar to the reference scenario with a southern boundary at approximately 25°S and extending northward along the west coast of Africa to the southern tip of Morocco to approximately 15°N. The depth of hypoxia shoaled from between 250-450 m in the reference experiment to 150-250 m. The maximum depth of OMZ increased by 100 m to 1200 m. In the eastern South Atlantic, the OMZ core in the 2 X CO₂ experiment expanded relative to the reference experiment 580 km to approximately 19°S and northward by 110 km (~1° northward propagation). In this 2 X CO₂ experiment, the OMZ core expanded vertically; it shoaled to 450 m and deepened to 915 m, which is 65 m deeper than the reference simulation. The minimum dissolved O₂ concentration was reduced by 1 μmol L⁻¹ relative to the reference experiment to 17 μmol O₂ L⁻¹.

For the 4 X CO₂ simulation there was insignificant horizontal expansion in the latitudinal direction (Figure 4-6) relative to the reference experiment. The most notable area of expansion was in the southwest direction in which the southwestern boundary of the eastern South Atlantic OMZ extend to ~30°S and ~20°W. The maximum depth increased by an additional 100 m to a depth of 1300 m. The OMZ core expanded symmetrically, by about 100 km, encompassing the Gulf of Guinea. The vertical expansion of the core was negligible between the 2 X and 4 X CO₂ simulations; however, the strength of the core increased significantly with a minimum dissolved O₂ concentration of 12 μmol L⁻¹ (Figure 4-7).

Horizontal expansion of the eastern South Atlantic OMZ did not occur between the 4 X CO₂ simulation and the 6 X or 8 X CO₂ scenarios. In the 6 X CO₂ scenario the

horizontal extent of the eastern South Atlantic at 450 m depth is reduced from the 4 X CO₂ simulation, where as in the 8 X CO₂ simulation the horizontal area expands back to the extent of the 4 X CO₂ simulation. The depth of hypoxia remained between 150-250 m depth for both 6 X and 8 X CO₂ experiments. The maximum depth of the OMZ increased to 1500 m in the 8 X CO₂ simulation. The OMZ core deepened to 1050 m and shoaled from the 4 X and 8 X CO₂ scenarios to 375 m. The minimum dissolved O₂ concentration remained at 12 μmol L⁻¹ for both the 6 X and 8 X CO₂ simulations (Figure 4-7).

4.3.2.3 Simulated expansion of the OMZ in the tropical Indian Ocean in response to CO₂ radiative forcing.

The expansion of the OMZ in the Indian Ocean is limited at the western boundary by the east coast of Africa and the eastern boundary is constrained by the Indonesian archipelago. The Indian Ocean OMZ included the poorly resolved Arabian Sea and the Gulf of Bengal, which is limited by the Indian subcontinent. Compared to the reference simulation, the OMZ extended southward to 10°S in the 2 X CO₂ simulation and deepened by 100 m to 1100 m. The OMZ core did not expand horizontally but deepened to 900 meters and shoaled by 50m to 225 meters. The minimum dissolved oxygen concentration was 10 μmol L⁻¹ (Figure 4-7) and remained the lowest concentration for each of the emissions scenario.

In the 4 X, 6 X, and 8 X pCO₂ simulations the horizontal expansion in the Indian Ocean OMZ was insignificant but it deepened to 1300 m, 1400 m, 1700 m, for the 4 X, 6X, and 8 X CO₂ simulations, respectively (Figure 4-6). For the 4 X CO₂ experiment the OMZ core expanded in the western direction to 45°E and deepened by 100 m to 1000 m; however, the upper boundary of the OMZ remained unchanged. In the 8 X CO₂ simulation the core expanded southward by 650 km to approximately 16°S and shoaled to 100 m for both the 6 X and 8 X CO₂ scenarios; however, the lower boundary remained

unchanged compared to the 4 X CO₂ experiment. The depth of hypoxia was located between 25 m and 75 m in the reference experiment and in all CO₂ emission scenarios.

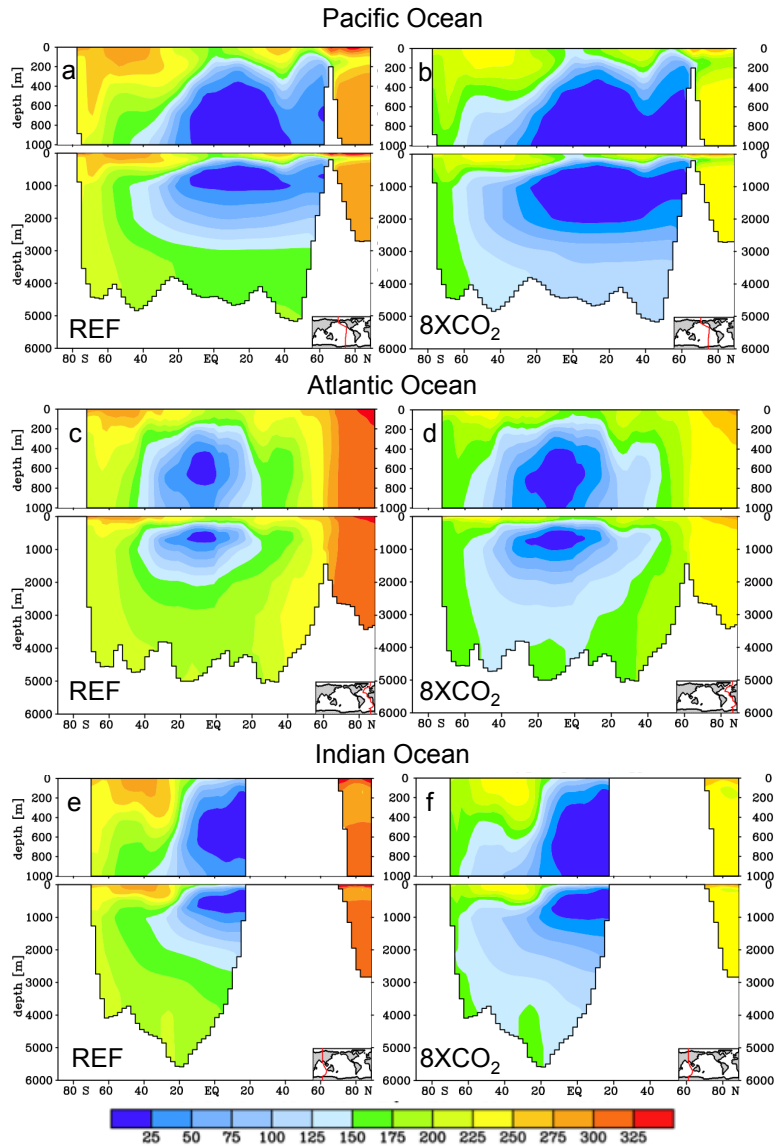


Figure 4-6 Meridional cross-section of dissolved oxygen [$\mu\text{mol L}^{-1}$] in the Pacific OMZ for the (a) reference experiment and (b) 8 X CO₂ experiment, the Atlantic OMZ for the (c) reference experiment and (d) 8 X CO₂ experiment, and the Indian Ocean for the (e) reference experiment and (f) 8 X CO₂ experiment.

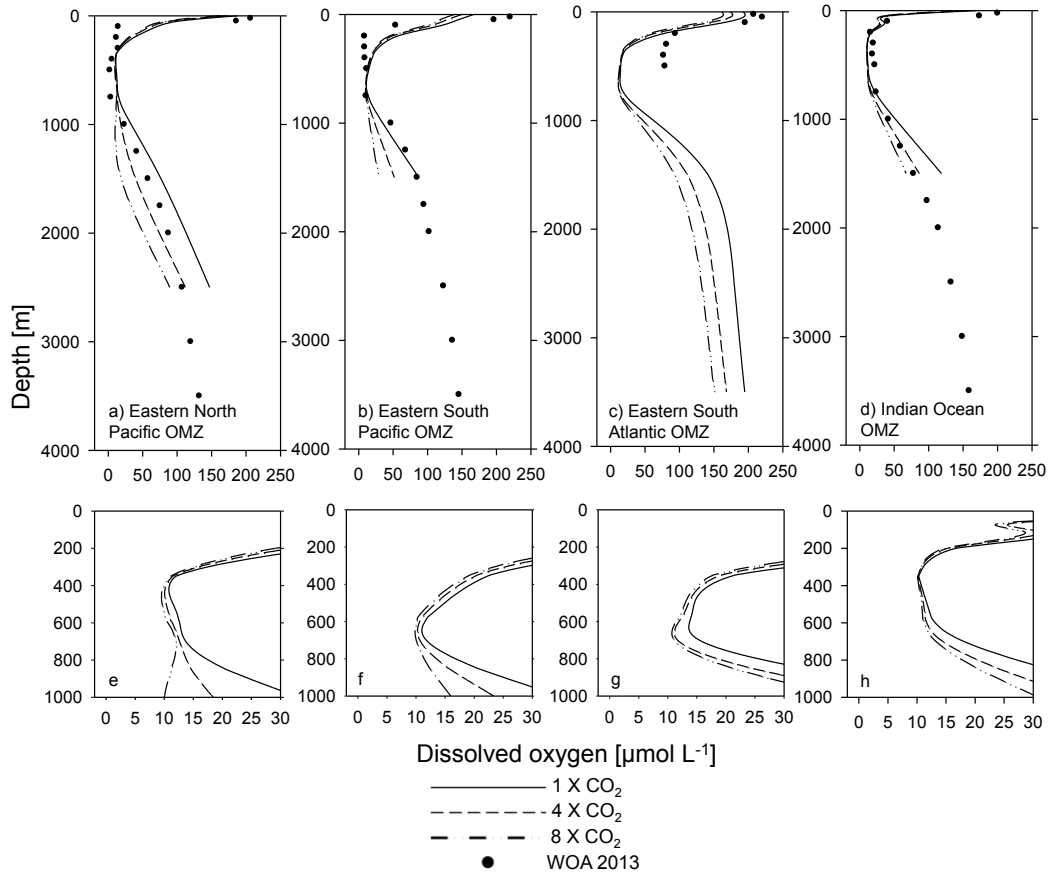


Figure 4-7 Simulated vertical distribution of dissolved O_2 through the OMZ cores for a) Eastern North Pacific OMZ, b) Eastern South Pacific OMZ, c) Eastern South Atlantic OMZ, and d) Indian Ocean OMZ for the 1 X, 4 X and 8 X CO_2 simulations (top). The bottom row are finer scale dissolved oxygen profiles for the OMZ cores e) Eastern North Pacific OMZ, f) Eastern South Pacific OMZ, g) Eastern South Atlantic OMZ, and h) Indian Ocean OMZ for the 1 X, 4 X and 8 X CO_2 simulations. Observations are the annual statistical mean for dissolved oxygen from the World Ocean Atlas, 2013 (Garcia et al., 2014). Standard error of the mean; upper ocean: $0.54\text{-}2.86 \mu\text{mol L}^{-1}$, twilight zone: $0.42\text{-}2.32 \mu\text{mol L}^{-1}$, deep ocean: $0.36\text{-}1.98 \mu\text{mol L}^{-1}$.

4.3.2.4 Simulated OMZ formation in the western tropical Pacific Ocean in response to CO₂ radiative forcing.

An OMZ core (<20 μmol L⁻¹ O₂) was simulated in the western tropical Pacific Ocean (143E, 2N) near the Bismark Sea after 5000 years integration of the 3 X CO₂ simulation. This region was modeled as a low oxygen zone (LOZ) in the reference simulation. For the 4 X CO₂ experiment, the OMZ developed in <2000 yr integration with a minimum dissolved oxygen concentration of 17 μmol L⁻¹. The upper boundary of the OMZ core remained unchanged for all perturbation simulations compared to the reference. However, the OMZ core deepened from 725 meters at 3 X CO₂ to 1000 meters for the 8 X CO₂ simulation.

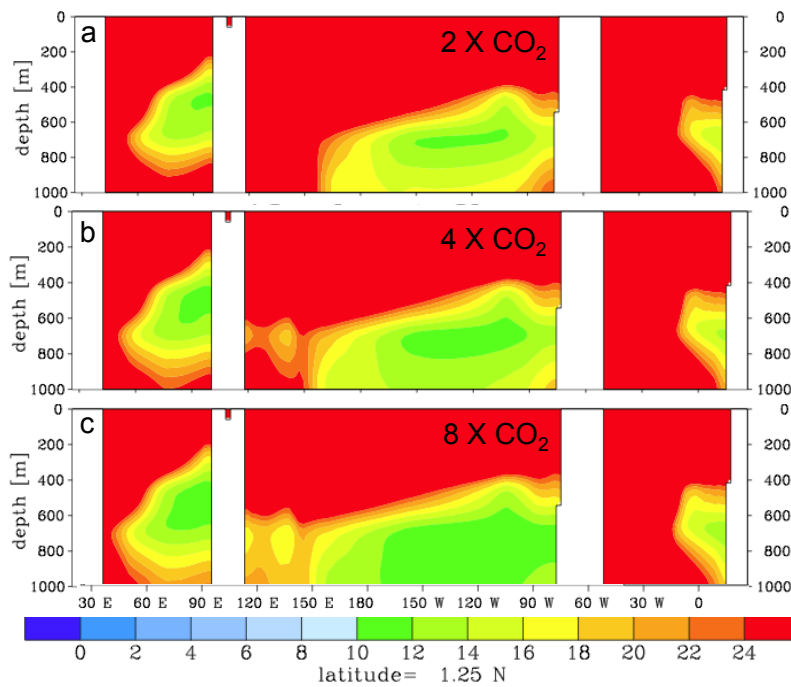


Figure 4-8 Zonal cross-section at 1.25° N of the formation of the western tropical Pacific OMZ for the (a) 2 X, (b) 4 X and (c) 8 X CO₂ simulations. The OMZ core is located between 130°E and 150°E.

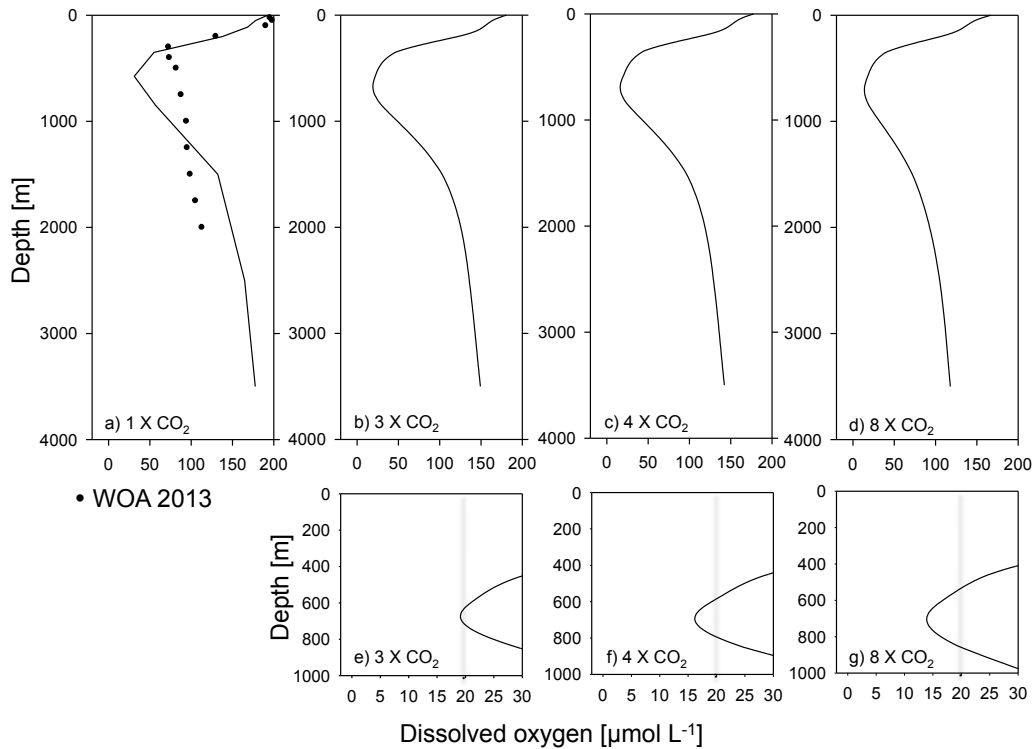


Figure 4-9 Simulated vertical dissolved oxygen concentration through the western tropical Pacific OMZ for the a) 1 X CO₂, b) 3 X CO₂, c) 4 X CO₂, and d) 8 X CO₂ simulations (Top). The bottom row are finer scale dissolved oxygen profiles for the OMZ cores e) 3 X CO₂, f) 4 X CO₂, and g) 8 X CO₂ simulations. The black dashed lines indicate the 20 μmol O₂ L⁻¹ threshold for OMZ core. For comparison the annual statistical mean for dissolved oxygen from the World Ocean Atlas, 2013 (•) (Garcia et al., 2014) is displayed. Standard error of the mean for the WOA2013; upper ocean: 0.54-2.86 μmol L⁻¹, twilight zone: 0.42-2.32 μmol L⁻¹, deep ocean: 0.36-1.98 μmol L⁻¹.

4.3.2.5 Export of particulate organic carbon and changes in global dissolved O₂ concentration in response to CO₂ radiative forcing.

Total particulate organic carbon production and export production of particulate organic carbon (P_{POC}) (Equation 3-6) from the euphotic zone into the deep sea (hereafter referred to as export production) increased predominantly near the equatorial Pacific with a rise in seawater temperature in response to CO₂ radiative forcing (Table 4-1). P_{POC} in the northern Indian and western tropical Pacific decreased in response to enhanced CO₂ radiative forcing, where as, changes in the east Atlantic Ocean were insignificant.

Table 4-1 Global total particulate organic carbon production and export production of particulate organic carbon (P_{POC}) at 30k years.

Simulation	Change in SST from Reference [°C]	Total POC Production [PgC yr ⁻¹]	Change from Reference [%]
REF	0	10.53	
2 X CO ₂	2.8	10.69	1.52
4 X CO ₂	5.91	10.79	2.48
6 X CO ₂	8.78	10.81	2.67
8 X CO ₂	11.5	10.93	3.78

Simulation	Change in SST from Reference [°C]	P _{POC} [PgC yr ⁻¹]	Change from Reference [%]
REF	0	9.14	
2 X CO ₂	2.8	9.28	1.52
4 X CO ₂	5.91	9.38	2.59
6 X CO ₂	8.78	9.40	2.81
8 X CO ₂	11.5	9.41	2.98

Expansion of OMZs and LOZs occurred during the first 2000 years of integration in each 30k year carbon perturbation simulation. The expansion continued on average 1500 years beyond the year in which the peak pCO₂ emission value was reached. The greatest reduction in surface dissolved oxygen occurred in the eastern tropical Atlantic OMZ, as a result of CO₂ radiative forcing. The total ocean area with a dissolved oxygen concentration of <50 μmol L⁻¹ expanded at approximately 2% per ~3°C increase in

seawater temperature which corresponded to a doubling of $p\text{CO}_2$ (Table 4-2). A $\sim 3^\circ\text{C}$ increase in temperature resulted in a shoaling of the OMZ by ~ 40 m and deepening ~ 45 m in the Indian Ocean and eastern South Atlantic Ocean, whereas in the eastern tropical Pacific OMZ core shoaled by ~ 20 m and deepened by ~ 240 m. The total ocean area at which the dissolved O_2 concentration is $< 50 \mu\text{mol L}^{-1}$ increased by 7.5% in the 8 X CO_2 simulations. The increase of hypoxic area in the photic zone is insignificant ($< 0.3\%$) due to the air-sea gas exchange. However, an area of hypoxia formed in the photic zone of the Sub-tropical North Pacific Ocean with a dissolved O_2 concentration of less than $12 \mu\text{mol L}^{-1}$.

Table 4-2 Total ocean area and total ocean volume at which dissolved O₂ concentrations are ≤50 μmol L⁻¹, ≤20 μmol L⁻¹, and ≤12 μmol L⁻¹ respectively for the 2 X, 4 X, 6 X and 8 X CO₂ simulations. Total ocean area value is from Volumes of the World's Oceans from ETOPO1 (Eakins and Sharman, 2010).

Simulation	SST [°C]	Total Ocean Area [10 ⁴ km ²]	Total Ocean Area [%]	~Ocean Volume [10 ⁵ km ³]	~Ocean Volume [%]	Total Ocean Area in the Photic Zone [10 ⁴ km ²]	Total Ocean Area in the Photic Zone [%]
Dissolved Oxygen Concentration ≤ 50 μmol L ⁻¹							
REF	19.4	5898.9	16.3	766.8	5.7	155.6	0.43
2 X CO ₂	22.2	6803.7	18.8	1088.5	8.1	188.1	0.52
4 X CO ₂	25.31	7527.5	20.8	1430.2	10.7	206.2	0.57
6 X CO ₂	28.18	8070.3	22.3	1614.1	12.1	227.9	0.63
8 X CO ₂	30.9	9879.7	23.8	2173.5	16.2	242.4	0.67
Dissolved Oxygen Concentration ≤ 20 μmol L ⁻¹							
REF	19.4	3112.3	8.6	186.7	1.4	39.8	0.11
2 X CO ₂	22.2	3763.7	10.4	225.2	1.7	50.6	0.14
4 X CO ₂	25.31	4379.9	12.1	350.3	2.6	61.5	0.17
6 X CO ₂	28.18	4885.6	13.5	537.4	4.0	65.1	0.18
8 X CO ₂	30.9	5356.1	14.8	1071.2	8.0	65.1	0.18
Dissolved Oxygen Concentration ≤ 12 μmol L ⁻¹							
REF	19.4	365.5	1.01	6.3	0.4	0	0
2 X CO ₂	22.2	506.6	1.4	8.8	0.06	0	0
4 X CO ₂	25.31	987.9	2.7	34.5	0.25	0	0
6 X CO ₂	28.18	1049.5	2.9	57.7	0.43	2.5	0.007
8 X CO ₂	30.9	1447.6	4.0	115.8	0.86	2.5	0.007
Total Ocean		36190.0	100	13390.3	100		

4.4 Discussion

In this study we investigated the expansion of OMZ as a result of increased seawater temperature in response to CO₂ radiative forcing. It is important to note that changes in ocean stratification due to ocean temperature and density changes were not simulated and held constant at preindustrial conditions. Therefore, the expansions of OMZs in this study are the result of changes in O₂ solubility and temperature-dependent productivity (Equation 3-6) and therefore may be modest due to no consideration a weakened connection between the OMZ and the ocean surface in the future (Glessmer et al., 2011). It has been suggested that the depth and strength of the thermocline may influence OMZ expansion and contraction (Deutsch et al., 2007). An increase of the thermocline in a warmer climate may result in a contraction of the OMZs due to reduced oxidative demand in hypoxic waters. However, this study assumed a constant thermocline depth, as the temperature increase is uniform at all depths. Other assumptions in this study were a constant nutrient inventory (Fe fertilization is considered in Chapter 6) and Redfield ratio. Changes in the Redfield ratio due to climate change has been suggested as a possible mechanism of enhanced volume of suboxic water in the ocean due to the respiration of increased organic carbon (Oschlies et al., 2008). Measurements of dissolved oxygen concentration in the suboxic regions of the oceans are limited (Locarmini et al., 2006; Levitus et al., 2013); however, paleo-records and climate models support the assumption that ocean anoxic events occur during periods of high pCO₂ (Falkowski et al., 2011). Furthermore, OMZs have expanded and contracted during the glacial interglacial cycles (Galbraith et al., 2004) as well as on shorter time scales in response to Dansgaard-Oeschger (D-O) events (Cannariato and Kennett, 1999).

The simulations of this study agree with other studies of model-simulated change and observed change in the extent of OMZs (Whitney et al., 2007; Karstensen et al., 2008; Stramma et al., 2008; Shaffer et al., 2009; Falkowski et al., 2011). However, the simulations presented here have a greater overall decrease in global oxygen concentration of 9.1% after 300 years of integration for a doubling of pCO₂ than previous studies ranging from 1-7% for various pCO₂ emissions and integration times (Matear et al., 2000; Bopp et al., 2002; Oschlies et al., 2008; Schmittner et al., 2008; Bopp et al., 2013). The rapid decrease in global dissolved O₂ concentration was due to the rapid change in global ocean temperature linked to the 1% business as usual atmospheric CO₂ emissions and therefore resulted in large changes in dissolved oxygen at high latitudes. However, the dissolved oxygen concentrations in the OMZ areas decreased more slowly in the model simulations as compared to the observed trends from Stramma et al., (2008). Stramma et al., (2008) produced a linear trend for each basin between the depths of 300-700 m for temperature and oxygen. The study suggests that temperature has increase by 0.005 °C yr⁻¹ in the Atlantic and Indian Oceans and a temperature decrease by 0.005 C yr⁻¹ for the Pacific Ocean since the 1960s. The oxygen loss for each basin since 1960 was approximately 0.23, 0.16, 0.09 μmols O₂ kg⁻¹ yr⁻¹ for the Atlantic, Pacific, and Indian Ocean respectively. Most of the expansion of suboxic area occurred during the first 2000 years of the 30,000-year simulation due to the slow response time, particularly in the deep Pacific Ocean. Compared to the reference experiment, the atmospheric pCO₂ is stabilized at the elevated CO₂ concentrations in the carbon perturbation simulations in this study; therefore, there is no recovery and the expanse and global dissolved oxygen is adjusted after ~2000 years.

In all carbon perturbation simulations the upper boundary of the OMZ cores were shallower compared to the reference simulation. The shallowest OMZ core was found in

the Indian Ocean OMZ at ~75 meters. Note that the upper boundary of the OMZ was located at 75 m depth because above this depth water masses were influenced by the air sea gas exchange of the uppermost model layer (Figure 4-8, Figure 4-9, and Figure 4-10). The core was not expected to shallow beyond 50 m depth in the simulations due to the assumption that the ocean surface oxygen concentration is at equilibrium with the atmosphere and the simulated surface layer of the top 50 meters. The OMZ core of the North Pacific had the deepest upper boundary, shoaling approximately 100 meters for the highest pCO₂ carbon perturbation scenario. The slower shoaling of the OMZ in the tropical Pacific Ocean compared to that of the tropical eastern Atlantic and Indian Ocean OMZs may be related to difference in solubility as well as linked to a stronger upwelling in the tropical eastern Pacific Ocean. Downward expansion of the OMZ core is limited by the lower boundary of the activity-ventilated zone at approximately 2000 meters in the Pacific. This depth coincides with the depth of the wind-driven circulation, which remained unchanged in each simulation, because the same wind stress forcing is applied to all simulations. Deepening of the eastern South Atlantic OMZ and the Indian Ocean OMZ were limited to the bottom boundary of the well-ventilated mixed layer (~1500 meter for the Atlantic and ~1000 meters for the Arabian Sea). The ventilation depth of the Arabian Sea may be over estimated due to the lack of monsoon variation in the model, which can cause the mixed layer depth to vary greatly in the Arabian Sea.

The expansion of the OMZ in the Indian Ocean and eastern South Atlantic Ocean were controlled primarily by changes in temperature-dependent oxygen solubility and to a lesser extent to changes in the temperature-dependent export production of POC. The extent of the OMZ in the Indian Ocean appears to be insensitive to changes in the export of organic matter in response to radiative forcing of less than 6 times of the preindustrial pCO₂. Figure 4-11 displays the increased outgassing of oxygen at higher

pCO₂ levels throughout the tropical regions. The water masses of the present day Arabian Sea and Bay of Bengal are much lower in sea surface dissolved oxygen than either the tropical Atlantic or tropical Pacific OMZs and exhibited a shallower depth of hypoxia. Therefore, any further loss of solubility due to ocean warming would cause an intensification of the OMZ. Findings from this sensitivity study suggest that the expansion of the Indian Ocean OMZ is controlled by solubility changes rather than changes in the export production of POC. The extent of the OMZ in the eastern tropical South Atlantic intensifies mainly due to the change in solubility and exhibited the greatest change in sea surface dissolved oxygen concentration due to CO₂ forcing of all the OMZs simulated (Figure 4-5). There is an insignificant change in export production of POC in the eastern tropical South Atlantic OMZ. The extent of the present day OMZ has a much higher dissolved oxygen concentration due to cooler water masses than in the northern Indian Ocean. However, the higher salinity of the Atlantic lead to greater loss of O₂ solubility at higher sea surface temperatures as compared to the Indian Ocean or eastern tropical Pacific Ocean for each pCO₂ simulation.

The change in the extent of the OMZ in the Pacific Ocean was driven by the change in productivity and export production of POC and to a lesser degree by changes in temperature-dependent dissolved O₂ solubility (Figure 4-10; Figure 4-11). Loss of solubility was greater in the eastern South Atlantic; however, the increase of export production of POC in the eastern equatorial Pacific OMZ led to significant horizontal expansion, which was not simulated in the eastern South Atlantic. The model did not indicate a more significant increase in P_{POC} in the cold tongue of the Pacific Ocean as compared to the warm pool in the western Pacific Ocean. However, it is important to note the simulated CO₂-induced seawater temperature change was uniform and therefore the eastern Pacific seawater temperature remains cooler relative to other regions of the

Pacific Ocean. The Pacific OMZ did not shoal as significantly as the Indian Ocean or eastern South Atlantic OMZs but expanded horizontally under the area of high productivity. Oxygen loss due to remineralization of organic matter was potentially the main mechanism for expansion of the OMZ in the tropical Pacific Ocean. Figure 4-10 is a cross section of the amount of oxygen consumed by the remineralization of organic matter indicating the large influence of organic matter export in the eastern tropical Pacific OMZ as opposed to eastern South Atlantic OMZ.

In the carbon cycle perturbation simulations, the LOZ that currently exists in the western tropical Pacific met the criteria of a permanent non-seasonal OMZ for the 3 X CO₂ simulation; however, in <2000 yrs a much stronger OMZ core developed in the 4 X CO₂ simulation (Figure 4-8). The formation occurred northwest of the Gulf of Carpentaria and expanded into the Banda Sea and south along the west coast of Australia. The western tropical Pacific OMZ formed in the warm water masses of the Indonesian throughflow (ITF), which brings warm water westward from the Pacific into the Indian Ocean. The OMZ was then expanded by the oxygen-depleted water masses originating from the Leeuwin Current, which flows south around the west coast of Australia. The controlling mechanism of the formation of the new OMZ core was similar to that of the Indian Ocean OMZ expansion. There was a net loss of export of production of POC in the area suggesting the main control of OMZ core formation was loss of O₂ solubility due to increased SST in an area of high heat transport between the Pacific and Indian Oceans. The formation of an OMZ could be expected in this area of higher SST; however, it is important to note that the model did not include changes in the intense tidal induced mixing that may affect sea surface temperatures and dissolved oxygen concentrations within the Indonesian throughflow.

4.5 Conclusion and future research

Increased sea surface temperature as a result of CO₂ radiative forcing will likely cause expansion of present-day tropical OMZs as well as the possibility of the formation of new oxygen depleted regions. Understanding the extent and the mechanisms for these OMZ expansions is of the utmost importance in order to more accurately predict environmental changes in these regions. Simulated expansion of the oxygen minimum zone was greatest in the eastern tropical Pacific Ocean, which was more sensitivity to the change in export of particulate organic carbon and less sensitive to loss of surface oxygen solubility. Total production increased greatest in the equatorial Pacific leading to the rapid horizontal expansion of the OMZ core. The expansion of the OMZ in the eastern equatorial Pacific Ocean could be reduced due to decrease in the export production of POC. Moreover, a change in the ecosystem structure could alter the Redfield ratio. A rise in the seawater temperature and high salinity in the Atlantic surface water lead to the greatest loss of dissolved oxygen in the intermediate water masses of any of the OMZs simulated. This loss in solubility caused a greater shoaling and deepening in the eastern tropical South Atlantic OMZ rather than horizontal expansion. However, the OMZ did expand more symmetrically than the eastern tropical Pacific OMZ which expanded horizontally. The Indian Ocean OMZ was restricted in horizontal expansion; therefore, simulated changes in this OMZ were mostly a vertical expansion of the core, which expanded at a similar rate as the eastern tropical South Atlantic OMZ due to loss of oxygen solubility in the region, which is already at very low oxygen concentrations. In conclusion, as seawater temperature increases as a result of CO₂ emission the OMZs will expand and strengthen as a result of changes in solubility and export of POC. These changes will limit migration and habitat zones resulting in fundamental changes in the marine ecosystem. The loss of dissolved oxygen will also result in changes to the carbon

and nitrogen cycles. Any expansion of hypoxia into the photic zone could be detrimental to marine ecosystems. Further research on the expansion of OMZ should include changes in ocean circulation and increases stratification in a comprehensive earth system model (see e.g. Moore et al., 2013). Changes in the ventilation of the ocean waters could lead to changes in both the intensity of the oxygen minimum zones as well as any future expansion.

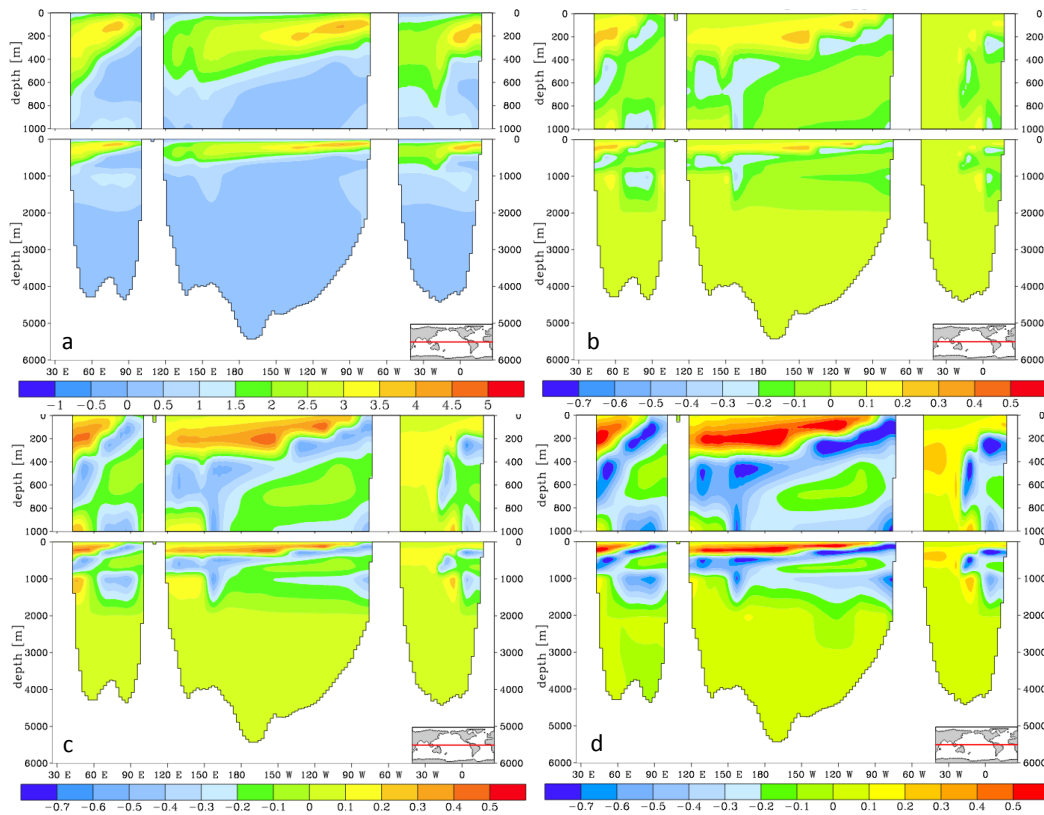


Figure 4-10 (a) Oxygen lost due to remineralization of particulate organic carbon for the reference run [$\mu\text{mol m}^{-2}\text{yr}^{-1}$]. Difference between the loss of oxygen due to remineralization between (b) 2 X CO₂ and reference run, (c) 4 X CO₂ and reference run (d) 8 X CO₂ and reference experiment.

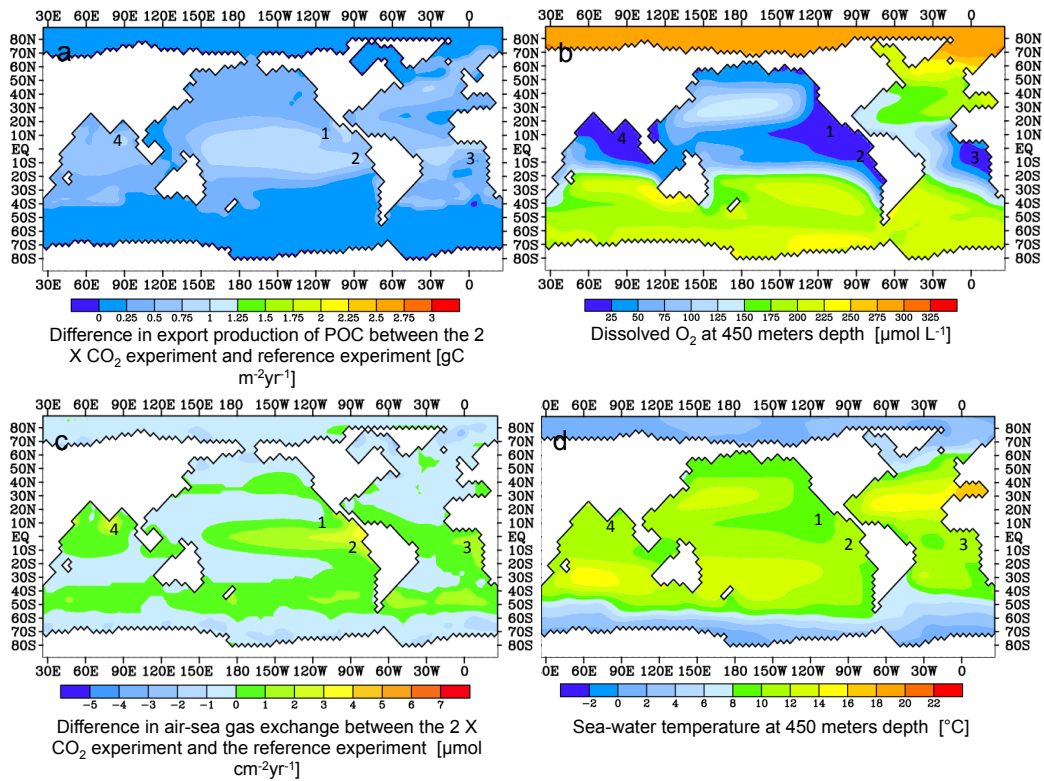


Figure 4-11 (a) Difference in export production of POC between the 2 X CO₂ experiment and reference experiment, (b) dissolved oxygen at 450 m depth for the 2 X CO₂ experiment, (c) difference in air-sea gas exchange between the 2 X CO₂ experiment and the reference experiment, and (d) sea-water temperature at 450 m depth. The numbers indicate the OMZ locations; [1] Eastern tropical North Pacific; 110°W, 10°N. [2] eastern tropical South Pacific; 85°W, 10°S. [3] eastern tropical South Atlantic; 5°W, 10°S. [4] Indian Ocean (Gulf of Bengal); 85°E, 7°N.

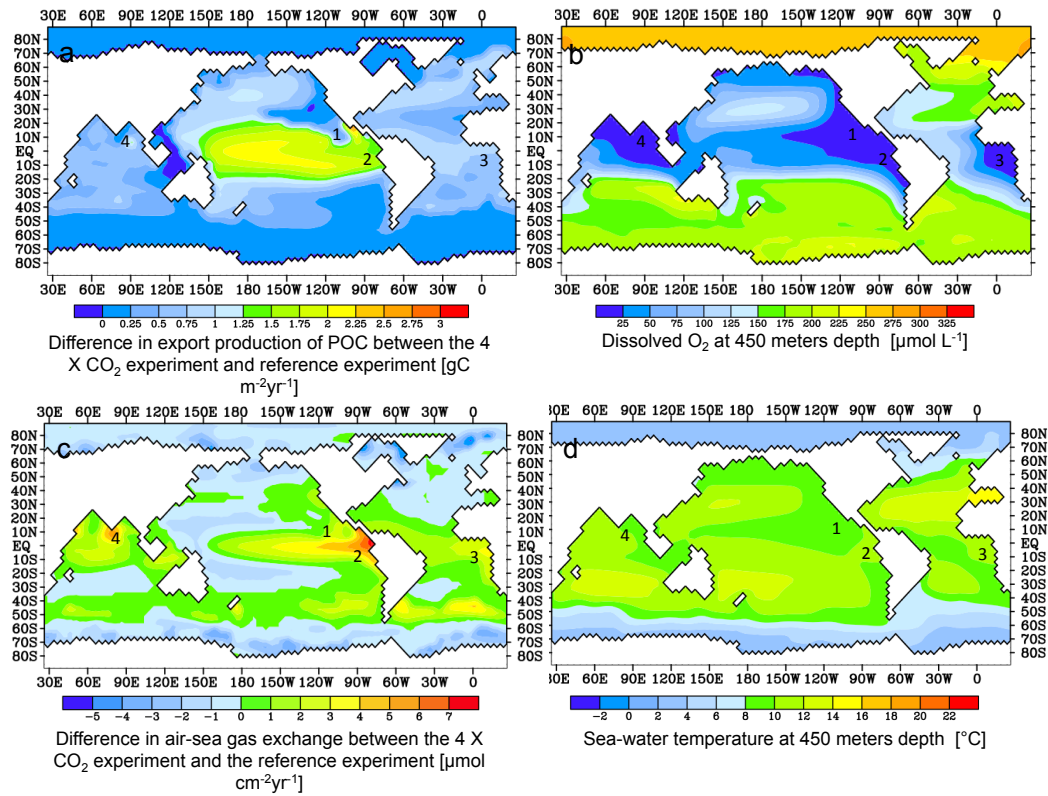


Figure 4-12 (a) Difference in export production of POC between the 4 X CO₂ experiment and reference experiment, (b) dissolved oxygen at 450 m depth for the 4 X CO₂ experiment, (c) difference in air-sea gas exchange between the 4 X CO₂ experiment and the reference experiment, and (d) sea-water temperature at 450 m depth. The numbers indicate the OMZ locations; [1] Eastern tropical North Pacific; 110°W, 10°N. [2] eastern tropical South Pacific; 85°W, 10°S. [3] eastern tropical South Atlantic; 5°W, 10°S. [4] Indian Ocean (Gulf of Bengal); 85°E, 7°N.

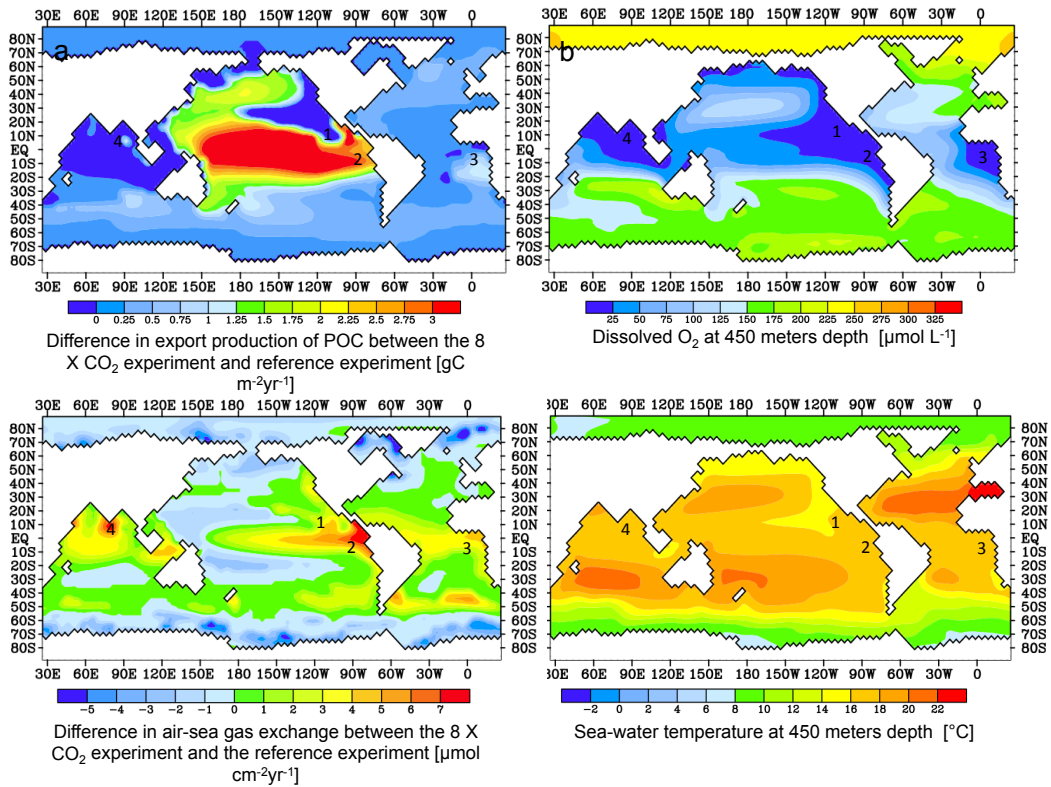


Figure 4-13 (a) Difference in export production of POC between the 8 X CO₂ experiment and reference experiment, (b) dissolved oxygen at 450 m depth for the 8 X CO₂ experiment, (c) difference in air-sea gas exchange between the 8 X CO₂ experiment and the reference experiment, and (d) sea-water temperature at 450 m depth. The numbers indicate the OMZ locations; [1] Eastern tropical North Pacific; 110°W, 10°N. [2] eastern tropical South Pacific; 85°W, 10°S. [3] eastern tropical South Atlantic; 5°W, 10°S. [4] Indian Ocean (Gulf of Bengal); 85°E, 7°N.

Chapter 5

Response of Ocean Acidification to Anthropogenic-Induced Carbon Emission

5.1 Introduction

The global decline of the pH values in the ocean in response to an increase in anthropogenic-induced CO₂ emission since 1850 and the associated impact of CO₂ on the acidification of the marine ecosystem will be discussed in the chapter. As atmospheric pCO₂ increases, the air-sea gas exchange results in higher dissolved CO₂ concentration in the surface water. A rise in the dissolved CO₂ concentration increases the calcium carbonate dissolution and decreases the pH value resulting in an increased bicarbonate concentration (Equation 1-1; Feely et al., 2004; Sabine et al., 2004). Rapid acidification in the ocean will have a direct effect on calcification, nutrient absorption of planktonic organism, carbon uptake, and the potential to influence primary productivity as well as higher trophic marine organisms (Brewer and Peltzer, 2009; Doney et al., 2009; Hofmann and Schellnhuber, 2009; Bijma et al., 2013).

The two biological pumps (soft tissue pump and CaCO₃ pumps; Volk and Hoffert, 1984) may be altered by the ocean acidification. The soft tissue pump may be reduced, because with a lower pH value ecosystem structure and photosynthesis may be reduced and thus would reduce the export of POC in the deep sea. The CaCO₃ pumps may be declined due to reduced calcification. The ratio of both biological pumps can be assessed by the ratio of export of POC and CaCO₃ to the deep-sea (Archer, 1994).

The preservation of CaCO₃ deposits in ocean sediments is widely used to infer the depth of calcium carbonate compensation (CCD) of the past. One prominent example of ocean acidification is the PETM (~55 Ma) with a rapid carbon injection (between approximately 2000 and 5000 PgC) inferred from a negative δ¹³C excursion (Zachos et al., 2008). This carbon pulse may have declined the pH value of surface water masses by

0.25 to 0.45 and may have led to a ~2 km shoaling of the carbonate compensation depth (CCD) in the South Atlantic Ocean (Zachos et al., 2005; Honisch et al., 2012) contributing to the largest extinction of benthic foraminifera in the last 75 Ma (Crowley and North, 1988). Another example of ocean acidification with a pH decrease of 0.05 units (or 0.11 relative to preindustrial levels) in response to elevated atmospheric pCO₂ concentration is the Pliocene (~3 Ma), a warming period with global SST increase of ~2.5°C (Bown et al., 2004; Haywood et al., 2009; Seki et al., 2010; Honisch et al., 2012). However, no calcification response has been documented during this period (Bown et al., 2004). Changes in pH have been reconstructed for the glacial-interglacial cycles derived from ratio of B/Ca in foraminifera (Spero et al., 1997; Hönisch and Hemming, 2005; Yu et al., 2007; Yu and Elderfield, 2007; Honisch et al., 2009; Pelejero et al., 2010; Honisch et al., 2012). The proxy indicated a lower pH in the surface waters during the interglacial period compared to glacial period as a result of changes in atmospheric pCO₂ levels. The CCD has deepened in the Pacific Ocean through the Cenozoic due to increased weathering of silicate and organic carbon bearing rocks (Griffith et al., 2011; Pälike et al., 2012) from ~3000 m in the early Cenozoic (~50 Ma) to a present day depth of ~4800 m.

A relationship between pH and O₂ has been verified for the estuary environment (Cochran and Burnett, 1996; Burnett, 1997) as well as an inverse relationship between O₂ and total dissolved inorganic carbon (DIC) in hypoxic waters in coastal regions (Frankignoulle et al., 1996; Yates et al., 2007; Feely et al., 2010; Cai et al., 2011; Paulmier et al., 2011). The preceding studies determined a coupling between acidification and hypoxia, which identified acidification as an additional stressor on biota in hypoxic waters. Brewer and Peltzer (2009) indicated that an increase in seawater pCO₂ within oxygen minimum zones could affect the 'respiration index' and thus the pO₂, which could contribute to the expansion of oxygen minimum zones (OMZ). Melzner et al., (2012)

collected data from the Boknis Eck Time Series Station (Kiel Bay) that included dissolved oxygen, salinity, temperature, DIC, and pH between 2009 and 2010 in order to explore the relationships between pH, DIC and dissolved oxygen concentrations in estuarine habitats with seasonal hypoxia. Using linear and nonlinear regression analysis Melzner et al., (2012) determined that estuarine environments are highly sensitive to effects of the increased DIC due to respiration and acidification. In this study we follow the approach of Melzner et al., (2012) and investigate how an increase in atmospheric $p\text{CO}_2$ affects the relationship between pH and dissolved O_2 concentration and DIC through the water column particularly in areas of low oxygen concentration. However, the approach may be limited because of the differences in salinity between the Baltic Sea and the global ocean environment.

5.2 Experimental design

The experimental design to explore the response of the pH value to increased atmospheric $p\text{CO}_2$ is similar to the methods used in Chapter 4. Biological efficiency was calculated by the sum of dissolved inorganic carbon (DIC) and dissolved organic carbon (DOC) at each data point and then applying Equation 1-7 at a depth of 3000 meters for the concentration of organic carbon in the deep sea.

5.3 Results

5.3.1 Sensitivity of ocean acidification to atmospheric carbon input.

The global average pH value decreased with each doubling of the atmospheric $p\text{CO}_2$ (Table 5-1); however, the globally averaged pH remained above 7.0. Feely et al., (2009) predicted a decrease in pH value in the tropical Pacific and Atlantic Oceans of 0.13 units for a doubling of atmospheric $p\text{CO}_2$. Water masses with a pH <7 were simulated in the 6 X CO_2 experiment (1688 ppmv) in the eastern tropical Pacific Ocean at a depth of 2000 meters. The acidic water masses (pH ~6.9) extended from the coast of

Central America to approximately 135°W. In the 8 X CO₂ scenario, a pH value of <7.0 (Figure 5-1) with the lowest pH value of 6.8 was simulated in a localized region of the North Pacific Ocean near 30°N 60°W in intermediate water masses below ~700 m and deep water masses. None of the simulations resulted in water masses with a pH of <7.0 for the Atlantic Ocean.

Table 5-1 Global sum of P_{CaCO₃} and global average DIC, pH, and carbonate ion concentrations for the 2 X, 4 X, 6 X and 8 X CO₂ simulations.

Experiment	CaCO ₃ Export Production [PgC yr ⁻¹]	DIC [μmol L ⁻¹]	pH	Carbonate Ion [μmol kg ⁻¹]
Reference	1.24	2137	7.82	116
2XCO ₂	1.23	2596	7.61	97
4XCO ₂	1.23	2858	7.34	64
6XCO ₂	1.22	2953	7.20	50
8XCO ₂	1.22	3003	7.10	43

Table 5-2 Lysocline depth and CCD for the 2 X, 4 X, 6 X and 8 X CO₂ simulations.

Experiment	Aragonite Lysocline Depth Ω _{ar} [meter]	Calcite Lysocline Depth Ω _{ca} [meter]	CCD [meter]
Reference	500	790	4800
2XCO ₂	380	580	4550
4XCO ₂	220	385	3400
6XCO ₂	150	295	3000
8XCO ₂	100	230	2700

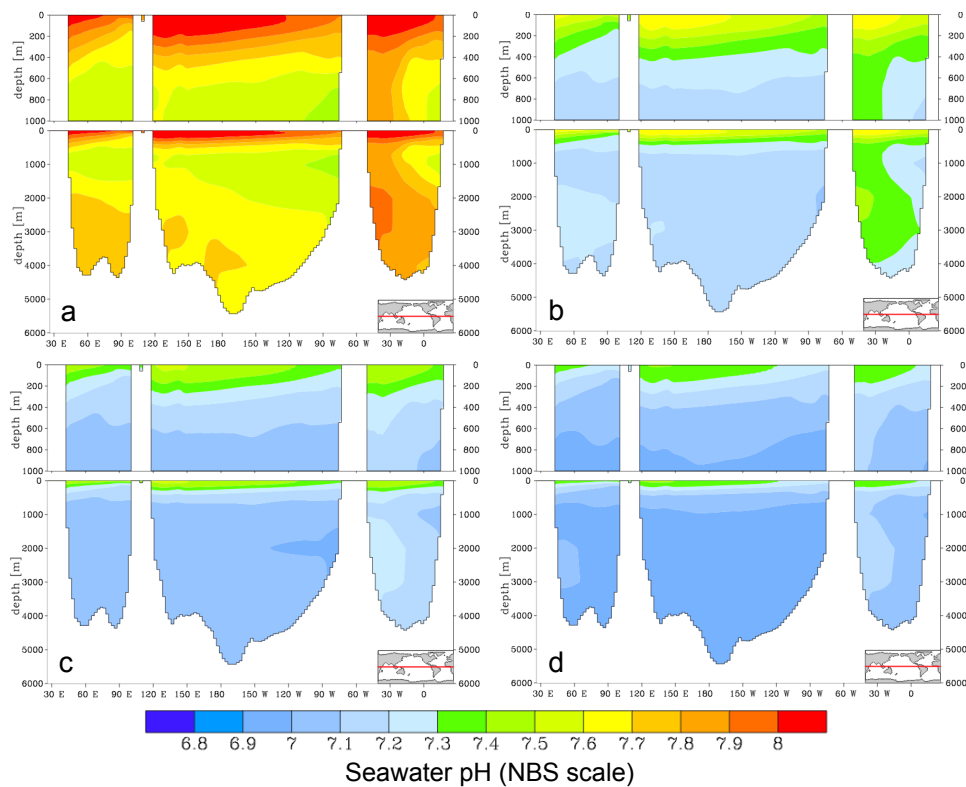


Figure 5-1 (a) pH value of the 1 X CO₂ (reference) experiment and the difference in pH value between (b) 4 X CO₂ experiment and reference experiment, (c) 6 X CO₂ experiment and the reference experiment, and (d) 8 X CO₂ experiment and the reference experiment simulated by HAMOCC 2.0.

Carbonate ion concentration decreased with a rise atmospheric pCO₂ (Table 5-1). For the 2 X CO₂ simulation [CO_3^{2-}] in the tropical Pacific and Atlantic Oceans decreased relative to the reference experiment by ~30 $\mu\text{mol kg}^{-1}$. For the 4 X CO₂ experiment, globally averaged [CO_3^{2-}] concentrations is similar to the 2 X CO₂ scenario with a decrease of ~32 $\mu\text{mol kg}^{-1}$ or 28% relative to the reference experiment. The simulated decrease in CO_3^{2-} concentrations presented in this study are modest compared to the 2 X CO₂ to the results of Feely (2010) which estimated a loss of ~50 $\mu\text{mol kg}^{-1}$. For the 4 X, 8 X, and 8 X CO₂ scenarios, the [CO_3^{2-}] and pH value decreased rapidly through

the surface water (Figure 5.2). The decrease in $[CO_3^{2-}]$ concentration led to a shoaling of both the Aragonite (Ω_{ar}) and Calcite (Ω_{ca}) saturation horizon in each simulation (Figure 5-2 and Table 5-1). The rate of shoaling for Ω_{ar} is slightly more rapid than the Ω_{ca} . However, both showed a significant decrease in shoaling rate for the 4 X and 8 X CO_2 experiments.

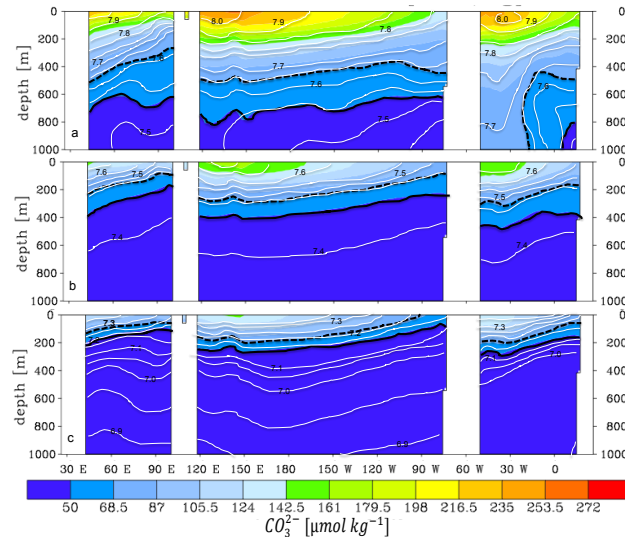


Figure 5-2 Zonal section of carbonate ion concentration at 2°N ($\mu\text{mol kg}^{-1}$) for (a) reference simulation, (b) 4 X CO_2 , and (c) 8 X CO_2 simulations. The solid and dashed black line indicates the calcite and aragonite saturation horizons. The contour interval for the pH value is 0.05 units.

Calcium carbonate deposition in the deep sea decreased as atmospheric pCO_2 and ocean acidification increased (Figure 5-1), reaching the lowest weight percentage in the 8 X CO_2 simulation (Figure 5-3). In the 4 X CO_2 simulation, no measurable $CaCO_3$ accumulation was detected in the Pacific Ocean with the exception of the Coral Sea and Tasman Sea east of Australia (average depth of 2500-3200 meters). $CaCO_3$ accumulation in the Pacific Ocean decreased by 60% at 4 X CO_2 experiment compared

to the reference simulation. The largest amount of CaCO_3 deposits in all simulations were located in the North Atlantic Ocean; however, for the 4 X CO_2 experiment the accumulation of CaCO_3 in sediments was limited to the shallow coastal regions in the West Atlantic Ocean extending along the coasts of North and South America as well as the Greenland Sea and Norwegian Sea. The 8 X CO_2 simulations resulted in only shallow CaCO_3 deposits due to the severe shoaling of the CCD (Table 5-1; Figure 5-7). In this simulation, CaCO_3 deposits occurred in isolated regions including the Gulf of Mexico, Timor Sea (west of Australia), Mozambique Channel, and parts of the Greenland and Norwegian Seas.

5.3.2 Regression analyses of O_2 , total DIC, and pH.

Regression analysis of 19 simulated water columns under preindustrial conditions as well as data from the CO_2 stabilization scenarios (Chapter 4) resulted in a linear relationship between pH and O_2 at all depths. Simulated water columns in regions of high dissolved oxygen concentrations and low biological efficiency (e.g. the Southern Ocean and high latitudes of the Atlantic Ocean) were similar to results of the estuary studies of Melzner et al., (2012) and Burnett (1997) suggesting a high correlation between pH value and the dissolved oxygen concentration. In all of the locations investigated an inverse relationship between total DIC and O_2 concentration was observed which is likely related to biological soft tissue pump. However, the regression analyses revealed that these correlations are decreased in areas of high biological efficiency (Figure 5-4 and Figure 5-5). The correlation between the dissolved O_2 and DIC and dissolved O_2 and pH in the Atlantic and Indian Oceans increased with increase atmospheric CO_2 concentrations, whereas it slightly decreased for the Pacific Ocean (Figure 5-6).

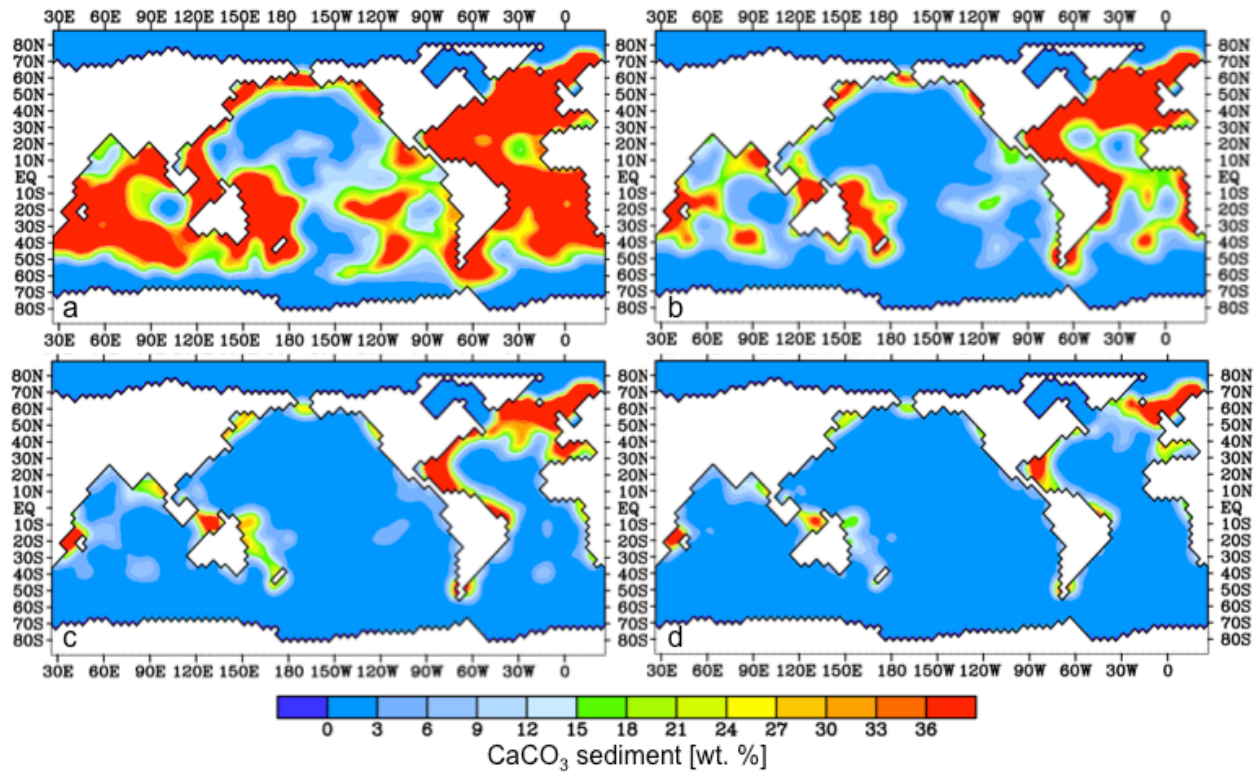


Figure 5-3 CaCO_3 accumulations in ocean sediments in percent weight for the (a) reference experiment, (b) 2 X CO_2 , (c) 4 X CO_2 , and (d) 8 X CO_2 simulations. Ocean depth contours are displayed in Figure 3-9.

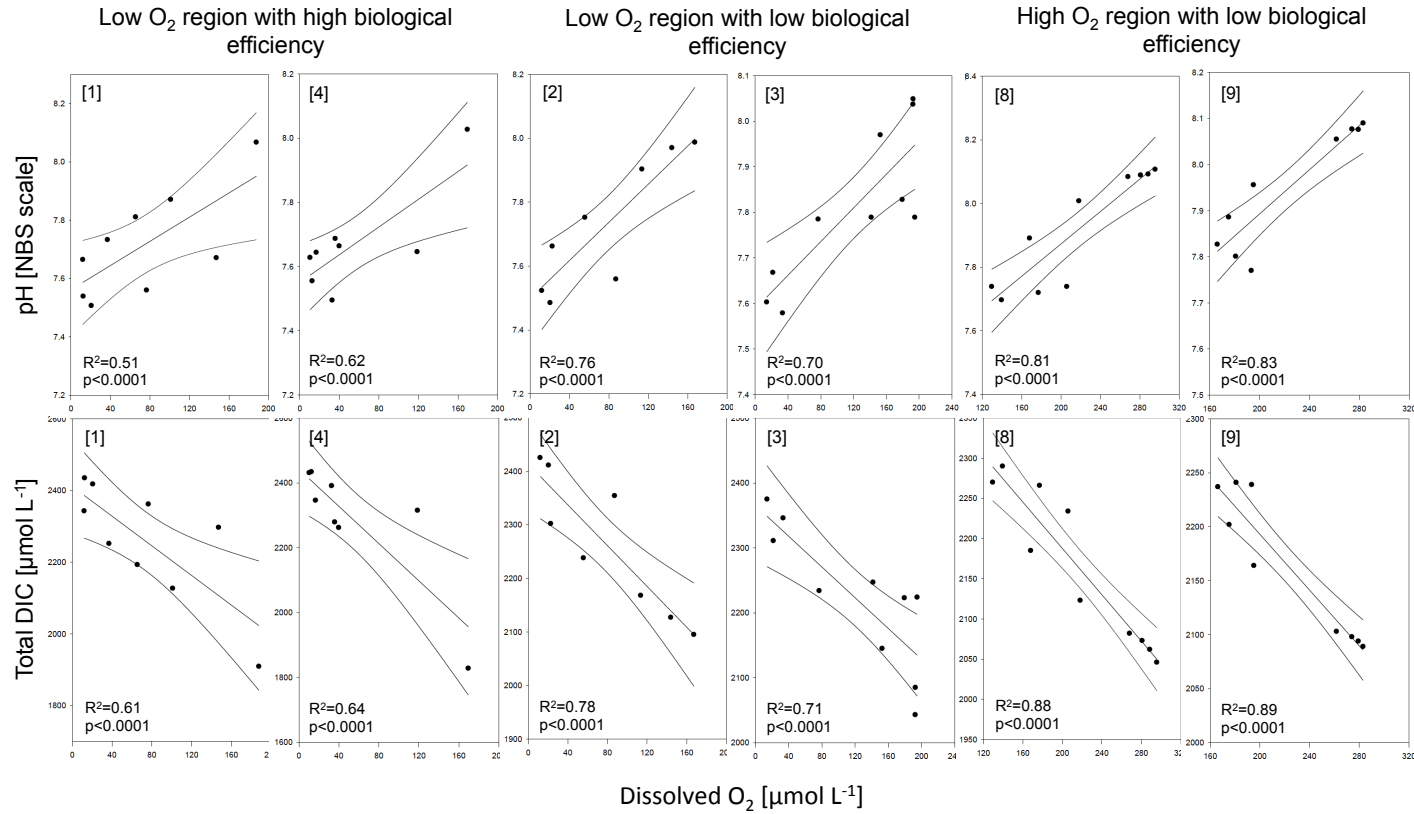


Figure 5-4 Regression analyses of the reference experiment for six simulated water columns between pH and dissolved O₂ (top) and between DIC and dissolved O₂ (bottom). Water column numbers are located in brackets in the top left hand corner. Note that the dots reflect the water masses at various depths for each location. The location of each water column is displayed in Figure 5-5

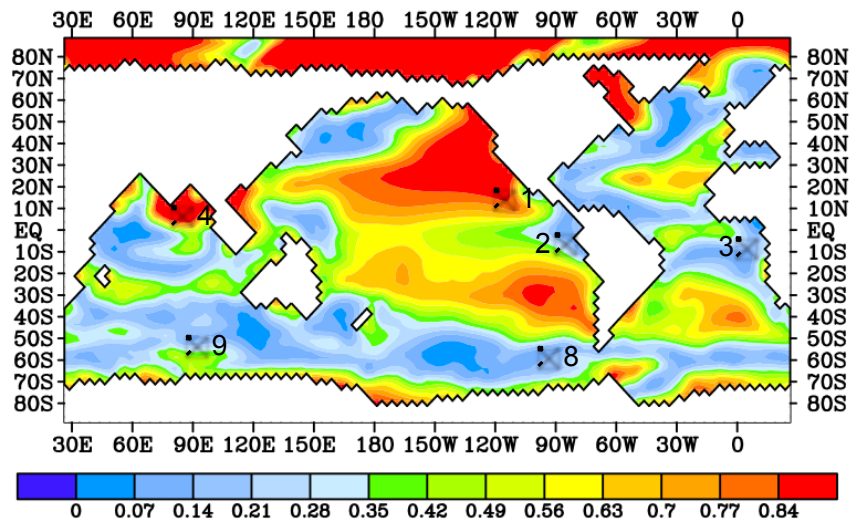


Figure 5-5 Location of water columns used for the regression analyses and the percent efficiency of the biological pump for the preindustrial simulations.

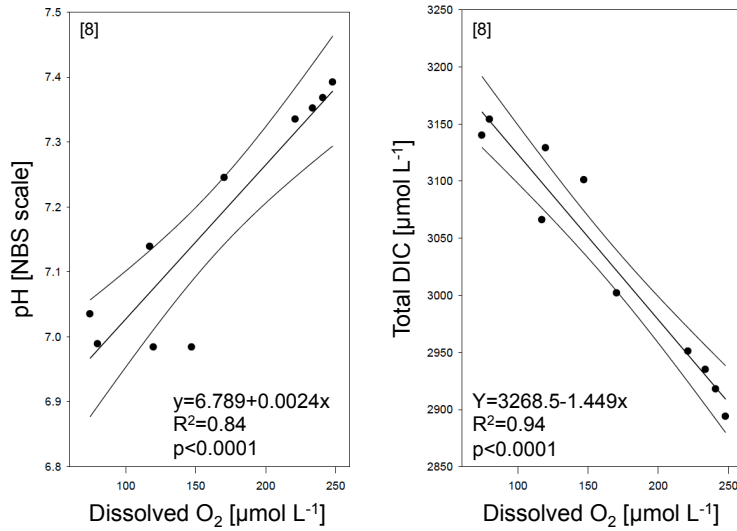


Figure 5-6 Regression analysis of a water column in the Southern Ocean simulated by the 8 X CO₂ experiment.

5.4 Discussion

The preindustrial and future simulations presented here explore the changes to the carbonate system and oxygen concentrations as atmospheric $p\text{CO}_2$ increases. The pH response to increase $p\text{CO}_2$ resulted in a nonlinear decrease per doubling of atmospheric $p\text{CO}_2$. The simulated decrease in pH value is comparable to that of the Pliocene (~3 Ma) which had an atmospheric $p\text{CO}_2$ concentration of ~560 ppmv equating to a doubling of preindustrial $p\text{CO}_2$. At eight times preindustrial $p\text{CO}_2$ concentration the pH value is comparable to the PETM; however, the time scale for the release CO_2 is unknown. Previous model estimates range from 1,000 years to 10,000 years (Panchuk et al., 2008; Zeebe et al., 2008). The rapid release of $p\text{CO}_2$ at a rate of 1% increase per year simulated in these sensitivity experiments could have resulted in a larger and more rapid decrease in the pH value due to the increase in DIC and the slow response time of pH buffering by weathering in the HAMOCC 2.0 model.

The greatest loss of simulated CaCO_3 deposition in sediment appeared to be in the deeper basins of the Pacific Ocean due to reduced CaCO_3 production with increased atmospheric $p\text{CO}_2$ and shoaling of the CCD in response to the ocean acidification. P_{CaCO_3} is reduced by ~4 TgC yr^{-1} per doubling $p\text{CO}_2$; however, the amount lost was slightly reduced at each doubling of $p\text{CO}_2$. Heinze (2004) estimated the loss of CaCO_3 production to be 50% by the year 2200 and therefore the total loss of CaCO_3 export production may be underestimated in this study due to the model assumption of a constant Redfield ratio. The globally averaged CCD shoaled with the increase of atmospheric $p\text{CO}_2$ with a rise of ~2100 m for the 8 X CO_2 simulation. This depth is consistent to estimates for the CCD shoaling in the Atlantic Ocean during the PETM (Zachos et al., 2008), which resulted in major shifts in marine planktonic communities (Kennett and Stott, 1991; Zachos et al., 2005). The exponential decline in the rate CCD

shoaling as pCO₂ increased suggests a reduction of CO₂ uptake by the ocean at atmospheric pCO₂ concentrations greater than 4 times the preindustrial pCO₂ (Figure 5-7) and this was further supported by the decline in shoaling of the calcite and aragonite saturation horizons (Table 5-1). The simulated CCD in this study was comparable to Cenozoic record of CCD and atmospheric CO₂ produced Pälke et al. (2012), This study, however, approximates a CCD at the same depth of the Eocene-Oligocene transition with an increase of <2 X CO₂, which is far less atmospheric pCO₂ than the reconstruction of Pälke et al. (2012) which estimates an atmospheric pCO₂ for E/O level at ~4 X CO₂. This discrepancy is due to the increased weathering rates during the Eocene-Oligocene transition owing to glaciation (Zachos et al., 1999; Zachos and Kump, 2005; Liu et al., 2009; Griffith et al., 2011; Pälke et al. 2012).

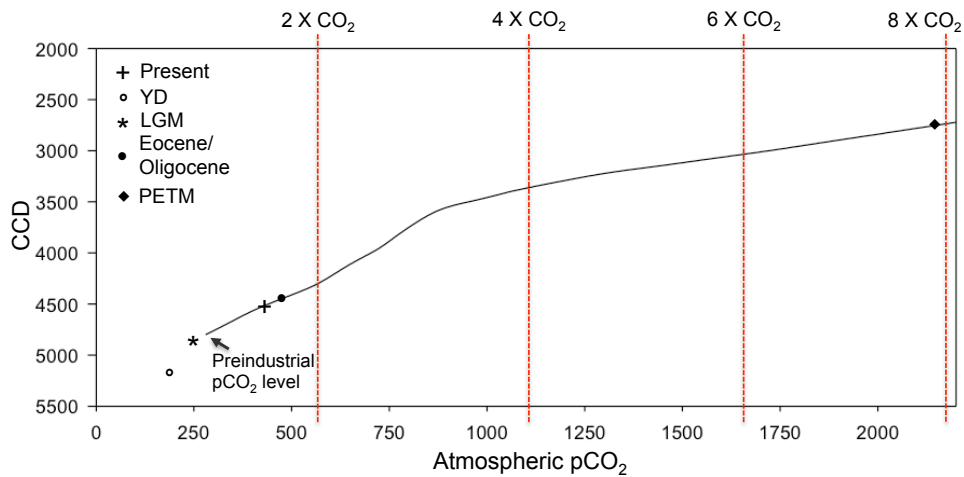


Figure 5-7 Simulated globally averaged CCD as a function of atmospheric pCO₂ levels from this study and the estimated CCD for the Pacific Ocean for the present (+), Younger Dryas (°) (Pälke et al., 2012), last glacial maximum (*) (Thunell et al., 1992; Pälke et al., 2012), Eocene/Oligocene (•) (Coxall et al., 2005; Liu et al., 2009; Pälke et al., 2012), and the CCD estimated derived from the Atlantic Ocean for the PETM (♦) (Zachos et al., 2005; Zachos et al., 2008).

Regression analysis with simulated water columns resulted in similar relationships between pH and dissolved O₂ as suggested by other studies (Burnett, 1997; Melzner et al., 2012); however, the correlation between pH value and dissolved O₂ was lower in areas of high biological pump efficiency (E_{bp}). The low correlation values indicate a strong biological control on deep-water dissolved O₂ concentration in these areas (Figure 5-4). The weaker relationship in high E_{bp} could also be attributed to the respiration parameterization in the model, which should increase DIC and decrease pH in regions of high productivity. When the biological component was reduced to zero (see reduced biology simulations; Figures 5-2, 5-3 and Chapter 4) there was a strong correlation between the pH value and dissolved oxygen as well as between DIC and dissolved oxygen in regions where the correlation was weak due to biological processes (Figure 5-8; Figure 5-9). Simulated cores from the Pacific Ocean suggest the strongest biological control on deep oxygen concentration of all the cores analyzed which further supports POC export as the primary mechanism for OMZ expansion in the Pacific Ocean (Chapter 4; Chapter 6). The lack of export production of POC from the surface could have also affected the relationship between DIC and dissolved O₂ concentration because of the reduction of vertical POC flux would lead to reduced loss of dissolved oxygen from remineralization. The correlation between dissolved O₂ concentration, pH and DIC was amplified in the Atlantic and Indian Oceans as atmospheric pCO₂ increased. However, it was decreased for the Pacific Ocean due to an increase in efficiency of the biological pump at higher atmospheric pCO₂ levels because the export production of POC is stimulated with a rise in sea surface temperature. It is important to note that the constant Redfield ratio in the model resulted in increased primary production in future simulations; however, other studies have indicated a decrease in production under future emission scenarios (Plattner et al., 2001; Riebesell et al., 2001; Zondervan et al., 2001). The

efficiency of the biological pump in the Atlantic Ocean was insignificantly changed with increased atmospheric pCO₂ levels whereas in the Indian Ocean efficiency was slightly decreased.

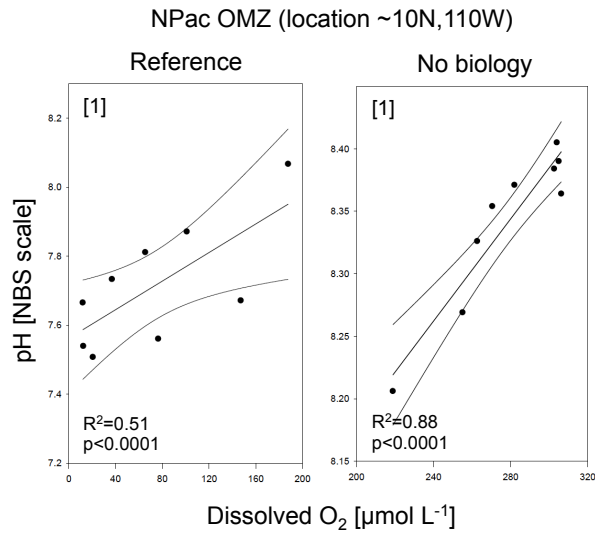


Figure 5-8 Regression analysis of pH value and dissolved O₂ concentration in a water column in the North Pacific (location [1] ~10N, 110W) for the reference experiment (left) and the reduced biology simulation (right).

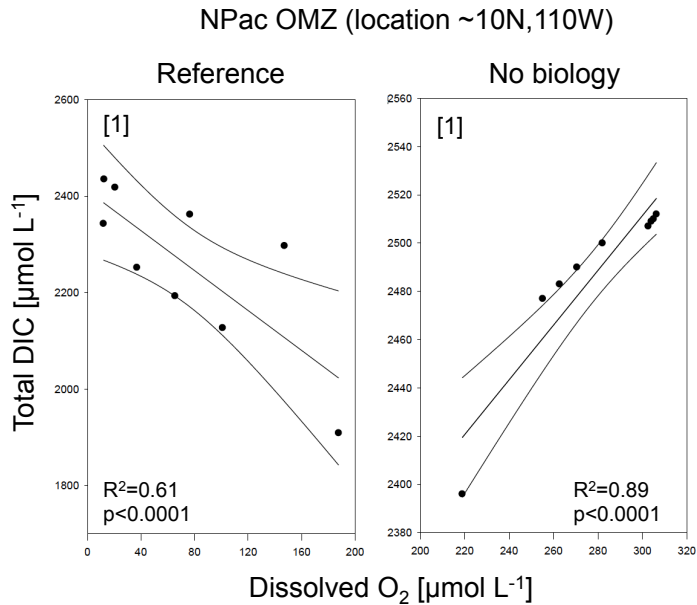


Figure 5-9 Regression analysis of DIC and dissolved O₂ concentration in a water column in the North Pacific (location ~10N, 110W) for the reference experiment (left) and the extinction simulation (right).

5.5 Conclusion and future research

As CO₂ emissions increase, aqueous CO₂ concentration will rise in the oceans due to the air-sea gas exchange, which will lead to increased ocean acidity and a decline in marine ecosystem diversity. The globally average calcite CCD shoaled at a rate of approximately 700 meters per doubling of atmospheric pCO₂ and the average ocean pH value decrease at ~0.2 units per doubling. For the 8 X CO₂ simulation, which corresponds to atmospheric pCO₂ levels if all fossil fuels would be burned (Caldeira and Wickett, 2003) the CCD shoaled to approximately 2100 m and the average ocean pH value decreased by ~0.7. The change in pH and CCD in response to total carbon emission, 4480 PgC or 8 times preindustrial pCO₂ levels, was similar to changes at the PETM (Zachos et al., 2005). The future change in CCD in response to increased pCO₂

and radiative forcing was consistent to changes throughout the Cenozoic (Pälike et al. 2012) with the exception of the Eocene-Oligocene transition which was a period of glaciation resulting in high weathering of silicate rock which was not considered in this study. The environmental response to such a carbon pulse would likely contribute to large shifts in planktonic communities as well as a possible extinction of benthic communities as documented in the geological record of the PETM (Thomas, 2006). The regression analyses indicated the same relationship between pH value and oxygen concentration for the water column in the open ocean as in studies of estuaries and areas of seasonal hypoxia (Cochran and Burnett, 1996; Frankignoulle et al., 1996; Burnett, 1997; Yates et al., 2007; Feely et al., 2010; Cai et al., 2011; Paulmier et al., 2011). However, there was a weaker correlation for areas with high biological efficiency that suggest a strong biological control or an under-representation of respiratory processes in the oceanic carbon cycle model. An increase in respiration processes would result in higher aqueous CO₂ concentrations and therefore a lower pH in these areas. The relationship between pH and O₂ suggest another stress for biological communities in low oxygen regions by lowering the respiratory index and extending dead zones (Brewer and Peltzer, 2009). However, Seibel and Childress (2013) have suggested that CO₂ concentration could never increase to the point of limiting the respiration reaction. Without regard to the necessary CO₂ concentration for cellular respiratory process to be interrupted, the relationship between pH value and dissolved oxygen concentration could still result further biological stress and an expansion of the dead zones due to the acidification of cellular tissue. Acidification of cellular tissue will limit protein function, in particular, the oxygen-binding protein, which may affect the dissolved oxygen concentration required for the organism to survive. Improved respiratory parameterization could strengthen the prediction of ocean acidification and dissolved oxygen concentration

especially in areas of high biological pump efficiency and thereby improving the models accuracy in simulating changes to the global carbon cycle. In conclusion, the sequestration of CO₂ by the ocean will have direct impacts on marine ecosystems, carbon cycle, and climate system and could lead to extinction of primary producers and well as higher organisms. Reduced species range and altered migration patterns of marine organism could impact fisheries and economies as well as have a profound effect on communities that rely on the ocean as their primary food source.

Chapter 6

Affects of Changes in Atmospheric Dust Deposition on Iron Fertilization and Dissolved Oxygen Concentration in the Ocean

6.1 Introduction

Atmospheric dust deposition is altered by the climate through changes in vegetation, desertification, and changes in dry and wet deposition. Atmospheric dust deposition can decrease by up to 50% (Mahowald et al., 2006) due to increased wet deposition in the tropics and polar regions due to climate change. Iron (Fe) fertilization by atmospheric dust deposition can stimulate the biological pump and thus the sequestering of atmospheric CO₂ in the ocean by enhancing productivity in iron-limited regions such as the Pacific and Southern Oceans (e.g. Joos et al., 1991; Buesseler et al., 2004; Aumont and Bopp, 2006; Blain et al., 2007; Buesseler et al., 2008; Buesseler, 2012). Iron is a limiting nutrient in the ocean (Martin and Fitzwater, 1988), as it is absorbed by phytoplankton and cyanobacteria and then assimilated by higher organisms allowing more efficient use of macronutrients. An increase in the biological efficiency and pCO₂ uptake enhances the POC export and thus reduces the dissolved oxygen concentration in the subsurface layers where POC is remineralized, in particular, the oxygen minimum zones (OMZ; see Chapter 1 and Chapter 4). Glacial-interglacial changes in the atmospheric dust deposition are hypothesized to be relevant in altering export production and particle flux in the deep sea (Ittekkot, 1993; Howard et al., 2006) and thus the air-sea gas exchange of CO₂ (Mahowald et al., 2006; Maher et al., 2010; Palastanga et al., 2013)

Predictions have ranged from significant decreases to increases in the amount of atmospheric dust under increased atmospheric pCO₂ conditions (Harrison et al., 2001; Tegen et al., 2004; Woodward et al., 2005; Mahowald et al., 2006). Prediction of

atmospheric dust concentrations is uncertain due in part due to natural and anthropogenic influences (Dale, 1997; Foley et al., 2005; Jickells et al., 2005; Neff et al., 2008) including atmospheric iron emissions from combustion engines and coal-fired power plants (Ito et al., 2012). Natural dust emissions originate from the Sahara and Sahel deserts of North Africa (67%), and the Gobi desert and other deserts of central Asia (25%) (Zender et al., 2004). Smaller amounts of natural dust are deposited in the Southern Ocean originating from Australia, South Africa, and Patagonia (8%) (Maher et al., 2010). The advection of dust from Africa leads to high dust deposition and Fe concentration in the Atlantic Ocean, particularly off the coast of North Africa.

Many studies (e.g. Joos et al., 1991; Buesseler et al., 2004; Aumont and Bopp, 2006; Blain et al., 2007; Buesseler et al., 2008; Buesseler, 2012) have examined processes linked to iron fertilization and its importance to the biological pump and the associated change in atmospheric pCO₂. In particular, these studies consider the importance of Fe limitation as a control of productivity and biomass in high-nitrate, low-chlorophyll (HNLC) regions of the ocean. This study examines the response of ocean oxygen concentration to ocean iron fertilization changes due to fluctuations in atmospheric dust under future emission scenarios including temperature feedbacks.

6.2 Experimental design

Atmospheric dust deposition, suspension of Fe from particles, and sediments re-suspension are sources of dissolved Fe in the water column. In this study, atmospheric dust deposition was modified in two sets of scenarios. In the first set of scenarios the dust deposition was decreased globally by 50% relative to the dust deposition from Mahowald et al. (2006), resulting in a global Fe deposition of 975 Tg yr⁻¹ and a second set of scenarios with global increase by 50% for a deposition of 2925 Tg yr⁻¹. These changes are consistent with the bulk of future dust deposition estimates which range from small

dust deposition changes to up to five times higher or lower than present-day (Hand et al., 2004; Tegen et al., 2004; Woodward et al., 2005; Mahowald et al., 2007; Mahowald et al., 2009; Maher et al., 2010; Martínez-García et al., 2011). This study did not consider regional changes in the dust emission, e.g. from land use changes, industrial combustion, or biomass burning (Guieu et al., 2005; Luo et al., 2008). For each altered dust scenario two simulations are conducted; one with preindustrial atmospheric pCO₂ concentration (1 X CO₂ DUST-50% and 1 X CO₂ DUST+50% respectively) and with four times the preindustrial atmospheric CO₂ level (4 X CO₂ DUST-50% and 4 X CO₂ DUST+50%). The 4 X CO₂ simulations included radiative forcing following Equation 4-2. For all experiments, iron solubility constant, ratio of Fe fixation to organic matter, and scavenging rate constant, which is limited in the study to the particle concentration in the water column, are taken from Palastanga et al. (2013). All sensitivity experiments were integrated for 15 kyrs. A brief description of the experiments are listed in Table 6-1, also see Chapter 2; Table 2-1. A recovery simulation was also completed with a 50% increase in dust deposition for 15,000-years and thereafter with present-day dust deposition for an additional 15,000 years. The recovery experiment was simulated with preindustrial atmospheric pCO₂ levels.

6.3 Results

6.3.1 Particulate organic carbon export response to changes in atmospheric dust deposition.

The reference (1 X CO₂) simulation was comparable to the preindustrial simulation of Palastanga (2013). Atmospheric dust depositions for the dust sensitivity experiments are shown in Figure 6-1. Compared to the observed dissolved Fe distribution of Johnson et al. (1997) the simulated dissolved Fe concentration are

Table 6-1 Description of the dust deposition experiments.

Experiments	Brief Description
1 X CO ₂ 4 X CO ₂	Preindustrial pCO ₂ and atmospheric dust deposition (1 X CO ₂) and a four time preindustrial pCO ₂ simulation with preindustrial atmospheric dust concentration (4 X CO ₂)
1 X CO ₂ DUST+50% 4 X CO ₂ DUST+50%	Preindustrial pCO ₂ and an increase in atmospheric dust deposition by 50% from preindustrial (1 X CO ₂ DUST+50%) and a four time preindustrial pCO ₂ simulation with a 50% increase in preindustrial atmospheric dust deposition (4 X CO ₂ DUST+50%)
1 X CO ₂ DUST-50% 4 X CO ₂ DUST-50%	Preindustrial pCO ₂ and a reduction in atmospheric dust deposition by 50% from preindustrial (1 X CO ₂ DUST-50%) and a four time preindustrial pCO ₂ simulation with a 50% reduction in preindustrial atmospheric dust deposition (4 X CO ₂ DUST-50%)

underestimated at the equatorial and subtropical latitudes and overestimated at the high latitudes. This model-data discrepancy was most likely due to the high scavenging rates, which are at a uniform rate in the model in order to more accurately represent surface Fe concentrations (Palastanga et al., 2013). In the Southern Ocean and equatorial Pacific Ocean the un-ballasted POC flux was comparable to Howard (2006) (Figure 6-3). However, the flux was underestimated by $\sim 200 \text{ mmol C m}^{-2}\text{yr}^{-1}$ for the subtropical North Atlantic Ocean and overestimated by $\sim 150 \text{ mmol C m}^{-2}\text{yr}^{-1}$ in the Indian Ocean. The total production export intensified in the increased dust deposition simulations by $\sim 5\%$ and $\sim 6\%$ for the 1 X CO₂ DUST+50% and 4 X CO₂ DUST+50% respectively and reduced by $\sim 9\%$ and $\sim 7\%$ in the 1 X CO₂ DUST-50% and 4 X CO₂ DUST-50%. The export production of POC accounted for $\sim 95\%$ of the change in total production export in all dust deposition experiments. Global mean total production export and export production of POC (P_{POC}) for each simulation are listed in Table 6-2.

6.3.2 Particulate organic carbon export response to an increase of atmospheric dust.

The most notable increase in POC export production (P_{POC}) for the 1 X CO₂ DUST+50% and the 4 X CO₂ DUST+50% simulations were in the equatorial Pacific Ocean and South Atlantic and Indian Ocean between 40°S-50°S (Figure 6-2). There was

also a significant increase in POC export production in the Sea of Okhotsk. The 1 X CO₂ DUST+50% simulation resulted in an increase of POC export by 20-30 gC m⁻² yr⁻¹ in the equatorial Pacific Ocean and ~10 gC m⁻² yr⁻¹ in the South Atlantic Ocean. An increase in atmospheric dust deposition did not increase the export production of POC in regions that are PO₄ limited such as the North Atlantic Ocean. Changes in POC export production due to increased dust deposition resulted in insignificant changes in the un-ballasted POC flux to the deep sea in areas that are not iron-limited as well as the Southern Ocean (Figure 6-3). The POC flux in the equatorial Pacific Ocean increased (~100 mmol C m⁻² yr⁻¹) in water masses above 1000 m; however, there was insignificant change in flux for masses below ~1000 m. The 4 X CO₂ DUST+50% experiment resulted in a further rise in POC export production from the 1 X CO₂ DUST+50% in the equatorial Pacific Ocean of >12 gC m⁻² yr⁻¹ due to the temperature-dependent increase in productivity and extended the area of high productivity eastward (Figure 6-2). The export production of POC (P_{POC}) in the Indian Ocean and South Atlantic Ocean increased by >6 gC m⁻² yr⁻¹. For the 4 X CO₂ DUST+50% scenario, the area of increased POC export production in the Sea of Okhotsk extends eastward into the Bering Sea. The 4 X CO₂ DUST+50% did not result in increased P_{POC} for regions that are not iron-limited due to temperature-dependent productivity or Fe fertilization.

6.3.3 Particulate organic carbon export response to a reduction of atmospheric dust.

The 1 X CO₂ DUST-50% experiment resulted in a reduction of P_{POC} for the equatorial Pacific Ocean and the South Atlantic and Indian Oceans between 40°S and 50°S (Figure 6-2). There was also a reduction in the Sea of Okhotsk. No significant change in P_{POC} occurred in areas of high Fe concentration within the tropical Atlantic and Indian Ocean in the 1 X CO₂ DUST-50% simulation. In Fe-limited regions, including the equatorial Pacific Ocean, P_{POC} decreased by 10-15 gC m⁻² yr⁻¹. The region of high

productivity in the tropical Pacific Ocean was restricted in the 1 X CO₂ DUST-50% to 10°N and 10°S of the equator and contracted eastward by 15° longitude. The POC flux to the deep-sea was reduced in the surface water of the eastern tropical Pacific Ocean by ~200 mmol C m⁻² yr⁻²; however, the change was insignificant in the intermediate and deep-water masses (Figure 6-3). The addition of 4 times the preindustrial pCO₂, including radiative forcing, resulted in little change in the P_{POC} in the 4 X CO₂ DUST+50%; however, the 4 X CO₂ DUST-50% resulted in significantly reduced productivity in the tropical Pacific Ocean compared to the 1 X CO₂ and 4 X CO₂ experiments (Figure 6-2). Also, the temperature-dependent productivity allowed for slightly more P_{POC} in the Sea of Okhotsk stretching into Bering Sea at higher atmospheric CO₂ concentration.

Table 6-2 Global means and percent change from the reference simulation for soluble iron, dissolved O₂, total productivity and export production of POC for the dust perturbation experiments after 15kyr integration.

Experiment	Soluble Fe		Global Mean Dissolved O ₂		Global Mean Total Production Export		Global Mean POC Production Export	
	[nmol L ⁻¹]	Δ [%]	[μmol L ⁻¹]	Δ [%]	[PgC m ² yr ⁻¹]	Δ [%]	[PgC m ² yr ⁻¹]	Δ [%]
1 X CO ₂ [reference]	0.9665		193.3		32.07		27.9	
4 X CO ₂	0.9726	0.6	167.1	-13.6	32.56	1.5	28.4	1.7
4 X CO ₂ DUST+50%	1.0169	5.2	165.1	-14.6	33.99	5.9	29.6	6.1
1 X CO ₂ DUST+50%	1.0234	5.8	190.0	-1.8	33.72	5.1	29.3	5.0
4 X CO ₂ DUST-50%	0.9365	-3.2	171.6	-11.3	29.77	-7.2	26.1	-6.5
1 X CO ₂ DUST-50%	0.9644	-0.2	199.5	3.9	29.26	-9.0	25.6	-8.3

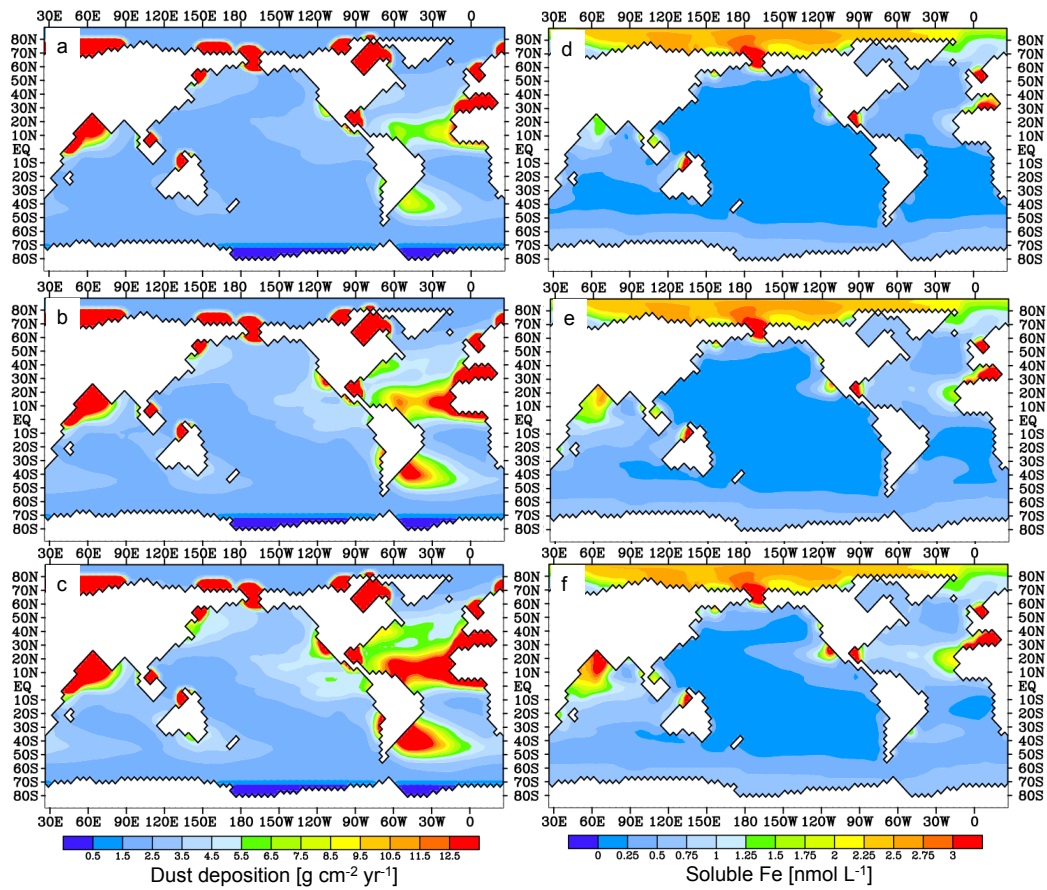


Figure 6-1 Simulated atmospheric dust deposition for the (a) 1 X CO₂ DUST-50%, (b) 1 X CO₂, and (c) 1 X CO₂ DUST+50% simulations and sea surface dissolved iron concentrations for the (d) 1 X CO₂ DUST-50%, (e) 1 X CO₂, and (f) 1 X CO₂ DUST+50% simulations.

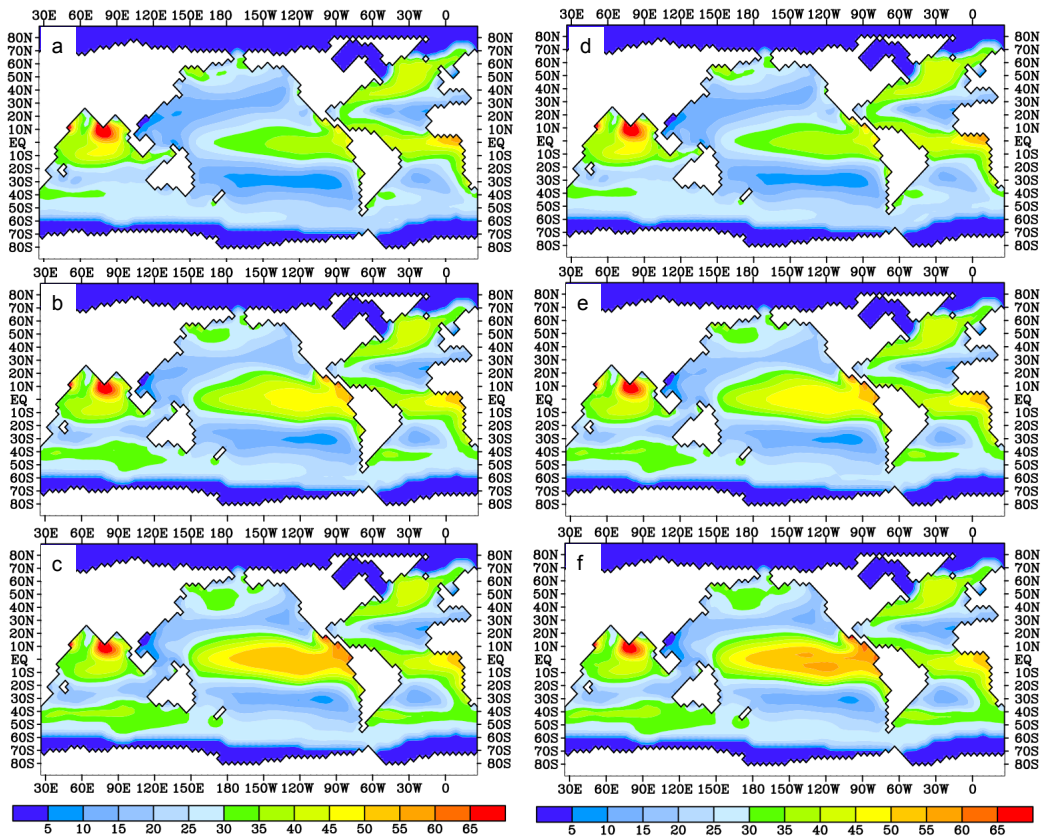


Figure 6-2 Export production of POC (P_{POC}) [$\text{gC m}^2 \text{yr}^{-1}$] for the (a) 1 X CO_2 DUST-50%, (b) 1 X CO_2 , (c) 1 X CO_2 DUST+50%, (d) 4 X CO_2 DUST-50%, (e) 4 X CO_2 , and (f) 4 X CO_2 DUST+50% experiments.

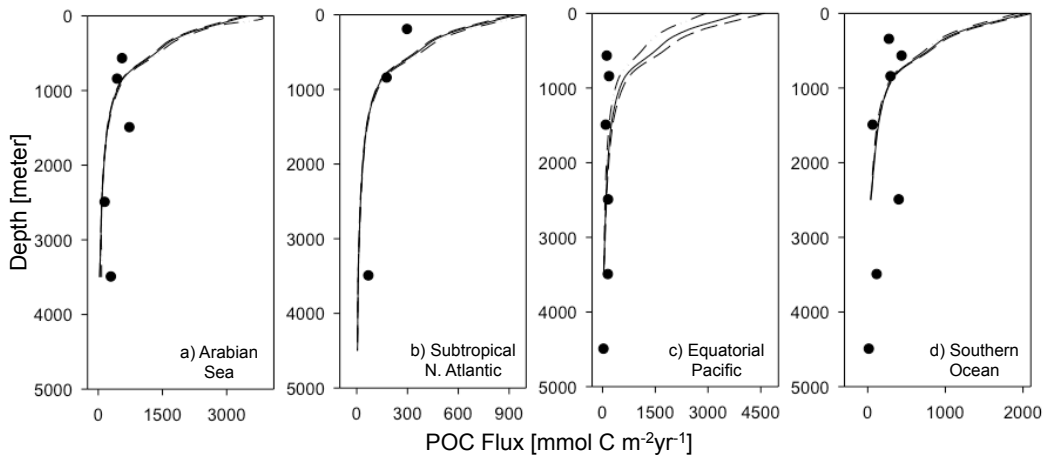


Figure 6-3 POC flux for the 1 X CO₂ (solid), 1 X CO₂ DUST+50% (dashed), and 1 X CO₂ DUST-50% (dashed-dot-dot) for the (a) Arabian Sea [10°S,70°E], (b) subtropical North Atlantic Ocean [30°N, 30°W], (c) equatorial Pacific Ocean [0°, 140°W], and (d) Southern Ocean [65°S, 110°W]. The circles are POC flux inferred from observations (Honjo et al., 1980; Honjo et al., 1995; Hammond et al., 1996; Rabouille et al., 1998).

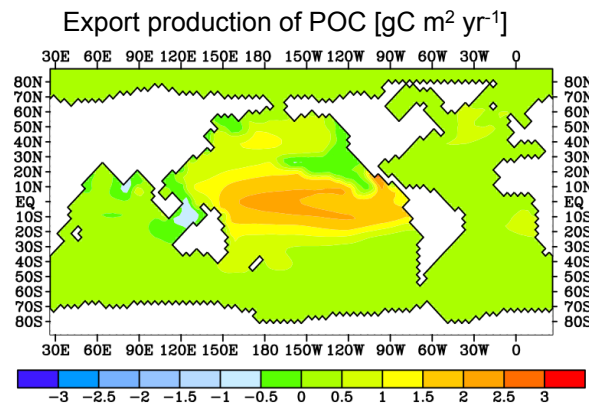


Figure 6-4 Increase in export production of particulate organic carbon (P_{POC}) due to temperature-dependent productivity (difference between the 4 X CO₂ and 1 X CO₂ experiment).

6.3.4 Global dissolved oxygen concentration response to changes in dust deposition.

The 1 X CO₂ DUST-50% and 1 X CO₂ DUST+50% simulations indicated a sensitivity of global mean dissolved oxygen concentrations to changes in atmospheric dust deposition. A reduction of dust deposition by 50% over the ocean increased global mean dissolved oxygen concentrations by >6 μmol O₂ L⁻¹ due to a reduced biological pump, whereas, an increase in dust deposition resulted in a depletion of dissolved O₂ concentration by ~3 μmol O₂ L⁻¹ due to increased biological pump (Table 6-1). Increased atmospheric pCO₂ and the associated radiative forcing resulted in a reduction of global mean dissolved oxygen concentrations by ~30 μmol L⁻¹ (see Chapter 4). With the reduction of atmospheric dust deposition at 4 time pCO₂ (4 X CO₂ DUST-50%) the loss of dissolved oxygen concentration was reduced to ~20 μmol L⁻¹ as compared to the 1 X CO₂ simulation. An increase in the atmospheric dust deposition by 50% (4 X CO₂ DUST+50%) resulted in a reduction of the global mean dissolved oxygen concentration by only ~2 μmol L⁻¹ as compared to the 4 X CO₂ simulation.

For the 1 X CO₂ simulations (1 X CO₂ DUST-50% and 1 X CO₂ DUST+50%) the changes in total ocean area with dissolved O₂ concentration of <50 μmol O₂ L⁻¹ were due to changes in the biological pump as a result of modifications in the dust deposition to the ocean. The 1 X CO₂ DUST-50% simulation resulted in a less efficient biological pump and the ocean area with dissolved O₂ concentration of <50 μmol O₂ L⁻¹ decreased by ~4% as compared to the 1 X CO₂ simulation. In contrast, the increased efficiency of the biological pump in the 1 X CO₂ DUST+50% simulation resulted in ~6% increase in total ocean area. The total ocean area with dissolved O₂ concentration of <50 μmol O₂ L⁻¹ (Table 6-2) expanded in both the 4 X CO₂ DUST-50% and 4 X CO₂ DUST+50% simulations relative to the 1 X CO₂ reference simulation. For the 4 X CO₂ DUST-50% simulation, the expansion was the result of temperature-dependent productivity and loss

of solubility due to higher seawater temperature. However, the larger expansion in the 4 X CO₂ DUST+50% simulation was due to the addition of Fe resulting in dust-stimulated biological pump. The largest increase in total ocean OMZ area occurred in the 4 X CO₂ DUST+50% scenario which resulted in a total area of over 90 × 10⁶ km² a 13% increase in total area relative the 1 X CO₂ simulation. However, the increased dust deposition by 50% at 4 times pCO₂ (4 X CO₂ DUST+50%) resulted in only a ~1% increase in total ocean area with dissolved O₂ concentration of <50 μmol O₂ L⁻¹ as compared to the 4 X CO₂ simulation with preindustrial dust deposition of Mahowald et al., (2006).

Table 6-3 Total ocean area (~volume) with a dissolved O₂ concentrations of ≤50 μmol L⁻¹, ≤20 μmol L⁻¹, for the experiments listed in Table 6-1 after 15k yrs of integration. Total ocean area is estimated from ETOPO1 (Eakins and Sharman, 2010).

Experiment	Total Ocean Area		Total Ocean Area in the Photic Zone [10 ⁵ km ²]	
	[10 ⁶ km ²]	Ocean Area [%]	km ²	Ocean Area in the Photic Zone [%]
Oxygen Concentration ≤ 50 μmol L ⁻¹				
1 X CO ₂ [reference]	60	16.6	15	0.43
4 X CO ₂	83	23.03	20	0.56
4 X CO ₂ DUST+50%	90	24.9	21	0.59
1 X CO ₂ DUST+50%	66	18.3	15	0.43
4 X CO ₂ DUST-50%	66	18.25	19	0.53
1 X CO ₂ DUST+50%	44	12.3	13	0.38
Oxygen Concentration ≤ 20 μmol L ⁻¹				
1 X CO ₂ [reference]	60	8.8	3.9	0.11
4 X CO ₂	83	12.3	5.7	0.16
4 X CO ₂ DUST+50%	90	13.4	6.1	0.17
1 X CO ₂ DUST+50%	66	10	5.7	0.16
4 X CO ₂ DUST-50%	66	9.59	5.0	0.14
1 X CO ₂ DUST+50%	44	6.19	2.7	0.075
Total Ocean	36	100		

6.3.5 Oxygen minimum zone response to changes in dust deposition.

Individual OMZ response to changes in atmospheric dust deposition differed between ocean basins (Figure 6-5 and Figure 6-6). The eastern subtropical Atlantic Ocean OMZ and the Indian Ocean OMZ responded similarly to changes in dust deposition with no significant dissolved oxygen response within the OMZs. In the Atlantic and Indian Ocean, dissolved oxygen concentration in all dust deposition perturbation simulations changed insignificantly in non-OMZ areas. The 1 X CO₂ DUST-50% simulation resulted in increased dissolved oxygen ($\sim 10 \mu\text{mol L}^{-1}$) along the east coast of South America extending into the South Atlantic Ocean. However, the increased dissolved oxygen in this region was diminished in the 4 X CO₂ DUST-50% simulation. For the 1 X CO₂ DUST-50% simulation, dissolved oxygen concentration increased in the deep Indian Ocean by $\sim 10 \mu\text{mol L}^{-1}$.

The North Pacific OMZ response to dust deposition was notable for each simulation indicating a high sensitivity in the North Pacific Ocean to perturbation in the dust deposition in this region. The 1 X CO₂ DUST+50 resulted in an expansion of the North Pacific OMZ core ($< 20 \mu\text{mol O}_2 \text{ L}^{-1}$) horizontally to 155°E and 10° westward longitude change from the 1 X CO₂ reference simulation and a deepening of the OMZ core by 500 m as compared to the 1 X CO₂ simulation (Figure 6-7). However, the 4 X CO₂ DUST+50% did not result in further expansion of the North Pacific OMZ as compared to the 4 X CO₂ simulation without additional dust deposition. Changes in the dissolved oxygen concentrations within the OMZ and its core were insignificant in the 1 X CO₂ DUST+50 and 4 X CO₂ DUST+50% simulations (Figure 6-6). For the 1 X CO₂ DUST+50% simulation there is a loss of $\sim 20 \mu\text{mol L}^{-1}$ below the OMZ at ~ 2200 m. With the addition of atmospheric pCO₂ (4 X CO₂ DUST+50%) the loss of dissolved oxygen concentration is reduced to $\sim 10 \mu\text{mol L}^{-1}$ at ~ 2200 m.

The horizontal expansion of the North Pacific OMZ core was restricted in the 1 X CO₂ DUST-50% and 4 X CO₂ DUST-50% simulations (Figure 6-7). The 1 X CO₂ DUST-50% reduced the extent of the OMZ by 5° longitude from the 1 X CO₂ reference simulation to approximately 170°E (Figure 6-5; Figure 6-6). A decrease in dust deposition of 50% neutralized the expansion of the OMZ due to increased radiative forcing in the 4 X CO₂ DUST-50% simulation relative to the 1 X CO₂ experiment. Therefore, the OMZ core in the North Pacific Ocean did not altered significantly (Figure 6-8). The greatest response of dissolved oxygen concentration in the Pacific Ocean to dust deposition occurred at the depths between 1000 and 3000 m with an increase in dissolved oxygen concentration of ~50 μmol L⁻¹ at 2500m in the 1 X CO₂ DUST-50% simulation (Figure 6-9). Dust deposition reduction scenarios (1 X CO₂ DUST-50% and 4 X CO₂ DUST-50%) resulted in an average increase of 5-10 μmol L⁻¹ in the surface waters of the Pacific Ocean (figure 6-6) in dissolved O₂ concentration and over 25 μmol O₂ L⁻¹ near the North Pacific OMZ.

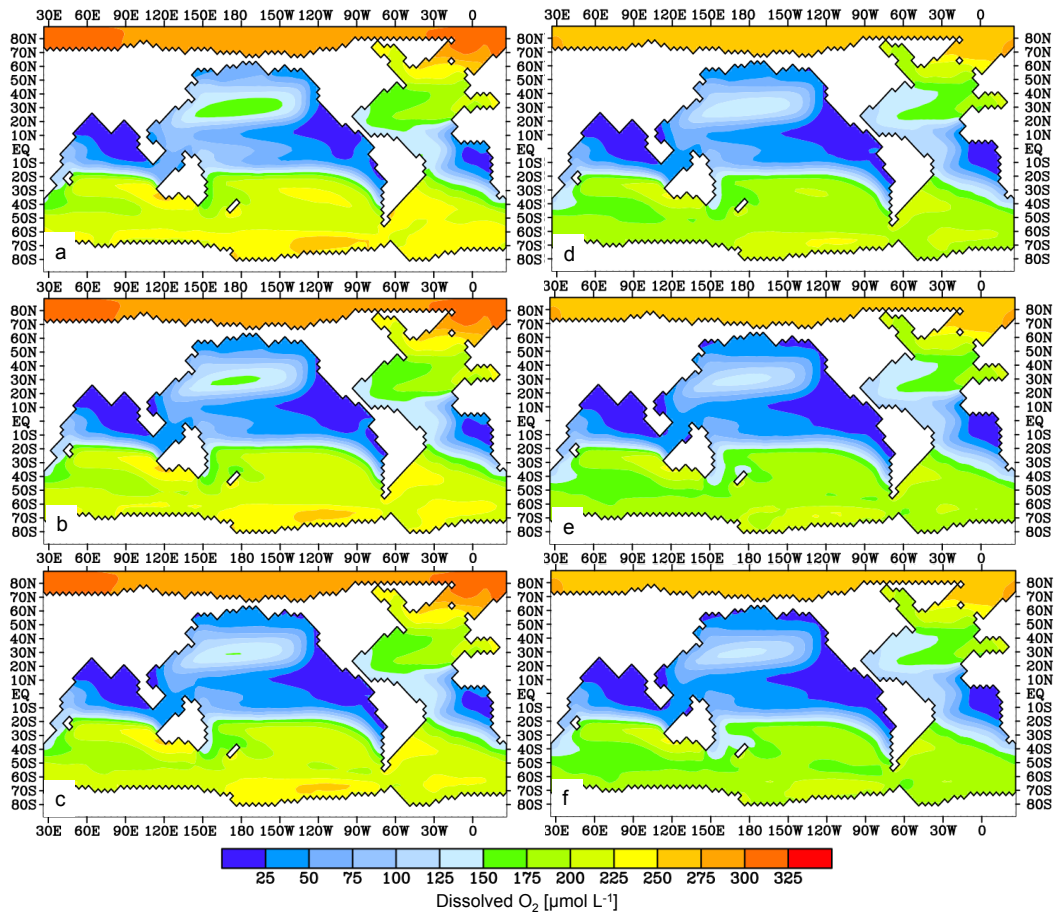


Figure 6-5 Dissolved oxygen concentration [$\mu\text{mol L}^{-1}$] at a depth of 400 m for the a) 1 X CO₂ DUST-50%, b) 1 X CO₂, c) 1 X CO₂ DUST+50%, d) 4 X CO₂ DUST-50%, e) 4 X CO₂, and f) 4 X CO₂ DUST+50% simulations.

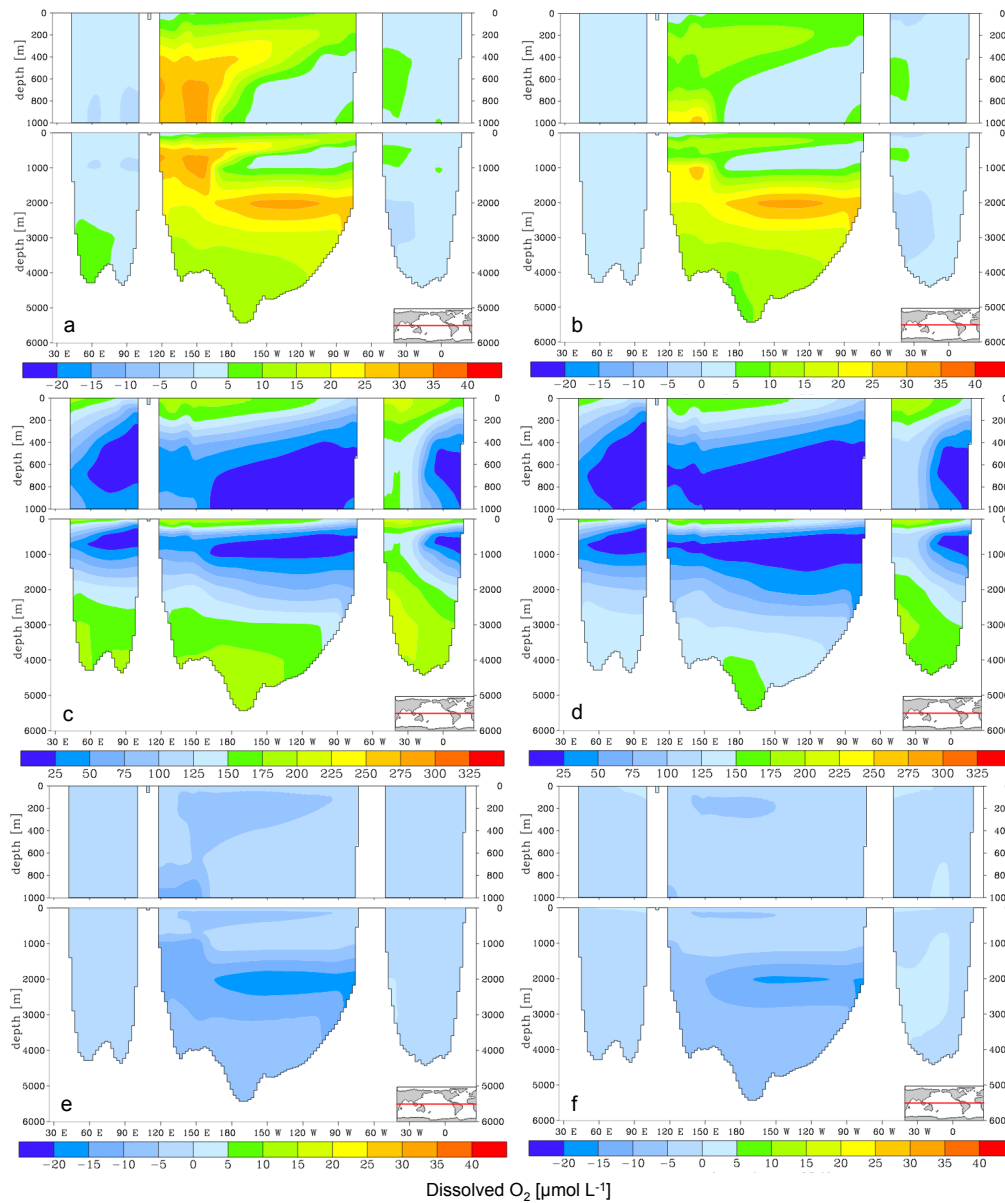


Figure 6-6 Difference between the simulations with a 50% reduction in atmospheric dust deposition for the a) 1 X CO₂ and b) 4 X CO₂ simulations. Dissolved oxygen concentration [$\mu\text{mol L}^{-1}$] for c) 1 X CO₂ and d) 4 X CO₂ simulations without a dust perturbation. Difference between the simulations with a 50% increase in atmospheric dust deposition for the e) 1 X CO₂ and f) 4 X CO₂ simulations.

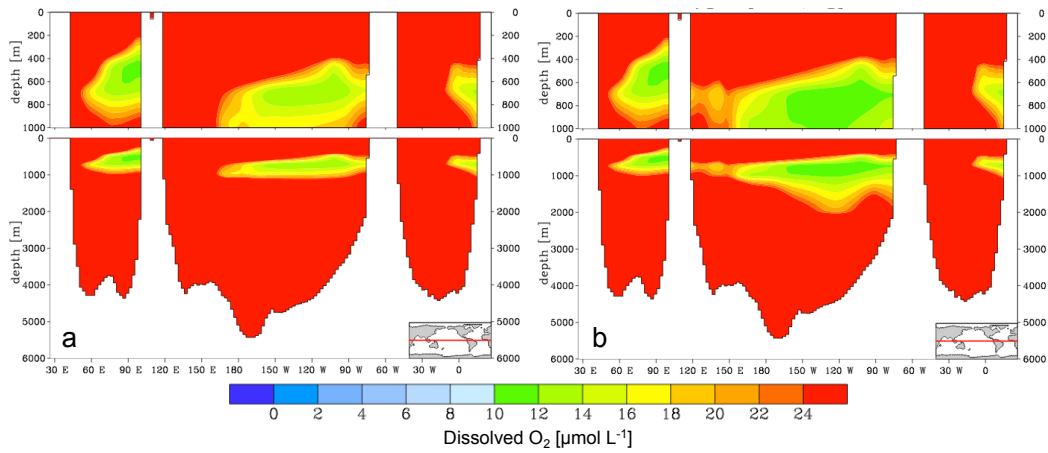


Figure 6-7 Dissolved oxygen concentrations [$\mu\text{mol L}^{-1}$] for the OMZ cores for (a) 4 X CO₂ DUST-50% and (b) 4 X CO₂ DUST+50% simulations.

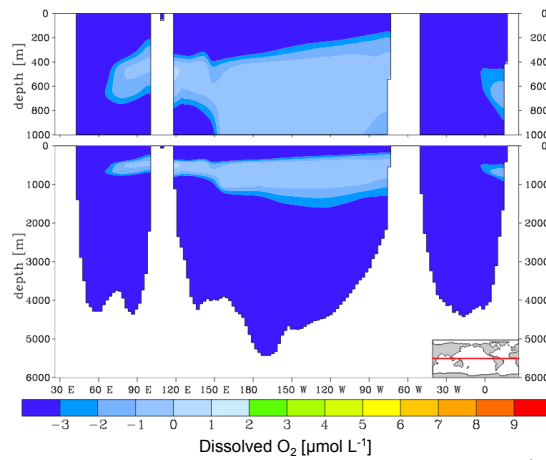


Figure 6-8 Difference in dissolved oxygen concentration [$\mu\text{mol L}^{-1}$] between the 4 X CO₂ DUST-50% and the 1 X CO₂ reference simulation.

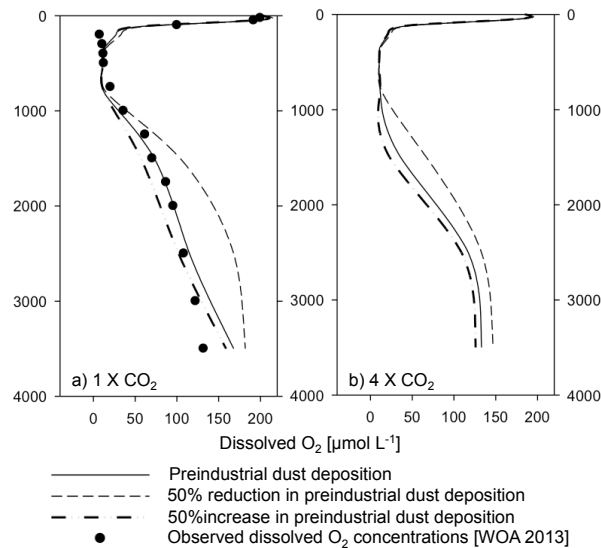


Figure 6-9 Vertical dissolved oxygen concentration profiles [$\mu\text{mol L}^{-1}$] at $\sim 10\text{N}$, 140W for the a) $1 \times \text{CO}_2$ and b) $4 \times \text{CO}_2$ simulations. The observations are taken from the World Ocean Atlas, 2013 (Garcia et al., 2014). Standard error of the mean; upper ocean: $0.54\text{--}2.86 \mu\text{mol L}^{-1}$, twilight zone: $0.42\text{--}2.32 \mu\text{mol L}^{-1}$, deep ocean: $0.36\text{--}1.98 \mu\text{mol L}^{-1}$.

6.4 Discussion

Future changes in atmospheric dust deposition will influence the export production of POC, vertical carbon flux, and dissolved oxygen concentration in the ocean. Unlike previous studies, the dust deposition experiments presented here focus on the response of the biological pump and dissolved oxygen concentration to perturbation in the Fe flux into the ocean. It is important to note that ocean stratification and changes in upwelling regions due to CO_2 radiative forcing were not considered and could have further implications on dissolved oxygen concentration and POC export. The most significant change in dissolved iron concentration in response to dust deposition occurred in the surface water of the Arabian Sea. An increase in dust deposition and thus, dissolved Fe concentration, in this region, did not significantly alter the export production

of POC with may be related to overestimated simulated soluble Fe utilization for the Arabian Sea. An increase in the dust deposition over the North Atlantic resulted in moderate rise in dissolved Fe concentrations in the surface water; however, this region is not Fe-limited and therefore the change in productivity relative to present day dust concentrations is insignificant for the dust perturbation simulations. The most notable change in the Atlantic Ocean in response to dust deposition perturbation was in the South Atlantic Ocean as a result of increased dust deposition off the coast of Patagonia. The atmospheric dust in this region is transported from Patagonia by the Westerlies to the South Atlantic Ocean. Thus an increase in dust deposition by 50% into the South Atlantic and Southern Ocean extending from Antarctica to the coast of South Africa resulted in a rise in export production in this region. For the reduced dust deposition the productivity in this region was significantly reduced and limited to $\sim 3^\circ$ degrees longitude from the coast of Patagonia. Increased dust deposition off the tip of South America could have implications for the Southern Ocean and the uptake of carbon emissions. The Fe fertilization of the Southern Ocean has been suggested as a method to increase the CO_2 uptake into the ocean (Chisholm et al., 2001; Buesseler and Boyd, 2003; Buesseler et al., 2004; Blain et al., 2007). However, this study also supports previous model simulations (Boyd and Law, 2001; Croot et al., 2001; Aumont and Bopp, 2006; Boyd and Ellwood, 2010) indicating that once Fe fertilization is diminished the export production drops below its initial state. For this study, the export production was reduced by 6% from the reference simulation (Figure 6-11).

The greatest response to dust deposition occurred in Fe-limited region of the equatorial Pacific Ocean where POC export production was increased by $>15 \text{ gC m}^{-2} \text{ yr}^{-1}$ at the equator. Note that increased CO_2 radiative forcing resulted in an rise in productivity due to the temperature dependency of productivity in the model; however, model studies

have also predicted reduced export production of POC due to reduced upwelling in the equatorial region and enhanced stratification in the high latitudes (e.g. Mikolajewicz et al., 2007). If warming of the sea surface persists and melting of sea ice increases, atmospheric dust deposition could enhance productivity by $\sim 25 \text{ gC m}^{-2} \text{ yr}^{-1}$ in the Sea of Okhotsk and Bering Sea. Iron fertilization by sea ice Fe has been the focus of several studies in the Southern Ocean and has been implicated in the sequestration of atmospheric carbon for the glacial-interglacial cycles (Sedwick and DiTullio, 1997; Wolff et al., 2006; Lannuzel et al., 2010). Aguilar-Islas et al., (2008) determined the same relationship between sea ice and algal blooms for the Bering Sea noting that seasonal ice melt lead to greater dissolved Fe concentrations in the upper 60 meters.

The global mean dissolve Fe concentration increased in the 4 X CO₂ simulation relative to the 1 X CO₂ reference simulation due to the increased solubility of Fe in less oxygenated water masses (13.6% decrease in the global mean dissolved oxygen concentration; Table 6-3). The response of dissolved Fe to changes in atmospheric dust deposition was less significant for the negative dust simulations as compared to the positive dust simulations. The 1 X CO₂ DUST-50% scenario only reduced the global mean dissolved Fe concentration by $\sim 0.2\%$ from the 1 X CO₂ simulation. This is due to reduced total productivity export by 9% which affected the amount of Fe utilization allowing more dissolved Fe to remain in the sea water. The 4 X CO₂ DUST-50% simulation resulted in a decrease of dissolved Fe by $\sim 3.2\%$; however, Fe utilization was increased in this simulation due to the temperature influence on total productivity. For the increased dust deposition simulations the dissolve iron concentrations were similar between the 1 X CO₂ DUST +50% and 4 X CO₂ DUST+50% with an increase of 5.8% and 5.2%, respectively. Total production export is slightly higher for the 4 X CO₂ DUST+50% resulting in more Fe utilization. The results presented here support the vast

number of studies (Berger et al., 1989; Ganopolski and Rahmstorf, 2001; Harrison et al., 2001; Mahowald and Luo, 2003; Buesseler et al., 2004; Mahowald et al., 2005; Aumont and Bopp, 2006; Mahowald et al., 2006; Blain et al., 2007; Buesseler, 2012) linking changes in total productivity due to fluctuations in atmospheric dust deposition and thus the efficiency of the ocean as a carbon sink.

This is the first study to examine the global dissolved oxygen concentration and OMZ response directly to Fe fertilization due to changes in atmospheric dust deposition. Due to the large regions of the ocean in which Fe is limited, reductions in atmospheric dust deposition had a stronger influence on the global average oxygen concentration of the ocean as compared to increased dust deposition due to a decrease in POC export and loss of dissolved oxygen concentration by remineralization below the photic zone (Table 6-2). The global mean dissolved oxygen concentration decreased for the 4 X CO₂ DUST+50% and 4 X CO₂ DUST-50% which suggest that the global dissolved oxygen concentration is significantly more sensitive to changes in temperature-dependent solubility than changes in atmospheric dust deposition. The 1 X CO₂ DUST+50% and 4 X CO₂ DUST+50% simulations resulted in a weaker global mean dissolved oxygen response to dust deposition suggesting that a 50% increase in atmospheric dust deposition with present day dust patterns only marginally decreases the surface area of the ocean that is Fe limited. However, it is important to note that changes in dust plumes due to anthropogenic influence or changes in atmospheric wind patterns due to climate change was not considered.

The dissolved oxygen concentration of the eastern subtropical South Atlantic and Indian Oceans OMZs were less sensitive to changes in dust deposition relative to the Pacific Ocean, due to a surplus of dissolved Fe in the surface water, and were more sensitive to changes in temperature-dependent solubility (see Chapter 4). Changes in

export production of POC strongly influenced the dissolved oxygen concentration of the eastern North Pacific OMZ (see Chapter 4); therefore, any changes in the atmospheric dust deposition would lead to Fe fertilization and thus affect extent of the OMZ. The OMZ core ($\leq 20 \mu\text{mol O}_2 \text{ L}^{-1}$) responded more significantly to increased dust deposition than the total OMZ area ($\leq 50 \mu\text{mol O}_2 \text{ L}^{-1}$). For the 1 X CO₂ DUST+50% simulation, the eastern North Pacific OMZ core deepened by ~500 m and the upper boundary of the OMZ core shoaled by over 300 meters. The significant change in the eastern North Pacific OMZ core was due to and the increased POC flux (Figure 6-3) and the resultant increase in remineralization within the OMZ. Dissolved Fe concentration in the surface waters above the OMZ area remained low in the increased dust deposition simulations suggesting a further strengthening of the biological pump in the equatorial Pacific Ocean (Figure 6-10). The addition of pCO₂ and radiative forcing in the 4 X CO₂ DUST+50% resulted in insignificant changes in the eastern North Pacific OMZ as compared to the 1 X CO₂ DUST+50% (Figure 6-5 and Figure 6-7). However, when dust deposition was reduced (4 X CO₂ DUST-50%) the expansion as a result of increased pCO₂ and seawater temperature is neutralized (Figure 6-8). This neutralization of the OMZ expansion from changes in pCO₂ and temperature was owed to the loss of productivity due the further reduction of dissolved iron in the surface waters in the equatorial Pacific. The significant response of the eastern North Pacific Ocean OMZ to perturbation in atmospheric dust supports the results presented in Chapter 4 that changes in the export-production and the biological pump influences the OMZ expansion in the Pacific Ocean OMZs.

The formation of the western subtropical Pacific Ocean OMZ (Figure 6-7; also see Chapter 4) in the 4 X CO₂ simulation was insensitive to perturbation of a 50% increase in dust deposition. However, under the same atmospheric and temperature conditions, a decrease in atmospheric dust deposition prevented any formation of the

western subtropical Pacific Ocean OMZ. Under present-day conditions, dust originating from the northwestern region of Australia is commonly advected northwestward and deposited over the Indonesian throughflow region. This region is characterized by transport of tropical Pacific water masses from the warm pool into the Indian Ocean (Wyrki, 1987). The extent of the OMZ in the western tropical Pacific Ocean was small with a minimum core concentration of $\sim 18 \mu\text{mol L}^{-1}$. Export production of POC in this region was significantly lower ($15 \text{ gC m}^{-2} \text{ yr}^{-1}$) compared to the POC export of the eastern equatorial Pacific Ocean ($55 \text{ gC m}^{-2} \text{ yr}^{-1}$). However, this study suggests that reduced atmospheric dust deposition originating from the deserts of Australia, thus decreased Fe fertilization, would not allow the formation of the western subtropical Pacific OMZ at high pCO_2 levels.

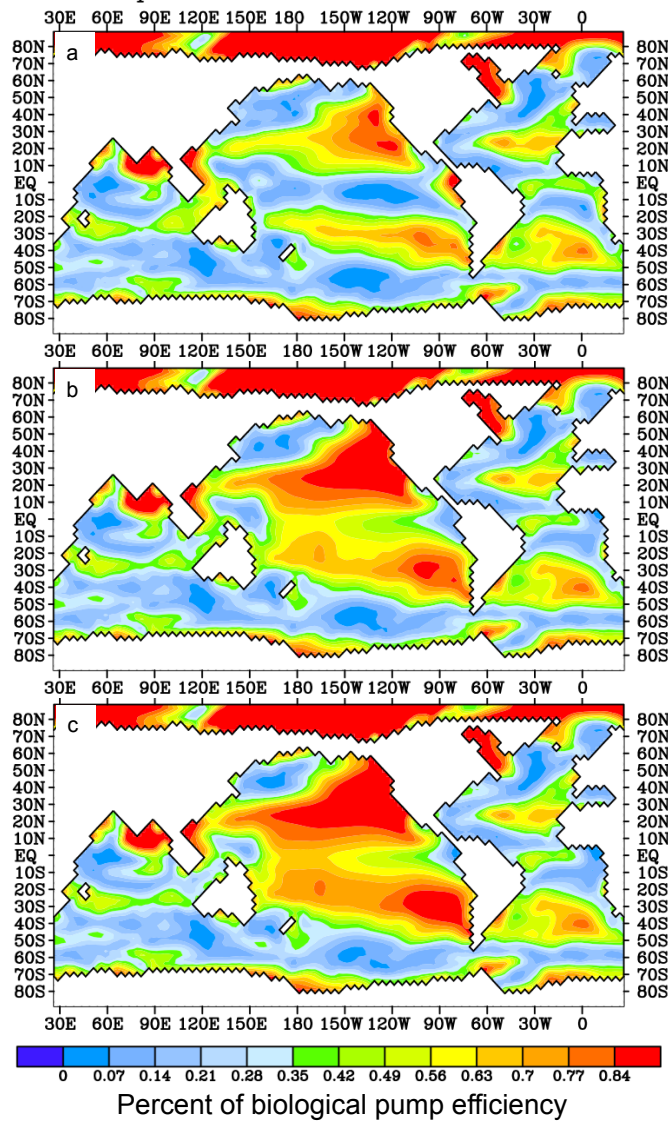


Figure 6-10 Biological pump efficiency for the a) 1 X CO₂ DUST-50%, b) 1 X CO₂, and c) 1 X CO₂ DUST+50% simulations.

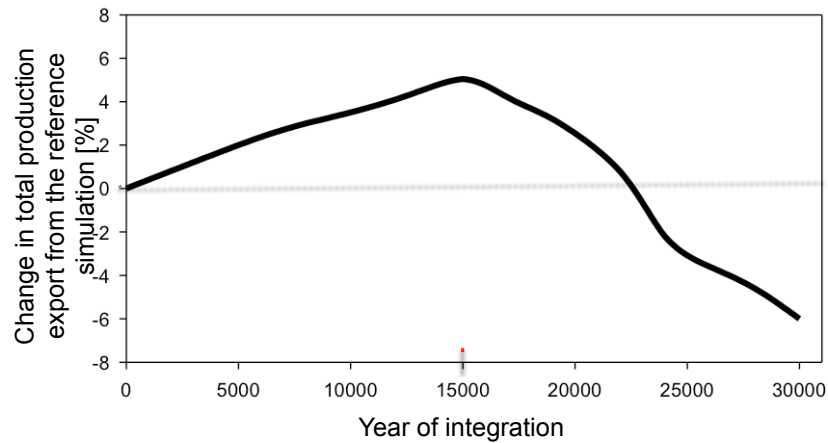


Figure 6-11 Change in total productivity through the dust perturbation and recovery simulations. The red line at indicates the time in which simulation starts to recover and the gray dotted line is the preindustrial total export production.

6.5 Conclusion and future perspectives

Iron is an important micronutrient for productivity in the ocean and is delivered to the open ocean by atmospheric dust deposition and hydrothermal activity. There is significant uncertainty in how dust deposition will alter in response to climate change. Also, the dust mineralogy and origin may alter due to human activities. The biological pump controls the vertical gradient of dissolved oxygen in the ocean and the uptake of CO_2 into the ocean; therefore, it is important to understand how changes in dust deposition influence the biological pump. Overall, changes to the global oxygen concentrations are largely influenced by the radiative forcing of greenhouse gases and to a lesser extent by fluctuations in Fe fertilization due to changes in dust concentration. The greatest response to increased Fe fertilization was in the Pacific Ocean due to the present day iron-depleted surface waters masses in this region. Simulations with 50% decrease in dust deposition had a significant influence on the dissolved oxygen concentration in the twilight zone. The simulations presented here indicated that a 50%

increase in atmospheric dust deposition was not a large enough to significantly reduce the extent of iron-limited surface waters masses and therefore didn't result in a significant change the dissolved oxygen concentration in the intermediate water masses. However, a reduction in dust deposition alters the extent of Fe limited regions and thus significantly reduces the export production and therefore OMZs. In order to further explore the influence of dust deposition under climate change scenarios, future changes in land-use and aerosol emission from coal-fired power plants should be considered which might lead to new or enhanced dust plumes. Rapid industrialization of emerging economies can result in significant increases in dissolved Fe concentration in the ocean and thus to depletions of dissolved oxygen in the proximity of the oxygen minimum zones.

References

- Aguilar-Islas, A., Rember, R., Mordy, C., and Wu, J., 2008, Sea ice-derived dissolved iron and its potential influence on the spring algal bloom in the Bering Sea: *Geophysical Research Letters*, v. 35, no. 24, DOI: 10.1029/2008GL035736.
- Algeo, T.J., Fraiser, M.L., Wignall, P.B., and Winguth, A.M., 2013, Permian–Triassic paleoceanography: *Global and Planetary Change*, v. 105, no. Complete, p. 1-6.
- Arakawa, A., and Lamb, V., 1977, Computational design of the basic dynamical processes of the UCLA General Circulation Model: *Methods in Computational Physics*, v. 17, p. 174-267.
- Archer, D., 1994, Effect of deep-sea sedimentary calcite preservation on: *Nature*, v. 367, p. 260-263.
- Archer, D., 2005, Fate of fossil fuel CO₂ in geologic time: *Journal of Geophysical Research: Oceans (1978–2012)*, v. 110, no. C9, DOI: 10.1029/2004JC002625.
- Archer, D.E., 1996, An atlas of the distribution of calcium carbonate in sediments of the deep sea: *Global Biogeochemical Cycles*, v. 10, no. 1, p. 159-174.
- Archer, D., Eby, M., Brovkin, V., et al., 2009, Atmospheric lifetime of fossil fuel carbon dioxide: *Annual Review of Earth and Planetary Sciences*, v. 37, no. 1, p. 117.
- Archer, D., Kheshgi, H., and Maier-Reimer, E., 1998, Dynamics of fossil fuel CO₂ neutralization by marine CaCO₃: *Global Biogeochemical Cycles*, v. 12, no. 2, p. 259-276.
- Archer, D., Kheshgi, H., and Maier-Reimer, E., 1997, Multiple timescales for neutralization of fossil fuel CO₂: *Geophysical Research Letters*, v. 24, no. 4, p. 405-408.

- Arthur, M.A., Dean, W.E., and Pratt, L.M., 1988, Geochemical and climatic effects of increased marine organic carbon burial at the Cenomanian/Turonian boundary: *Nature*, v. 335, no. 6192, p. 714-717.
- Aumont, O., and Bopp, L., 2006, Globalizing results from ocean in situ iron fertilization studies: *Global Biogeochemical Cycles*, v. 20, no. 2, DOI: 10.1029/2005GB002591.
- Baud, A., Magaritz, M., and Holser, W.T., 1989, Permian-Triassic of the Tethys: Carbon isotope studies: *Geologische Rundschau*, v. 78, no. 2, p. 649-677.
- Behrenfeld, M.J., Bale, A.J., Kolber, Z.S., Aiken, J., and Falkowski, P.G., 1996, Confirmation of iron limitation of phytoplankton photosynthesis in the equatorial Pacific Ocean: *Nature*, v.383, p. 508-511.
- Benton, M.J., and Twitchett, R.J., 2003, How to kill (almost) all life: the end-Permian extinction event: *Trends in Ecology & Evolution*, v. 18, no. 7, p. 358-365.
- Berger, W., Smetacek, V., and Wefer, G., 1989, Ocean productivity and paleoproductivity-an overview, in *Productivity of the Oceans present and past: Report of the Dahlem Workshop on Productivity of the Ocean*, Berlin, 1988 (WH Berger, VS Smetacek, G Wefer, eds) *Life sciences research reports* 44, Wiley & Sons, Chichester, p. 1-34.
- Berner, R.A., 2003, The long-term carbon cycle, fossil fuels and atmospheric composition: *Nature*, v. 426, no. 6964, p. 323-326.
- Berner, R.A., and Berner, E.K., 1997, Silicate weathering and climate: In *Tectonic uplift and climate change*, Springer US, p. 353-365.
- Bijma, J., Poertner, H., Yesson, C., and Rogers, A.D., 2013, Climate change and the oceans—What does the future hold?: *Marine pollution bulletin*, v. 74, no. 2, p. 495-505.

- Black, B.A., Elkins-Tanton, L.T., Rowe, M.C., and Peate, I.U., 2012, Magnitude and consequences of volatile release from the Siberian Traps: *Earth and Planetary Science Letters*, v. 317, p. 363-373.
- Blain, S., Quéguiner, B., Armand, L., et al., 2007, Effect of natural iron fertilization on carbon sequestration in the Southern Ocean: *Nature*, v. 446, no. 7139, p. 1070-1074.
- Bopp, L., Le Quéré, C., Heimann, M., Manning, A.C., and Monfray, P., 2002, Climate-induced oceanic oxygen fluxes: Implications for the contemporary carbon budget: *Global Biogeochemical Cycles*, v. 16, no. 2, p. 1022.
- Bopp, L., Resplandy, L., Orr, J.C., et al., 2013, Multiple stressors of ocean ecosystems in the 21st century: projections with CMIP5 models.: *Biogeosciences Discussions*, v. 10, no. 2, p. 6225-6245.
- Bown, P.R., Lees, J.A., and Young, J.R., 2004, Calcareous nannoplankton evolution and diversity through time. in *Coccolithophores*, Springer, p.481-508.
- Boyd, P., and Ellwood, M., 2010, The biogeochemical cycle of iron in the ocean: *Nature Geoscience*, v. 3, no. 10, p. 675-682.
- Boyd, P., and Law, C., 2001, The Southern Ocean iron release experiment (SOIREE)—introduction and summary: *Deep Sea Research Part II: Topical Studies in Oceanography*, v. 48, no. 11, p. 2425-2438.
- Brewer, P.G., and Peltzer, E.T., 2009, OCEANS. Limits to marine life: *Science* (New York, N.Y.), v. 324, no. 5925, p. 347-348.
- Broecker, W.S., 1997, Thermohaline circulation, the Achilles heel of our climate system: Will man-made CO₂ upset the current balance?: *Science*, v. 278, no. 5343, p. 1582-1588.

- Broecker, W.S., Kennett, J.P., Flower, B.P., Teller, J.T., Trumbore, S., Bonani, G., and Wolfli, W., 1989, Routing of meltwater from the Laurentide Ice Sheet during the Younger Dryas cold episode: *Nature*, v. 341, p. 318-321.
- Broecker, W.S. and Peng, T., 1982, *Tracers in the Sea*, Lamont-Doherty Geological Observatory, Columbia University.
- Buesseler, K.O., 2012, Biogeochemistry: The great iron dump: *Nature*, v. 487, no. 7407, p. 305-306.
- Buesseler, K.O., Doney, S.C., Karl, D.M., et al., 2008, ocean iron fertilization—moving forward in a sea of uncertainty: *atmosphere*, v. 1, p. 2.
- Buesseler, K.O., Andrews, J.E., Pike, S.M., and Charette, M.A., 2004, The effects of iron fertilization on carbon sequestration in the Southern Ocean: *Science (New York, N.Y.)*, v. 304, no. 5669, p. 414-417.
- Buesseler, K.O., and Boyd, P.W., 2003, Climate change. Will ocean fertilization work?: *Science (New York, N.Y.)*, v. 300, no. 5616, p. 67-68.
- Burnett, L.E., 1997, The challenges of living in hypoxic and hypercapnic aquatic environments: *American Zoologist*, v. 37, no. 6, p. 633-640.
- Cai, W., Hu, X., Huang, W., et al., 2011, Acidification of subsurface coastal waters enhanced by eutrophication: *Nature Geoscience*, v. 4, no. 11, p. 766-770.
- Caldeira, K., and Wickett, M.E., 2003, Oceanography: anthropogenic carbon and ocean pH: *Nature*, v. 425, no. 6956, p. 365-365.
- Cannariato, K.G., and Kennett, J.P., 1999, Climatically related millennial-scale fluctuations in strength of California margin oxygen-minimum zone during the past 60 ky: *Geology*, v. 27, no. 11, p. 975-978.
- Chisholm, S.W., Falkowski, P.G., and Cullen, J.J., 2001, Dis-crediting ocean fertilization: *Science*, v. 294, no. 5541, p. 309-310.

- Cochran, R.E., and Burnett, L.E., 1996, Respiratory responses of the salt marsh animals, *Fundulus heteroclitus*, *Leiostomus xanthurus*, and *Palaemonetes pugio* to environmental hypoxia and hypercapnia and to the organophosphate pesticide, azinphosmethyl: *Journal of experimental marine biology and ecology*, v. 195, no. 1, p. 125-144.
- Coxall, H.K., Wilson, P.A., Pälike, H., Lear, C.H., and Backman, J., 2005, Rapid stepwise onset of Antarctic glaciation and deeper calcite compensation in the Pacific Ocean: *Nature*, v. 433, no. 7021, p. 53-57.
- Croot, P.L., Bowie, A.R., Frew, R.D., et al., 2001, Retention of dissolved iron and Fe II in an iron induced Southern Ocean phytoplankton bloom: *Geophysical Research Letters*, v. 28, no. 18, p. 3425-3428.
- Crowley, T.J., and North, G.R., 1988, Abrupt climate change and extinction events in Earth history: *Science (New York, N.Y.)*, v. 240, no. 4855, p. 996-1002.
- Dale, V.H., 1997, The relationship between land-use change and climate change: *Ecological Applications*, v. 7, no. 3, p. 753-769.
- Dansgaard, W., Johnsen, S., Clausen, H., et al., 1993, Evidence for general instability of past climate from a 250-kyr ice-core record: *Nature*, v. 364, no. 6434, p. 218-220.
- Deutsch, C., Sarmiento, J.L., Sigman, D.M., Gruber, N., and Dunne, J.P., 2007, Spatial coupling of nitrogen inputs and losses in the ocean: *Nature*, v. 445, no. 7124, p. 163-167.
- Dickens, G.R., O'Neil, J.R., Rea, D.K., and Owen, R.M., 1995, Dissociation of oceanic methane hydrate as a cause of the carbon isotope excursion at the end of the Paleocene: *Paleoceanography*, v. 10, no. 6, p. 965-971.
- Doney, S.C., Fabry, V.J., Feely, R.A., and Kleypas, J.A., 2009, Ocean acidification: the other CO₂ problem: *Marine Science*, v. 1, p. 169-192.

- Driesschaert, E., Fichefet, T., Goosse, H., et al., 2007, Modeling the influence of Greenland ice sheet melting on the Atlantic meridional overturning circulation during the next millennia: *Geophysical Research Letters*, v. 34, no. 10, p. L10707.
- Dufresne, J., Fairhead, L., Le Treut, H., et al., 2002, On the magnitude of positive feedback between future climate change and the carbon cycle: *Geophysical Research Letters*, v. 29, no. 10, p. 43-1-43-4.
- Dunne, J.P., Armstrong, R.A., Gnanadesikan, A., and Sarmiento, J.L., 2005, Empirical and mechanistic models for the particle export ratio: *Global Biogeochemical Cycles*, v. 19, no. 4, GB4026, DOI: 10.1029/2004GB002390.
- Eakins, B., and Sharman, G., 2010, Volumes of the World's Oceans from ETOPO1: NOAA National Geophysical Data Center, Boulder, CO.
- Eisenman, I., Bitz, C.M., and Tziperman, E., 2009, Rain driven by receding ice sheets as a cause of past climate change: *Paleoceanography*, v. 24, no. 4, PA4209, DOI: 10.1029/2009PA001778.
- Eldholm, O., and Thomas, E., 1993, Environmental impact of volcanic margin formation: *Earth and Planetary Science Letters*, v. 117, no. 3, p. 319-329.
- Erba, E., Bartolini, A., and Larson, R.L., 2004, Valanginian Weissert oceanic anoxic event: *Geology*, v. 32, no. 2, p. 149-152.
- Erwin, D., 1994, The end-Permian mass extinction: a complex, multicausal extinction: *LPI Contributions*, v. 825, p. 33.
- Falkowski, P.G., Knoll, A.H., Falkowski, P., and Knoll, A., 2007, An introduction to primary producers in the sea: who they are, what they do, and when they evolved: *Evolution of Primary Producers in the Sea*, p. 1-6.

- Falkowski, P., Algeo, T., Codispoti, L., et al., 2011, Ocean Deoxygenation: Past, Present, and Future: *Eos*, v. 92, no. 46, p. 409-410.
- Feely, R.A., Alin, S.R., Newton, J., et al., 2010, The combined effects of ocean acidification, mixing, and respiration on pH and carbonate saturation in an urbanized estuary: *Estuarine, Coastal and Shelf Science*, v. 88, no. 4, p. 442-449.
- Feely, R.A., Doney, S.C., and Cooley, S.R., 2009, Ocean acidification: present conditions and future changes in a high-CO₂ world: *Annual Review of Marine Science*, v. 1, p. 169-192.
- Feely, R.A., Sabine, C.L., Lee, K., Berelson, W., Kleypas, J., Fabry, V.J., and Millero, F.J., 2004, Impact of anthropogenic CO₂ on the CaCO₃ system in the oceans: *Science*, v. 305, no. 5682, p. 362-366.
- Filippelli, G.M., 2008, The global phosphorus cycle: past, present, and future: *Elements*, v. 4, no. 2, p. 89-95.
- Filippelli, G.M., 2002, The global phosphorus cycle: *Reviews in mineralogy and geochemistry*, v. 48, no. 1, p. 391-425.
- Filippelli, G.M., 2001, Carbon and phosphorus cycling in anoxic sediments of the Saanich Inlet, British Columbia: *Marine Geology*, v. 174, no. 1, p. 307-321.
- Filippelli, G.M., Sierro, F., Flores, J., Vázquez, A., Utrilla, R., Pérez-Folgado, M., and Latimer, J., 2003, A sediment–nutrient–oxygen feedback responsible for productivity variations in Late Miocene sapropel sequences of the western Mediterranean: *Palaeogeography, Palaeoclimatology, Palaeoecology*, v. 190, p. 335-348.
- Foley, J.A., Defries, R., Asner, G.P., et al., 2005, Global consequences of land use: *Science (New York, N.Y.)*, v. 309, no. 5734, p. 570-574.

- Frankignoulle, M., Bourge, I., and Wollast, R., 1996, Atmospheric CO₂ fluxes in a highly polluted estuary (the Scheldt): *Limnology and Oceanography*, v. 41, no. 2, p. 365-369.
- Friedlingstein, P., DUFRESNE, J., Cox, P., and Rayner, P., 2003, How positive is the feedback between climate change and the carbon cycle?: *Tellus B*, v. 55, no. 2, p. 692-700.
- Friedlingstein, P., Cox, P., Betts, R., et al., 2006, Climate-carbon cycle feedback analysis: Results from the C4MIP model intercomparison: *Journal of Climate*, v. 19, no. 14, p. 3337-3353.
- Fuenzalida, R., Schneider, W., Garcés-Vargas, J., Bravo, L., and Lange, C., 2009, Vertical and horizontal extension of the oxygen minimum zone in the eastern South Pacific Ocean: *Deep Sea Research Part II: Topical Studies in Oceanography*, v. 56, no. 16, p. 992-1003.
- Galbraith, E.D., Kienast, M., Pedersen, T.F., and Calvert, S.E., 2004, Glacial-interglacial modulation of the marine nitrogen cycle by high-latitude O₂ supply to the global thermocline: *Paleoceanography*, v. 19, no. 4, DOI: 10.1029/2003PA001000.
- Ganeshram, R.S., Pedersen, T.F., Calvert, S., and François, R., 2002, Reduced nitrogen fixation in the glacial ocean inferred from changes in marine nitrogen and phosphorus inventories: *Nature*, v. 415, no. 6868, p. 156-159.
- Ganopolski, A., and Rahmstorf, S., 2001, Rapid changes of glacial climate simulated in a coupled climate model: *Nature*, v. 409, no. 6817, p. 153-158.
- Garcia, H. E., R. A. Locarnini, T. P. Boyer, J. I. Antonov, O.K. Baranova, M.M. Zweng, J.R. Reagan, D.R. Johnson, 2014, *World Ocean Atlas 2013, Volume 3: Dissolved Oxygen, Apparent Oxygen Utilization, and Oxygen Saturation*. S. Levitus, Ed., A. Mishonov Technical Ed.; NOAA Atlas NESDIS 75, p. 27.

- Garcia, H. E., R. A. Locarmini, T. P. Boyer, J. I. Antonov, O.K. Baranova, M.M. Zweng, J.R. Reagan, D.R. Johnson, 2014, *World Ocean Atlas 2013, Volume 4: Dissolved Inorganic Nutrients (phosphate, nitrate, silicate)*. S. Levitus, Ed., A. Mishonov Technical Ed.; NOAA Atlas NESDIS 76, p. 25.
- Glessmer, M., Park, W., and Oschlies, A., 2011, Simulated reduction in upwelling of tropical oxygen minimum waters in a warmer climate: *Environmental Research Letters*, v. 6, no. 4, p. 045001.
- Gray, J.S., Wu, R.S., and Or, Y.Y., 2002, Effects of hypoxia and organic enrichment on the coastal marine environment: *Marine Ecology Progress Series*, v. 238, no. 1, p. 249-279.
- Griffith, E.M., Paytan, A., Eisenhauer, A., Bullen, T.D., and Thomas, E., 2011, Seawater calcium isotope ratios across the Eocene-Oligocene transition: *Geology*, v. 39, no. 7, p. 683-686.
- Grotzinger, J.P., and Knoll, A.H., 1995, Anomalous carbonate precipitates: is the Precambrian the key to the Permian?: *Palaios*, p. 578-596.
- Guieu, C., Bonnet, S., Wagener, T., and Loÿe-Pilot, M., 2005, Biomass burning as a source of dissolved iron to the open ocean?: *Geophysical Research Letters*, v. 32, no. 19, DOI: 10.1029/2005GL022962.
- Hammond, D., McManus, J., Berelson, W., Kilgore, T., and Pope, R., 1996, Early diagenesis of organic material in equatorial Pacific sediments: stoichiometry and kinetics: *Deep Sea Research Part II: Topical Studies in Oceanography*, v. 43, no. 4, p. 1365-1412.
- Hand, J., Mahowald, N., Chen, Y., Siefert, R., Luo, C., Subramaniam, A., and Fung, I., 2004, Estimates of atmospheric-processed soluble iron from observations and a global mineral aerosol model: Biogeochemical implications: *Journal of*

- Geophysical Research: Atmospheres (1984–2012), v. 109, no. D17, DOI: 10.1029/2004D004574.
- Handoh, I.C., and Lenton, T.M., 2003, Periodic mid-Cretaceous oceanic anoxic events linked by oscillations of the phosphorus and oxygen biogeochemical cycles: *Global Biogeochemical Cycles*, v. 17, no. 4, p. 1092.
- Hansen, J., Fung, I., Lacis, A., et al., 1988, Global climate changes as forecast by Goddard Institute for Space Studies three dimensional model: *Journal of Geophysical Research: Atmospheres (1984–2012)*, v. 93, no. D8, p. 9341-9364.
- Harrison, S.P., Kohfeld, K.E., Roelandt, C., and Claquin, T., 2001, The role of dust in climate changes today, at the last glacial maximum and in the future: *Earth-Science Reviews*, v. 54, no. 1, p. 43-80.
- Hay, W.W., Deconto, R.M., and Wold, C.N., 1997, Climate: Is the past the key to the future?: *Geologische Rundschau*, v. 86, no. 2, p. 471-491.
- Haywood, A.M., Dowsett, H.J., Valdes, P.J., Lunt, D.J., Francis, J.E., and Sellwood, B.W., 2009, Introduction. Pliocene climate, processes and problems: *Philosophical transactions. Series A, Mathematical, physical, and engineering sciences*, v. 367, no. 1886, p. 3-17.
- Heinze, C., 2004, Simulating oceanic CaCO₃ export production in the greenhouse: *Geophysical Research Letters*, v. 31, no. 16, DOI: 10.1029/2004GL020613.
- Heinze, C., Gehlen, M., and Land, C., 2006, On the potential of ²³⁰Th, ²³¹Pa, and ¹⁰Be for marine rain ratio determinations: A modeling study: *Global Biogeochemical Cycles*, v. 20, no. 2, DOI: 10.1029/2005GB002595.
- Heinze, C., Hupe, A., Maier-Reimer, E., Dittert, N., and Ragueneau, O., 2003, Sensitivity of the marine biospheric Si cycle for biogeochemical parameter variations: *Global Biogeochemical Cycles*, v. 17, no. 3, DOI: 10.1029/2002BG001943.

- Heinze, C., Maier-Reimer, E., Winguth, A.M., and Archer, D., 1999, A global oceanic sediment model for long-term climate studies: *Global Biogeochemical Cycles*, v. 13, no. 1, p. 221-250.
- Heinze, C., Maier-Reimer, E., and Winn, K., 1991, Glacial pCO₂ reduction by the world ocean: Experiments with the Hamburg carbon cycle model: *Paleoceanography*, v. 6, no. 4, p. 395-430.
- Helly, J.J., and Levin, L.A., 2004, Global distribution of naturally occurring marine hypoxia on continental margins: *Deep Sea Research Part I: Oceanographic Research Papers*, v. 51, no. 9, p. 1159-1168.
- Hofmann, M., and Schellnhuber, H., 2009, Oceanic acidification affects marine carbon pump and triggers extended marine oxygen holes: *Proceedings of the National Academy of Sciences*, v. 106, no. 9, p. 3017-3022.
- Hönisch, B., and Hemming, N.G., 2005, Surface ocean pH response to variations in pCO₂ through two full glacial cycles: *Earth and Planetary Science Letters*, v. 236, no. 1, p. 305-314.
- Hönisch, B., Hemming, N.G., Archer, D., Siddall, M., and McManus, J.F., 2009, Atmospheric carbon dioxide concentration across the mid-Pleistocene transition: *Science (New York, N.Y.)*, v. 324, no. 5934, p. 1551-1554.
- Hönisch, B., Ridgwell, A., Schmidt, D.N., et al., 2012, The geological record of ocean acidification: *Science (New York, N.Y.)*, v. 335, no. 6072, p. 1058-1063.
- Honjo, S., Connell, J.F., and Sachs, P.L., 1980, Deep-ocean sediment trap; design and function of PARFLUX Mark II: *Deep Sea Research Part A: Oceanographic Research Papers*, v. 27, no. 9, p. 745-753.
- Honjo, S., Dymond, J., Collier, R., and Manganini, S.J., 1995, Export production of particles to the interior of the equatorial Pacific Ocean during the 1992 EqPac

- experiment: Deep Sea Research Part II: Topical Studies in Oceanography, v. 42, no. 2, p. 831-870.
- Houghton, J.T., 2004, Global Warming, Cambridge University Press.
- Howard, M., Winguth, A., Klaas, C., and Maier-Reimer, E., 2006, Sensitivity of ocean carbon tracer distributions to particulate organic flux parameterizations: Global Biogeochemical Cycles, v. 20, no. 3, DOI: 10.1029/2005GB002499.
- IPCC. 2013. The IPCC Fifth Assessment Report (AR5), Climate Change 2013: The Physical Science Basis. Intergovernmental Panel on Climate Change, Geneva, Switzerland.
- IPCC. 1994. The IPCC Second Assessment Report (AR2), Climate Change 1995: The Physical Science Basis. Intergovernmental Panel on Climate Change, Geneva, Switzerland.
- Isozaki, Y., 1997, Permo-Triassic boundary superanoxia and stratified superocean: records from lost deep sea: Science, v. 276, no. 5310, p. 235-238.
- Ito, A., Kok, J.F., Feng, Y., and Penner, J.E., 2012, Does a theoretical estimation of the dust size distribution at emission suggest more bioavailable iron deposition?: Geophysical Research Letters, v. 39, no. 5, DOI: 10.1029/2011GL050455.
- Ittekkot, V., 1993, The abiotically driven biological pump in the ocean and short-term fluctuations in atmospheric CO₂ contents: Global and Planetary Change, v. 8, no. 1, p. 17-25.
- Jickells, T., An, Z., Andersen, K.K., et al., 2005, Global iron connections between desert dust, ocean biogeochemistry, and climate: Science, v. 308, no. 5718, p. 67-71.
- Johnson, K.S., Gordon, R.M., and Coale, K.H., 1997, What controls dissolved iron concentrations in the world ocean?: Marine Chemistry, v. 57, no. 3, p. 137-161.

- Joos, F., Sarmiento, J., and Siegenthaler, U., 1991, Estimates of the effect of Southern Ocean iron fertilization on atmospheric CO₂ concentrations: *Nature*, v. 349, p. 772-775.
- Kamykowski, D., and Zentara, S., 1990, Hypoxia in the world ocean as recorded in the historical data set: *Deep Sea Research Part A. Oceanographic Research Papers*, v. 37, no. 12, p. 1861-1874.
- Karstensen, J., Stramma, L., and Visbeck, M., 2008, Oxygen minimum zones in the eastern tropical Atlantic and Pacific oceans: *Progress in Oceanography*, v. 77, no. 4, p. 331-350.
- Keeling, R.F., Körtzinger, A., and Gruber, N., 2010, Ocean deoxygenation in a warming world: *Annual Review of Marine Science*, v. 2, p. 199-229.
- Kennett, J., and Stott, L., 1991, Abrupt deep-sea warming, palaeoceanographic changes and benthic extinctions at the end: *Nature*, v. 353, p. 19.
- Kidder, D.L., and Worsley, T.R., 2004, Causes and consequences of extreme Permo-Triassic warming to globally equable climate and relation to the Permo-Triassic extinction and recovery: *Palaeogeography, Palaeoclimatology, Palaeoecology*, v. 203, no. 3, p. 207-237.
- Knoll, A.H., Bambach, R., Canfield, D., and Grotzinger, J., 1996, Comparative Earth history and Late Permian mass extinction: *SCIENCE-NEW YORK THEN WASHINGTON-*, p. 452-457.
- Knorr, G., and Lohmann, G., 2007, Rapid transitions in the Atlantic thermohaline circulation triggered by global warming and meltwater during the last deglaciation: *Geochemistry, Geophysics, Geosystems*, v. 8, no. 12, DOI: 10.1029/2007GC001604.

- Knorr, G., and Lohmann, G., 2003, Southern Ocean origin for the resumption of Atlantic thermohaline circulation during deglaciation: *Nature*, v. 424, no. 6948, p. 532-536.
- Kuypers, M.M., Pancost, R.D., and Damsté, J.S.S., 1999, A large and abrupt fall in atmospheric CO₂ concentration during Cretaceous times: *Nature*, v. 399, no. 6734, p. 342-345.
- Lannuzel, D., Schoemann, V., de Jong, J., et al., 2010, Distribution of dissolved iron in Antarctic sea ice: Spatial, seasonal, and inter-annual variability: *Journal of Geophysical Research: Biogeosciences (2005–2012)*, v. 115, no. G3, DOI: 10.1029/2009JG001031.
- Leckie, R.M., Bralower, T.J., and Cashman, R., 2002, Oceanic anoxic events and plankton evolution: Biotic response to tectonic forcing during the mid-Cretaceous: *Paleoceanography*, v. 17, no. 3, p. 13-1-13-29.
- Leckie, R.M., Bralower, T.J., and Cashman, R., 2002, Oceanic anoxic events and plankton evolution: Biotic response to tectonic forcing during the mid-Cretaceous: *Paleoceanography*, v. 17, no. 3, p. 1041.
- Levitus, S., Antonov, J., Baranova, O., et al., 2013, The World Ocean Database: Data Science Journal, v. 12, no. 0, p. WDS229-WDS234.
- Liu, Z., Otto-Bliesner, B., He, F., et al., 2009, Transient simulation of last deglaciation with a new mechanism for Bølling-Allerød warming: *Science*, v. 325, no. 5938, p. 310-314.
- Liu, Z., Pagani, M., Zinniker, D., et al., 2009, Global cooling during the eocene-oligocene climate transition: *Science (New York, N.Y.)*, v. 323, no. 5918, p. 1187-1190.
- Locarmini, R. A., A. V. Mishonov, J. I. Antonov, T. P. Boyer, H. E. Garcia, O. K. Baranova, M. M. Zweng, C. R. Paver, J. R. Reagan, D. R. Johnson, M. Hamilton,

- and D. Seidov, 2013, *World Ocean Atlas 2013, Volume 1: Temperature*. S. Levitus, Ed., A. Mishonov Technical Ed.; NOAA Atlas NESDIS 73, p. 40.
- Locarmini, R.A., Mishonov, A.V., Antonov, J.I., Boyer, T.P., Garcia, H.E., and Levitus, S., 2006, *World Ocean Atlas 2005 Volume 1: Oxygen*: NOAA Atlas NESDIS 61, no. 1.
- Luo, C., Mahowald, N., Bond, T., et al., 2008, Combustion iron distribution and deposition: *Global Biogeochemical Cycles*, v. 22, no. 1, GB1012, DOI: 10.1029/2007GB002964.
- Maher, B., Prospero, J., Mackie, D., Gaiero, D., Hesse, P., and Balkanski, Y., 2010, Global connections between aeolian dust, climate and ocean biogeochemistry at the present day and at the last glacial maximum: *Earth-Science Reviews*, v. 99, no. 1, p. 61-97.
- Mahowald, N.M., Baker, A.R., Bergametti, G., et al., 2005, Atmospheric global dust cycle and iron inputs to the ocean: *Global Biogeochemical Cycles*, v. 19, no. 4, GB4025, DOI: 10.1029/2004GB002402.
- Mahowald, N.M., Engelstaedter, S., Luo, C., et al., 2009, Atmospheric Iron Deposition: Global Distribution, Variability, and Human Perturbations*: *Annual Review of Marine Science*, v. 1, p. 245-278.
- Mahowald, N.M., and Luo, C., 2003, A less dusty future?: *Geophysical Research Letters*, v. 30, no. 17, p. 1903.
- Mahowald, N.M., Muhs, D.R., Levis, S., Rasch, P.J., Yoshioka, M., Zender, C.S., and Luo, C., 2006, Change in atmospheric mineral aerosols in response to climate: Last glacial period, preindustrial, modern, and doubled carbon dioxide climates: *Journal of Geophysical Research*, v. 111, no. D10, p. D10202.

- Mahowald, N., Ballantine, J., Feddema, J., and Ramankutty, N., 2007, Global trends in visibility: Implications for dust sources: *Atmos.Chem.Phys*, v. 7, no. 12, p. 3309-3339.
- Maier-Reimer, E., 1993, Geochemical cycles in an ocean general circulation model. Preindustrial tracer distributions: *Global Biogeochemical Cycles*, v. 7, no. 3, p. 645-677.
- Maier-Reimer, E., and Hasselmann, K., 1987, Transport and storage of CO₂ in the ocean an inorganic ocean-circulation carbon cycle model: *Climate Dynamics*, v. 2, no. 2, p. 63-90.
- Maier-Reimer, E., Mikolajewicz, U., and Hasselmann, K., 1993, Mean circulation of the Hamburg LSG OGCM and its sensitivity to the thermohaline surface forcing: *Journal of Physical Oceanography*, v. 23, no. 4, p. 731-757.
- Maier-Reimer, E., Mikolajewicz, U., and Winguth, A., 1996, Future ocean uptake of CO₂: interaction between ocean circulation and biology: *Climate Dynamics*, v. 12, no. 10, p. 711-722.
- Martin, J.H., 1990, Glacial-interglacial CO₂ change: The iron hypothesis: *Paleoceanography*, v. 5, no. 1, p. 1-13.
- Martin, J.H., and Fitzwater, S., 1988, Iron deficiency limits phytoplankton growth in the north-east Pacific subarctic: *Nature*, v. 331, no. 3414343, p. 947-975.
- Martin, J.H., Knauer, G.A., Karl, D.M., and Broenkow, W.W., 1987, VERTEX: carbon cycling in the northeast Pacific: *Deep Sea Research Part A.Oceanographic Research Papers*, v. 34, no. 2, p. 267-285.
- Martínez-García, A., Rosell-Melé, A., Jaccard, S.L., Geibert, W., Sigman, D.M., and Haug, G.H., 2011, Southern Ocean dust-climate coupling over the past four million years: *Nature*, v. 476, no. 7360, p. 312-315.

- Matear, R., Hirst, A., and McNeil, B., 2000, Changes in dissolved oxygen in the Southern Ocean with climate change: *Geochemistry, Geophysics, Geosystems*, v. 1, no. 11, paper number 200GB000086.
- McConnell, J.R., Aristarain, A.J., Banta, J.R., Edwards, P.R., and Simões, J.C., 2007, 20th-Century doubling in dust archived in an Antarctic Peninsula ice core parallels climate change and desertification in South America: *Proceedings of the National Academy of Sciences*, v. 104, no. 14, p. 5743-5748.
- McInerney, F. A., and Wing, S.L., 2011, The Paleocene-Eocene thermal maximum: a perturbation of carbon cycle, climate, and biosphere with implications for the future: *Annual Review of Earth and Planetary Science*, v. 39, p. 489-516.
- Melzner, F., Thomsen, J., Koeve, W., et al., 2012, Future ocean acidification will be amplified by hypoxia in coastal habitats: *Marine Biology*, p. 1-14.
- Meyer, K.M., Kump, L.R., and Ridgwell, A., 2008, Biogeochemical controls on photic-zone euxinia during the end-Permian mass extinction: *Geology*, v. 35, no. 9, p.747-750.
- Mikolajewicz, U., Gröger, M., Maier-Reimer, E., Schurgers, G., Vizcaino, M., and Winguth, A.M., 2007, Long-term effects of anthropogenic CO₂ emissions simulated with a complex earth system model: *Climate Dynamics*, v. 28, no. 6, p. 599-633.
- Misumi, K., and Yamanaka, Y., 2008, Ocean anoxic events in the mid-Cretaceous simulated by a 3-D biogeochemical general circulation model: *Cretaceous Research*, v. 29, no. 5, p. 893-900.
- Moore, J.K., Lindsay, K., Doney, S.C., Long, M.C., and Misumi, K., 2013, Marine Ecosystem Dynamics and Biogeochemical Cycling in the Community Earth System Model [CESM1 (BGC)]: Comparison of the 1990s with the 2090s under

- the RCP4.5 and RCP8.5 Scenarios.: *Journal of Climate*, v. 26, no. 23, p. 9291-9312.
- Moore, J., and Braucher, O., 2008, Sedimentary and mineral dust sources of dissolved iron to the world ocean: *Biogeosciences*, v. 5, no. 3, p. 631-656.
- Najjar, R.G., Sarmiento, J.L., and Toggweiler, J.R., 1992, Downward transport and fate of organic matter in the ocean: Simulations with a general circulation model. *Global Biogeochemical Cycles*, v. 6, no. 1., p. 45-76.
- Nameroff, T., Calvert, S., and Murray, J., 2004, Glacial-interglacial variability in the eastern tropical North Pacific oxygen minimum zone recorded by redox sensitive trace metals: *Paleoceanography*, v. 19, no. 1, DOI: 10.1029/2003PA000912.
- Neff, J., Ballantyne, A., Farmer, G., et al., 2008, Increasing eolian dust deposition in the western United States linked to human activity: *Nature Geoscience*, v. 1, no. 3, p. 189-195.
- Oschlies, A., Schulz, K.G., Riebesell, U., and Schmittner, A., 2008, Simulated 21st century's increase in oceanic suboxia by CO₂ and enhanced biotic carbon export: *Global Biogeochemical Cycles*, v. 22, no. 4, DOI: 10.1029/2007GB003147.
- Otto-Bliesner, B.L., 2003, The role of mountains, polar ice, and vegetation in determining the tropical climate during the Middle Pennsylvanian: *Climate model simulations: Society for Sedimentary Geology (SEPM)*, ISBN 1-56576-085-9, p. 227-237.
- Paasche, E., 1969, Light-dependent coccolith formation in the two forms of *Coccolithus pelagicus*: *Archiv für Mikrobiologie*, v. 67, no. 2, p. 199-208.
- Palastanga, V., Slomp, C., and Heinze, C., 2013, Glacial-interglacial variability in ocean oxygen and phosphorus in a global biogeochemical model: *Biogeosciences*, v. 10, p. 945-958.

- Palastanga, V., Slomp, C., and Heinze, C., 2011, Long-term controls on ocean phosphorus and oxygen in a global biogeochemical model: *Global Biogeochemical Cycles*, v. 25, no. 3, GB 3024, DOI: 10.1029/2010GB003827.
- Pälike, H., Lyle, M.W., Nishi, H., et al., 2012, A Cenozoic record of the equatorial Pacific carbonate compensation depth: *Nature*, v. 488, no. 7413, p. 609-614.
- Panchuk, K., Ridgwell, A., and Kump, L., 2008, Sedimentary response to Paleocene-Eocene Thermal Maximum carbon release: A model-data comparison: *Geology*, v. 36, no. 4, p. 315-318.
- Parekh, P., Follows, M.J., and Boyle, E.A., 2005, Decoupling of iron and phosphate in the global ocean: *Global Biogeochemical Cycles*, v. 19, no. 2, DOI: 10.1029/2004GB002280.
- Paulmier, A., Ruiz-Pino, D., and Garçon, V., 2011, CO₂ maximum in the oxygen minimum zone (OMZ): *Biogeosciences*, v. 8, no. 2, p. 239-252.
- Payne, J.L., Lehrmann, D.J., Wei, J., Orchard, M.J., Schrag, D.P., and Knoll, A.H., 2004, Large perturbations of the carbon cycle during recovery from the end-permian extinction: *Science (New York, N.Y.)*, v. 305, no. 5683, p. 506-509.
- Pelejero, C., Calvo, E., and Hoegh-Guldberg, O., 2010, Paleo-perspectives on ocean acidification: *Trends in Ecology & Evolution*, v. 25, no. 6, p. 332-344.
- Plattner, G., Joos, F., Stocker, T., and Marchal, O., 2001, Feedback mechanisms and sensitivities of ocean carbon uptake under global warming: *Tellus B*, v. 53, no. 5, p. 564-592.
- LaQuéré, C.L., Andres, R.J., Boden, T., et al., 2013, The global carbon budget 1959–2011: *Earth System Science Data*, v. 5, no. 1, p. 165-185.
- Rabouille, C., Gaillard, J., Relexans, J., Treguer, P., and Vincendeau, M., 1998, Recycling of organic matter in Antarctic sediments: A transect through the polar

- front in the Southern Ocean (Indian sector): *Limnology and Oceanography*, v. 43, no. 3, p. 420-432.
- Redfield, A.C., 1934, On the proportions of organic derivatives in sea water and their relation to the composition of plankton: University Press of Liverpool, p. 176-192.
- Richards, F.A., Cline, J.D., Broenkow, W.W., and Atkinson, L.P., 1965, Some consequences of the decomposition of organic matter in Lake Nitinat, an anoxic fjord: *Limnology and Oceanography*, p. 185-201.
- Riebesell, U., Zondervan, I., Rost, B., and Zeebe, R., 2001, Effects of increasing atmospheric CO₂ on phytoplankton communities and the biological carbon pump: *Global Change Newsletter*, v. 47, p. 12-15.
- Ruddiman, W.F., 2001, *Earth's Climate: past and future*, Macmillan.
- Sabine, C.L., Feely, R.A., Gruber, N., et al., 2004, The oceanic sink for anthropogenic CO₂: *Science*, v. 305, no. 5682, p. 367-371.
- Sarmiento, J.L., Hughes, T.M., Stouffer, R.J., and Manabe, S., 1998, Simulated response of the ocean carbon cycle to anthropogenic climate warming: *Nature*, v. 393, no. 6682, p. 245-249.
- Sarmiento, J.L., and Orr, J.C., 1991, Three-dimensional simulations of the impact of Southern Ocean nutrient depletion on atmospheric CO₂ and ocean chemistry: *Limnol.Oceanogr*, v. 36, no. 8, p. 1928-1950.
- Sarmiento, J.L., and Gruber, N., 2006, *Ocean biogeochemical dynamics*, Princeton University Press Princeton 1015.
- Schmittner, A., Oschlies, A., Matthews, H.D., and Galbraith, E.D., 2008, Future changes in climate, ocean circulation, ecosystems, and biogeochemical cycling simulated for a business-as-usual CO₂ emission scenario until year 4000 AD: *Global Biogeochemical Cycles*, v. 22, no. 1, p. GB1013.

- Sedwick, P.N., and DiTullio, G.R., 1997, Regulation of algal blooms in Antarctic shelf waters by the release of iron from melting sea ice: *Geophysical Research Letters*, v. 24, no. 20, p. 2515-2518.
- Seibel, B.A., and Childress J.J., 2013, The real limits to marine life: a further critique of the Respiration Index: *Biogeosciences*, v.10, no, 5, p. 2815-2819.
- Seiter, K., Hensen, C., Schröter, J., and Zabel, M., 2004, Organic carbon content in surface sediments—defining regional provinces: *Deep Sea Research Part I: Oceanographic Research Papers*, v. 51, no. 12, p. 2001-2026.
- Seki, O., Foster, G.L., Schmidt, D.N., Mackensen, A., Kawamura, K., and Pancost, R.D., 2010, Alkenone and boron-based Pliocene p CO₂ records: *Earth and Planetary Science Letters*, v. 292, no. 1, p. 201-211.
- Shaffer, G., 1996, Biogeochemical cycling in the global ocean 2. New production, Redfield ratios, and remineralization in the organic pump: *Journal of geophysical research*, v. 101, no. C2, p. 3723-3745.
- Shaffer, G., Olsen, S.M., and Pedersen, J.O.P., 2009, Long-term ocean oxygen depletion in response to carbon dioxide emissions from fossil fuels: *Nature Geoscience*, v. 2, no. 2, p. 105-109.
- Sikes, C.S., and Wilbur, K.M., 1980, Calcification by Coccolithophorids: Effects of pH and Sr1: *Journal of Phycology*, v. 16, no. 3, p. 433-436.
- Slomp, C.P., Epping, E.H., Helder, W., and Van Raaphorst, W., 1996, A key role for iron-bound phosphorus in authigenic apatite formation in North Atlantic continental platform sediments: *Journal of Marine Research*, v. 54, no. 6, p. 1179-1205.
- Slomp, C.P., Thomson, J., and de Lange, G.J., 2004, Controls on phosphorus regeneration and burial during formation of eastern Mediterranean sapropels: *Marine Geology*, v. 203, no. 1, p. 141-159.

- Slomp, C.P., Thomson, J., and de Lange, G.J., 2002, Enhanced regeneration of phosphorus during formation of the most recent eastern Mediterranean sapropel (S1): *Geochimica et Cosmochimica Acta*, v. 66, no. 7, p. 1171-1184.
- Sluijs, A., Brinkhuis, H., Schouten, S., et al., 2007, Environmental precursors to rapid light carbon injection at the Palaeocene/Eocene boundary: *Nature*, v. 450, no. 7173, p. 1218-1221.
- Spero, H.J., Bijma, J., Lea, D.W., and Bemis, B.E., 1997, Effect of seawater carbonate concentration on foraminiferal carbon and oxygen isotopes: *Nature*, v. 390, no. 6659, p. 497-500.
- Stocker, T.F., and Schmittner, A., 1997, Influence of CO₂ emission rates on the stability of the thermohaline circulation: *Nature*, v. 388, no. 6645, p. 862-865.
- Storey, M., Duncan, R.A., and Swisher, C.C., 2007, Paleocene-Eocene thermal maximum and the opening of the northeast Atlantic: *Science*, v. 316, no. 5824, p. 587-589.
- Stouffer, R., Yin, J., Gregory, J., et al., 2006, Investigating the causes of the response of the thermohaline circulation to past and future climate changes: *Journal of Climate*, v. 19, no. 8, p. 1365-1387.
- Stramma, L., Oschlies, A., and Schmidtko, S., 2012, Anticorrelated observed and modeled trends in dissolved oceanic oxygen over the last 50 years: *Biogeosciences Discussions*, v. 9, no. 4, p. 4595-4626.
- Stramma, L., Johnson, G.C., Sprintall, J., and Mohrholz, V., 2008, Expanding oxygen-minimum zones in the tropical oceans: *Science*, v. 320, no. 5876, p. 655-658.
- Stramma, L., Visbeck, M., Brandt, P., Tanhua, T., and Wallace, D., 2009, Deoxygenation in the oxygen minimum zone of the eastern tropical North Atlantic: *Geophysical Research Letters*, v. 36, no. 20, p. L20607.

- Sun, Y., Joachimski, M.M., Wignall, P.B., et al., 2012, Lethally hot temperatures during the Early Triassic greenhouse: *Science* (New York, N.Y.), v. 338, no. 6105, p. 366-370.
- Svensen, H., Planke, S., Møllegaard, A., Jamveit, B., Myklebust, R., Eidem, T.R., and Rey, S.S., 2004, Release of methane from a volcanic basin as a mechanism for initial Eocene global warming: *Nature*, v. 429, no. 6991, p. 542-545.
- Takahashi, M., and Parsons, T.R., 1973, *Biological oceanographic processes*, Pergamon press.
- Takahashi, M., Hama, T., Matsunaga, K., and Handa, N., 1995, Photosynthetic organic carbon production and respiratory organic carbon consumption in the trophogenic layer of Lake Biwa: *Journal of Plankton Research*, v. 17, no. 5, p. 1017-1025.
- Tegen, I., Werner, M., Harrison, S.P., and Kohfeld, K.E., 2004, Relative importance of climate and land use in determining present and future global soil dust emission: *Geophysical Research Letters*, v. 31, no. 5, DOI: 10.1029/2003GL019216.
- Thomas, E., 2006, An ocean view of the early Cenozoic Greenhouse World: *Oceanography*, v. 19, no. 4, p. 94-103.
- Thomas, E., and Shackleton, N.J., 1996, The Paleocene-Eocene benthic foraminiferal extinction and stable isotope anomalies: *Geological Society, London, Special Publications*, v. 101, no. 1, p. 401-441.
- Thunell, R., Qingmin, M., Calvert, S., and Pedersen, T., 1992, Glacial-Holocene Biogenic Sedimentation Patterns in the South China Sea: Productivity Variations and Surface Water pCO₂: *Paleoceanography*, v. 7, no. 2, p. 143-162.

- Van Cappellen, P., and Ingall, E.D., 1996, Redox stabilization of the atmosphere and oceans by phosphorus-limited marine productivity: *Science*, v. 271, no. 5248, p. 493-496.
- Van Cappellen, P., and Ingall, E.D., 1994, Benthic phosphorus regeneration, net primary production, and ocean anoxia: A model of the coupled marine biogeochemical cycles of carbon and phosphorus: *Paleoceanography*, v. 9, no. 5, p. 677-692.
- Volk, T., and Hoffert, M.I., 1985, Ocean carbon pumps: Analysis of relative strengths and efficiencies in ocean-driven atmospheric CO₂ changes: *The Carbon Cycle and Atmospheric CO₂: Natural Variations Archean to Present*, p.99-110.
- Walling, D., and Fang, D., 2003, Recent trends in the suspended sediment loads of the world's rivers: *Global and Planetary Change*, v. 39, no. 1, p. 111-126.
- Weaver, A.J., Saenko, O.A., Clark, P.U., and Mitrovica, J.X., 2003, Meltwater pulse 1A from Antarctica as a trigger of the Bølling-Allerød warm interval: *Science*, v. 299, no. 5613, p. 1709-1713.
- Weiss, R., 1970, The solubility of nitrogen, oxygen and argon in water and seawater, *in* *Deep Sea Research and Oceanographic Abstracts*, Elsevier, p. 721-735.
- Weissert, H., 1981, The Environment of Deposition of Black Shales in the Early Cretaceous an Ongoing Controversy: *The Society of Economic Paleontologist and Mineralogist (SEPM)*, SEPM Special Publication, no. 32, p. 547-560.
- Whitney, F.A., Freeland, H.J., and Robert, M., 2007, Persistently declining oxygen levels in the interior waters of the eastern subarctic Pacific: *Progress in Oceanography*, v. 75, no. 2, p. 179-199.
- Wignall, P., and Hallam, A., 1993, Griesbachian (Earliest Triassic) palaeoenvironmental changes in the Salt Range, Pakistan and southeast China and their bearing on

- the Permo-Triassic mass extinction: *Palaeogeography, Palaeoclimatology, Palaeoecology*, v. 102, no. 3, p. 215-237.
- Winguth, A., Mikolajewicz, U., Gröger, M., Maier-Reimer, E., Schurgers, G., and Vizcaíno, M., 2005, Centennial scale interactions between the carbon cycle and anthropogenic climate change using a dynamic Earth system model: *Geophysical Research Letters*, v. 32, no. 23, DOI: 10.1029/2005GL023681.
- Winguth, A., Archer, D., Duplessy, J., Maier-Reimer, E., and Mikolajewicz, U., 1999, Sensitivity of paleonutrient tracer distributions and deep-sea circulation to glacial boundary conditions: *Paleoceanography*, v. 14, no. 3, p. 304-323.
- Winguth, C., and Winguth, A., 2012, Simulating Permian-Triassic oceanic anoxia distribution: Implications for species extinction and recovery: *Geology*, v. 40, no. 2, p.127-130.
- Wolff, E.W., Fischer, H., Fundel, F., et al., 2006, Southern Ocean sea-ice extent, productivity and iron flux over the past eight glacial cycles: *Nature*, v. 440, no. 7083, p. 491-496.
- Woodward, S., Roberts, D., and Betts, R., 2005, A simulation of the effect of climate change-induced desertification on mineral dust aerosol: *Geophysical Research Letters*, v. 32, no. 18, DOI: 10.1029/2005GL023482.
- Wyrтки, K., 1987, Indonesian through flow and the associated pressure gradient: *Journal of Geophysical Research: Oceans (1978-2012)*, v. 92, c.12, p.12941-12946.
- Yates, K.K., Dufore, C., Smiley, N., Jackson, C., and Halley, R.B., 2007, Diurnal variation of oxygen and carbonate system parameters in Tampa Bay and Florida Bay: *Marine Chemistry*, v. 104, no. 1, p. 110-124.

- Yu, J., and Elderfield, H., 2007, Benthic foraminiferal B/Ca ratios reflect deep water carbonate saturation state: *Earth and Planetary Science Letters*, v. 258, no. 1, p. 73-86.
- Yu, J., Elderfield, H., and Hönisch, B., 2007, B/Ca in planktonic foraminifera as a proxy for surface seawater pH: *Paleoceanography*, v. 22, no. 2, DOI: 10.1029/2006PA001347.
- Zachos, J.C., Dickens, G.R., and Zeebe, R.E., 2008, An early Cenozoic perspective on greenhouse warming and carbon-cycle dynamics: *Nature*, v. 451, no. 7176, p. 279-283.
- Zachos, J.C. and Kump, L.R., 2005, Carbon cycle feedbacks and the initiation of Antarctic glaciations in the earliest Oligocene: *Global and Planetary Change*, v. 47, p. 51-66.
- Zachos, J.C., Opdyke, B.N., Quinn, T.M., Jones, C.E., and Halliday, A.N., 1999, Early Cenozoic glaciation, Antarctic weathering, and seawater $^{87}\text{Sr}/^{86}\text{Sr}$: Is there a link?: *Chemical Geology*, v. 161, p. 165-180.
- Zachos, J.C., Röhl, U., Schellenberg, S.A., et al., 2005, Rapid acidification of the ocean during the Paleocene-Eocene thermal maximum: *Science*, v. 308, no. 5728, p. 1611-1615.
- Zeebe, R.E., Zachos, J.C., Caldeira, K., and Tyrrell, T., 2008, Carbon emissions and acidification: *Science*, v. 321, no. 5885, p. 51.
- Zender, C.S., Miller, R., and Tegen, I., 2004, Quantifying mineral dust mass budgets: Terminology, constraints, and current estimates: *EOS, Transactions American Geophysical Union*, v. 85, no. 48, p. 509-512.

- Zickfeld, K., Eby, M., and Weaver, A.J., 2008, Carbon-cycle feedbacks of changes in the Atlantic meridional overturning circulation under future atmospheric CO₂: *Global Biogeochemical Cycles*, v. 22, no. 3, DOI: 10.1029/2007GB003118.
- Zondervan, I., Zeebe, R.E., Rost, B., and Riebesell, U., 2001, Decreasing marine biogenic calcification: A negative feedback on rising atmospheric pCO₂: *Global Biogeochemical Cycles*, v. 15, no. 2, p. 507-516.
- Zweng, M.M., J.R. Reagan, J.I. Antonov, R.A. Locarnini, A.V. Mishonov, T.P. Boyer, H.E. Garcia, O.K. Baranova, D.R. Johnson, D. Seidov, M.M. Biddle, 2013, *World Ocean Atlas 2013, Volume 2: Salinity*. S. Levitus, Ed., A. Mishonov Technical Ed.; NOAA Atlas NESDIS 74, p. 39.

Biographical Information

Teresa Sykes graduated from the University of Mary Hardin-Baylor with a Bachelor degree in Biology in May of 1992. She began work as a Medical Technologist after graduation but decided to leave the medical field as pursue a Master of Science in Environmental Science from Tarleton State University which was granted in May of 2008. In the fall of 2008 she began the Ph.D. program in Earth and Environmental Science at the University of Texas at Arlington and completed the program in Dec 2014. Teresa Sykes was also an active member of the United States Air Force Reserve and deployed many times during her MS and Ph.D research. Dr. Sykes would like to continue her research in biogeochemical cycles and climate change as well as teach and lead students in research.